Chem Soc Rev

ROYAL SOCIETY OF CHEMISTRY

REVIEW ARTICLE

View Article Online
View Journal | View Issue

Cite this: *Chem. Soc. Rev.*, 2024, **53**, 9378

Metal–organic frameworks for organic transformations by photocatalysis and photothermal catalysis

Hong-Guang Jin, *[a] Peng-Cheng Zhao,[a] Yunyang Qian,[c] Juan-Ding Xiao,*[b] Zi-Sheng Chao[a] and Hai-Long Jiang *[c]

Organic transformation by light-driven catalysis, especially, photocatalysis and photothermal catalysis, denoted as photo(thermal) catalysis, is an efficient, green, and economical route to produce value-added compounds. In recent years, owing to their diverse structure types, tunable pore sizes, and abundant active sites, metal–organic framework (MOF)-based photo(thermal) catalysis has attracted broad interest in organic transformations. In this review, we provide a comprehensive and systematic overview of MOF-based photo(thermal) catalysis for organic transformations. First, the general mechanisms, unique advantages, and strategies to improve the performance of MOFs in photo(thermal) catalysis are discussed. Then, outstanding examples of organic transformations over MOF-based photo(thermal) catalysis are introduced according to the reaction type. In addition, several representative advanced characterization techniques used for revealing the charge reaction kinetics and reaction intermediates of MOF-based organic transformations by photo(thermal) catalysis are presented. Finally, the prospects and challenges in this field are proposed. This review aims to inspire the rational design and development of MOF-based materials with improved performance in organic transformations by photocatalysis and photothermal catalysis.

Received 7th July 2024

DOI: 10.1039/d4cs00095a

rsc.li/chem-soc-rev

1. Introduction

As one of the most crucial disciplines in the field of chemistry, organic synthetic chemistry, which can create a rich variety of functional molecules, plays a crucial role in improving human life and social civilization.[1] Conventional organic synthesis often involves complicated reaction steps with harsh reaction conditions, resulting in high energy consumption and aggravated

[a] *School of Materials Science and Engineering, Changsha University of Science & Technology, Changsha, 410114, China. E-mail: jesonjin08@csust.edu.cn*
[b] *Institutes of Physical Science and Information Technology, Anhui University, Hefei, Anhui, 230601, P. R. China. E-mail: jdxiao@ahu.edu.cn*
[c] *Hefei National Research Center for Physical Sciences at the Microscale, Department of Chemistry, University of Science and Technology of China, Hefei, Anhui, 230026, China. E-mail: jianglab@ustc.edu.cn*

Hong-Guang Jin

Hong-Guang Jin received his PhD (2016) from Aix-Marseille Université. He subsequently worked at Hunan University as a postdoc fellow (2017–2019). He is currently working at Changsha University of Science and Technology (CSUST). His research focuses on the synthesis and photocatalytic application of MOF-based materials.

Juan-Ding Xiao

Juan-Ding Xiao received her PhD (2017) from the University of Science and Technology of China (USTC), supervised by Prof. Hai-Long Jiang. She subsequently worked at Chinese Academy of Sciences (CAS) as an assistant researcher and postdoc fellow in 2017–2021. She is currently an associate professor in Anhui University. Her research interest is the synthesis and photocatalysis of MOF-based materials.

environmental problems.[2] Solar energy is becoming one of the most appealing and achievable energy sources due to its magnitude, wide availability, versatility, and clean nature. Commonly, solar energy conversion can be achieved by converting photons into electricity, fuel and heat.[3] Amongst, photo-assisted catalysis, which mainly includes two directly relevant applications involving the use of electrons and heat, photocatalysis and photothermal catalysis, is attractive for organic transformations.[4–8] Nevertheless, it is still challenging to develop a cheap and stable photocatalytic system with high organic transformation efficiency. Several strategies have been adopted to meet this challenge, focusing on the intrinsic structural optimization of photocatalysts to improve the key processes in solar energy utilization: (1) solar light absorption, (2) charge separation and transfer, (3) surface redox reactions, and (4) photothermal effect.

As for organic transformation by photocatalysis, the conversion efficiency depends mainly on light harvesting, charge separation, and redox reactions. While for organic transformation by photothermal catalysis, the conversion efficiency is highly dependent on the resulting photothermal effect. Photocatalytic organic transformation was first demonstrated in homogeneous systems by using transition metal complexes, precious metal complexes, and organic dyes as photosensitizers and/or photoactive sites.[9–13] These homogeneous photocatalysts exhibit excellent catalytic performance in various chemical reactions but suffer from drawbacks in terms of high cost and low recyclability for separation from reaction mixtures. In this case, heterogeneous photocatalysts, mainly including semiconductors (*e.g.*, oxides, sulfides, and nitrides) and conjugated organic polymers,[14–18] can be alternatives due to their long lifetime and reusability. Although optimizing the band structures of semiconductors or synthesizing composites (commonly to construct heterojunctions) can ensure the activity and selectivity in photocatalytic organic transformations, the development of photocatalysts with well-defined structures is still particularly desirable because this route can provide in-depth studies on structure–activity relationships and guide the further design of photocatalysts with improved performance.

Hai-Long Jiang

*Hai-Long Jiang earned his PhD (2008) from Fujian Institute of Research on the Structure of Matter, CAS. He subsequently worked at the National Institute of Advanced Industrial Science and Technology (AIST, Japan), first as an AIST Fellow and later as a JSPS Fellow during 2008-2011. After a postdoctoral stint at Texas A&M University (USA), he joined USTC as a full professor in 2013, and was appointed as a chair professor in 2022. He is a Fellow of both the Chinese Chemical Society (FCCS) and Royal Society of Chemistry (FRSC) and has been annually named as a highly cited researcher by Clarivate Analytics since 2017. His research group (**http://mof.ustc.edu.cn**) engages in microenvironment modulation (MEM) of catalytic centers based on reticular materials.*

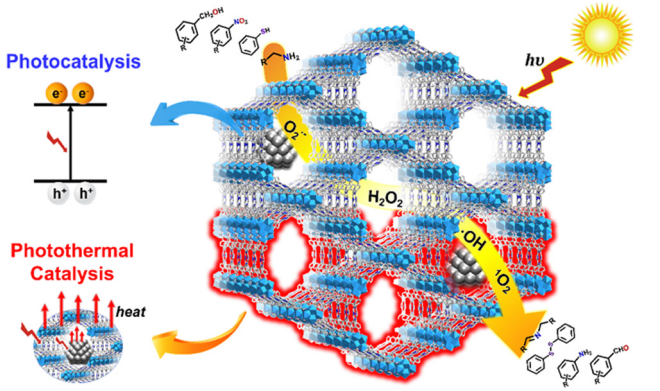

Scheme 1 Schematic illustration showing the organic transformations by MOF-based photocatalysts and photothermal catalysts.

Metal–organic frameworks (MOFs) assembled from metal ions/clusters with organic linkers have received growing attention in the field of photo(thermal) catalysis.[19–23] MOFs feature defined crystalline structures, intrinsically high porosity, tunable chemical compositions, and abundant active sites, making them ideal platforms for studying key photocatalytic processes and structure–activity relationships in organic transformations. The structures of MOFs can be simply designed to enhance their catalytic properties and deepen the understanding of catalytic mechanisms. The main strategies for structural designation include: (1) modifying the organic ligands and/or metal nodes to optimize light absorption, (2) regulating the crystal surface and constructing heterojunctions to promote the migration and separation of photogenerated electron–hole (e^-–h^+) pairs, (3) increasing the number of active sites or creating defect sites to promote surface reactions, and (4) integrating plasmonic units to enhance catalysis *via* photothermal effects.

To date, several reviews have focused on organic transformations using MOF-based heterogeneous catalysts by photocatalysis or photothermal catalysis,[24–30] however, an overview of MOFs for organic transformations by photo(thermal) catalysis is still lacking. Herein, we summarize recent progress in organic transformations by photo(thermal) catalysis over MOF-based catalysts and pay special attention to the general mechanisms and unique advantages of MOF-based photocatalysts (Scheme 1). Given that photo(thermal) catalysis involves several key processes, namely, light absorption, e^-–h^+ separation, surface redox reactions, and photothermal effects, strategies for optimizing these processes and promoting the performance of MOF-based photocatalysts are presented. Subsequently, various organic transformations, including oxidation, reduction, coupling, tandem, synergistic redox, and CO_2 addition reactions over MOF-based photo(thermal) catalysts are introduced. It should be noted that, as a sort of oxidation reactions, the organic dyes photodegradation will not be discussed here due to its nature of mineralized reactions. Furthermore, representative advanced characterization techniques that

can reveal the charge reaction kinetics and reaction intermediates during these organic transformation processes are described. Eventually, current challenges and perspectives in this area are briefly discussed.

2. General mechanism

2.1. Key processes in photocatalysis

A thorough understanding of the photocatalytic mechanism in MOF-based photocatalytic systems will contribute to the development of efficient photocatalysts. Typically, there are three key photophysical/photochemical processes involved in a photocatalysis reaction:[31–33] (i) light absorption by the light-harvesting antenna in MOFs to generate e^- at the lowest unoccupied molecular orbital (LUMO) and h^+ at the highest occupied molecular orbital (HOMO), (ii) separation of e^- and h^+ and migration to the catalyst surface, and (iii) e^- and h^+-engaged surface redox reactions.

Optimization of the photocatalytic performance can be started from the perspective of promoting the above three key processes. For instance, to promote the efficiency of process (i), various methodologies have been adopted to expand the light harvesting of a photocatalytic system toward the visible region, such as the introduction of organic chromophores with large π-conjugated systems or the combination of two or more photocatalysts with different light responsive ranges.[34] Strategies including postmodification and construction of heterojunctions have been commonly utilized to create new electron transport channels that facilitate the process (ii) for efficient charge separation.[35] Surface reactions in process (iii) mainly consist of electron-engaged reduction reactions and hole-engaged oxidation reactions; the former are represented by photocatalytic hydrogen (H_2) production,[36] carbon dioxide (CO_2) reduction,[37] and nitrogen (N_2) fixation,[38] while the latter are known to involve photocatalytic water oxidation,[39] pollution degradation,[40] and organic oxidation reactions.[41] All of these reactions can be promoted by introducing more active sites within a photocatalytic system.

Kinetics and thermodynamic equilibrium of these three distinct processes determine the eventual performance of the photocatalysts. Therefore, it is of paramount importance to characterize and understand these processes objectively and theoretically. If the maximum capacity of one individual stage of these processes can be determined and utilized as a reference to identify the limiting step, the photocatalytic system can be optimized to boost the performance. Considering that the photocatalytic process is essentially an electron transfer process, the characterization of electron transfer involved in process (ii) is the most direct approach to understanding photocatalytic systems. Conventional techniques, mainly including electrochemical impedance spectroscopy, photocurrent and photovoltage spectroscopy, and open-circuit voltage decay techniques, have difficulty in quantitatively characterizing the electron transfer process inside photocatalysts.[42,43] Nevertheless, there are emerged time- and space-resolved advanced techniques, such as transient absorption (TA) spectroscopy,[44] time-resolved photoluminescence (TRPL) spectroscopy,[45] X-ray absorption spectroscopy (XAS),[46] and electron paramagnetic resonance (EPR) spectroscopy,[47] have been adopted to determine the electron transfer kinetics in photocatalysis, contributing to the further design and advancement of high-efficiency photocatalysts in the future.

2.2. Charge/energy transfer mechanism

MOF-based photocatalyst-driven organic transformations follow either charge transfer (CT, direct pathway) or energy transfer (EnT, mediated pathway) mechanism (Fig. 1), commonly assisted by generated reactive species, such as e^-, h^+, superoxide radical anion ($O_2^{\bullet-}$), singlet oxygen ($^1O_2$), hydrogen peroxide (H_2O_2), and hydroxyl radical ($^\bullet OH$).[24–28,48,49] In photocatalytic organic transformations mediated by the CT mechanism, MOF-based photocatalysts are first light-excited to produce e^-–h^+ pairs (excitons or carriers). After efficient separation, the h^+ at HOMO and the e^- at LUMO can interact with the organic substrates and/or sacrificial agents to initiate redox reactions. While in photocatalytic organic transformations driven by the EnT mechanism, the excited states of MOFs are first generated through the absorption of photons with sufficient energy. Then, an EnT process occurs from the excited-state MOF to a substrate molecule, resulting in the formation of more reactive species, which can react with a second substrate to form the final product.

Charge and energy transfer processes have their own advantages in photocatalysis.[50,51] The CT route can realize various advanced oxidation processes through the generation of reactive oxygen species (ROS) over the photocatalytic process, such as $O_2^{\bullet-}$, $^\bullet OH$, and H_2O_2.[52,53] In contrast, the EnT route can allow oxidation reactions to occur *via* the generation of ROS $^1O_2$.[54–56] There is one obvious advantage for the EnT route: it allows some reactions with high potentials, which are almost impossible to achieve *via* the CT route. For instance, the sensitization of conjugated olefins into their excited sates, which is very challenging in the CT route, can be carried out effectively following the EnT route.[57]

The MOF-based photocatalytic organic transformations can be mediated by either CT or EnT alone or by the combination of these two pathways. For example, very recently, Zhang *et al.*

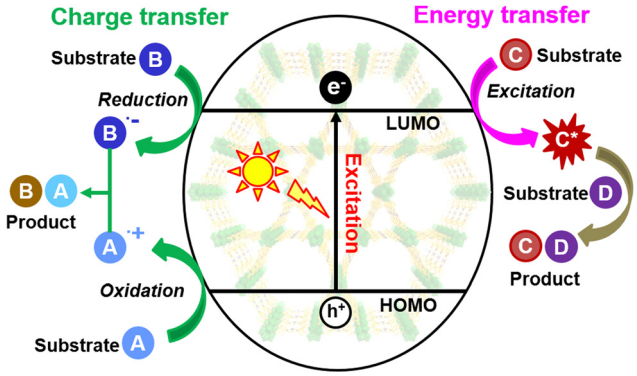

Fig. 1 General photocatalytic mechanism including charge transfer and energy transfer in MOF-based photocatalysts for organic transformations.

synthesized a phosphonate-based Fe-MOF *via* an amorphization strategy, resulting in excellent photocatalytic activity for the selective oxidation of toluene. A mechanistic study revealed that the effective CT facilitated by the distortion of Fe-oxo clusters in the framework can support the abundant generation of $O_2^{\bullet-}$, which is a crucial factor for the efficient oxidation reaction (Fig. 2a).[58] By using the representative pyrene-based MOF NU-1000 as the photocatalyst, Zhang *et al.* realized iodoperfluoroalkylation of olefins *via* the EnT-mediated atom-transfer radical addition (ATRA) route (Fig. 2b).[59] Taking $C_nF_{2n+1}I$ as an example, the homolytic cleavage of the carbon–iodine bond triggered by EnT from photoexcited NU-1000 to $C_nF_{2n+1}I$ can produce perfluoroalkyl and iodine radicals, resulting in the addition of the α- and β-positions of olefin, respectively, to complete the ATRA reaction (Pathway A). When the substrate is an aromatic alkene, the ATRA product undergoes base-assisted elimination of HI to form (*E*)/(*Z*)-isomeric mixtures, which are then enriched to the (*Z*)-isomer by imposing another EnT from the triplet excited state of NU-1000 (Pathway B). Additionally, Wang *et al.* demonstrated that a novel Zn-MOF based on porphyrin- and carbazole-based organic ligands was a remarkable photocatalyst for the oxidation of amines.[60] The synergistic CT and EnT processes upon light irradiation, accounting for the generation of $O_2^{\bullet-}$ and $^1O_2$, respectively, contributed to the high photocatalytic activity (Fig. 2c).

2.3. Photothermal effect

The photothermal effect refers to the property of a material that converts absorbed light to heat. The materials with photothermal effects that have been reported to date can be commonly divided into four categories, namely, precious metal nanoparticles (NPs),[61] inorganic semiconductors,[62] carbon-based materials,[63] and polymers.[64] A systematic elaboration of the photothermal effect from the perspective of the physiochemical mechanism is necessary for the further development of novel excellent photothermal materials and to apply in diverse fields, including photothermal catalysis.[65] The mechanism for light-to-heat conversion is dependent on the nature of the catalysts and generally involves the following three mechanisms (Fig. 3): (i) the light-induced localized surface plasmon resonance (LSPR) can convert light energy into the kinetic energies of electrons and holes, which dissipate nonradiatively to cause a temperature increase in the surrounding medium; (ii) the transition of electrons by photoexcitation can release heat in the nonradiative relaxation process to return to the ground state; and (iii) the molecular vibrations initiated by the light absorption can generate heat to increase the temperature.

Organic transformations over MOF-based photocatalysts by photothermal catalysis can utilize the individual photothermal effect of MOF itself, the incorporated plasmonic NPs supported by MOFs, or the combined photothermal effects of MOFs and NPs.[29,30,66,67] Taking the photothermal effect of MOFs without integrated plasmonic NPs as an example, Zhang *et al.* prepared FeTPyP with a two-dimensional (2D) layered structure, which exhibited excellent photothermal catalytic activity for the synthesis of styrene carbonate *via* the CO_2 cycloaddition reaction.[68] The results show that the crucial ring opening process can be accelerated by the holes generated from the photoexcited FeTPyP, and the promoted charge transfer and separation benefit from the increased temperature of the catalytic system owing to the photothermal effect of 5,10,15,20-tetra(4-pyridyl)porphyrin (H_2TPyP) at the FeTPyP framework (Fig. 4).

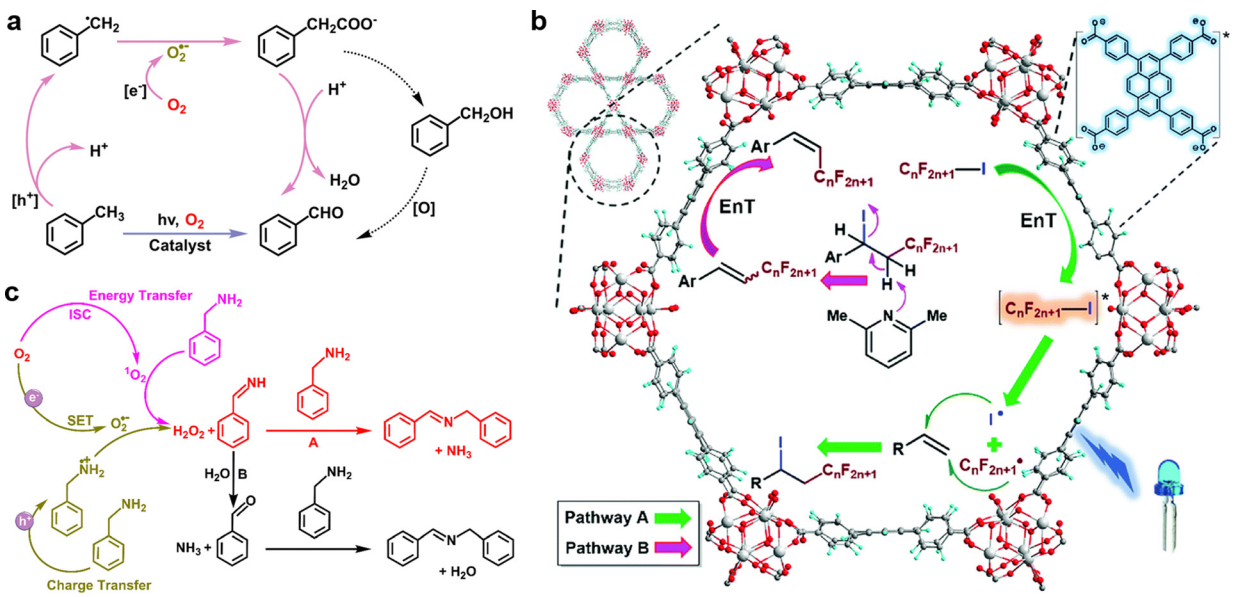

Fig. 2 (a) Charge transfer-mediated photocatalytic selective oxidation of toluene to benzaldehyde over an amorphous Fe-MOF. Adapted with permission from ref. 58. Copyright 2024 Wiley. (b) Energy transfer-mediated photocatalytic ATRA reaction of perfluoroalkyl iodides to olefins (Pathway A) and the generation of (*Z*)-enriched perfluoroalkyl alkenes (Pathway B) over NU-1000. Adapted with permission from ref. 59. Copyright 2018 RSC. (c) Charge transfer and energy transfer-mediated photocatalytic oxidation of amines over a Zn-MOF. Adapted with permission from ref. 60. Copyright 2022 RSC.

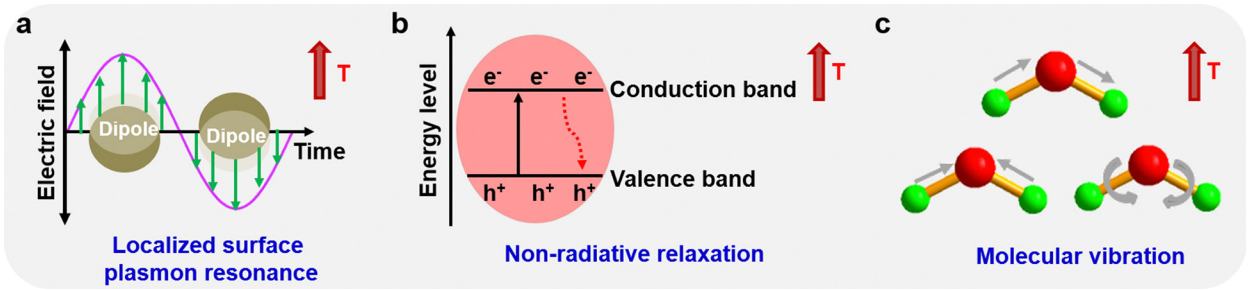

Fig. 3 Schematic illustration of photothermal mechanisms in materials of (a) plasmonic structures, (b) semiconductors, and (c) molecules.

The photothermal effect of MOFs can also contribute to organic transformations by activating the catalytic centers, as shown by Sharma and coworkers.[69] In their work, a novel Mn(II)-porphyrin MOF was successfully prepared, wherein the porphyrin ligands can absorb and convert light into heat to remove the coordinated water molecules around the Mn nodes. The catalytic Mn centers with Lewis acidity were thus activated, which improved their adsorption to the substrates and accelerated the synthesis of cyclic carbonates.

3. Unique advantages of MOFs in photo(thermal) catalysis

3.1. Modulated microenvironment

A microenvironment with unique structural and electronic characteristics around catalytic sites has an important effect on the catalytic behaviors of enzymes and homogeneous catalysis.[70] However, it remains a major challenge to discover the microenvironment modulation of active sites in heterogeneous catalysis because of their vague structure and/or low modifiability.[71] As a class of emerging porous crystalline materials, MOFs with atomically precise and highly tunable structures are ideal candidates as heterogeneous catalysts for regulating the surrounding microenvironment to affect the catalytic performance.[30,72–77] There are many strategies, such as grafting extrinsic organic/inorganic units onto unsaturated metal nodes, functionalization of organic ligands, encapsulation of guests, control of pore/channel size and shape, and alteration of the spatial location of the catalytic sites, to modulate the microenvironment in MOFs to understand the intrinsic structure–activity relationship and further optimize the catalytic performance.[72,78]

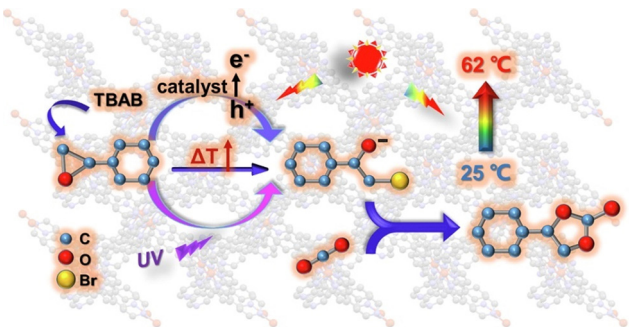

Fig. 4 Proposed mechanism of the synthesis of styrene carbonate *via* the CO_2 cycloaddition reaction by the photothermal catalyst FeTPyP. Reproduced with permission from ref. 68. Copyright 2022 Elsevier.

First, the coordination modulation of a single atom can be realized in MOF-based photocatalysis.[79,80] Zr-based MOFs are intensively utilized for the construction of single-atom catalysts (SACs) due to the presence of neighboring surface-O/OH_x sites at Zr_6-oxo clusters, allowing the anchoring of extraneous metal species.[81,82] With the help of microwave, Ma *et al.* developed a simple and general method to immobilize various single atoms, such as Ni(II), $Co(II)^{2+}$, and $Cu(II)^{2+}$, onto the Zr_6-oxo clusters of different Zr-MOFs.[74] Interestingly, following hydroxylation, sulfonation, or further oxidation, the coordination environments of these single-atom metals were flexibly modulated (Fig. 5a), affording representative Ni_1-X/UiO-66-NH_2 (X = S, O, S_{ox}; ox, oxidation) photocatalysts. The results show that Ni_1–S/UiO-66-NH_2 possessing a reductive oxidation state has a lowest proton activation barrier, leading to the highest photocatalytic activity for H_2 production, which is 270 times that of the pristine MOF.

In addition, the modulation on the second coordination sphere interactions to improve the catalytic efficiency mimicking the supramolecular systems has been fulfilled in MOF-based photocatalysis.[76] It is known that interactions extending beyond the primary coordination sphere can contribute to the enhancement of the catalytic activity and/or selectivity.[84] Rayder *et al.* prepared a host–guest composite *via* the noncovalent encapsulation of a ruthenium complex into the pores of various functionalized UiO-66-X (X = CH_3, F, Br, NO_2, NH_2, NH_3^+, 4F) hosts to study the influence of the outer sphere on the catalytic activity induced by the modulated host–guest interactions.[76] UiO-66-NH_3^+ was found to possess the highest efficiency in CO_2 hydrogenation to methanol, benefiting from the ammonium functional group in close proximity to the encapsulated catalyst.

Moreover, by simply changing the –X groups on UiO-X shell of the sandwich-structured MOF@Pt@MOF, microenvironments of the UiO-66-NH_2 photosensitizer and Pt cocatalyst were simultaneously modulated.[83] A mechanistic study revealed that with the gradual increase in the electron-withdrawing capacity of the –X group ($-OCH_3$ < –NA < –H < –Br < –Cl < $-NO_2$), the charge separation efficiency (η_2) of the UiO-66-NH_2 core, as evaluated by the exciton binding energy (E_b), increased; while the intrinsic reduction efficiency (η_3) of Pt, as indicated by the electrochemical H_2 evolution reaction (HER), decreased (Fig. 5b). The relationship between the H_2 production activity and the electron-

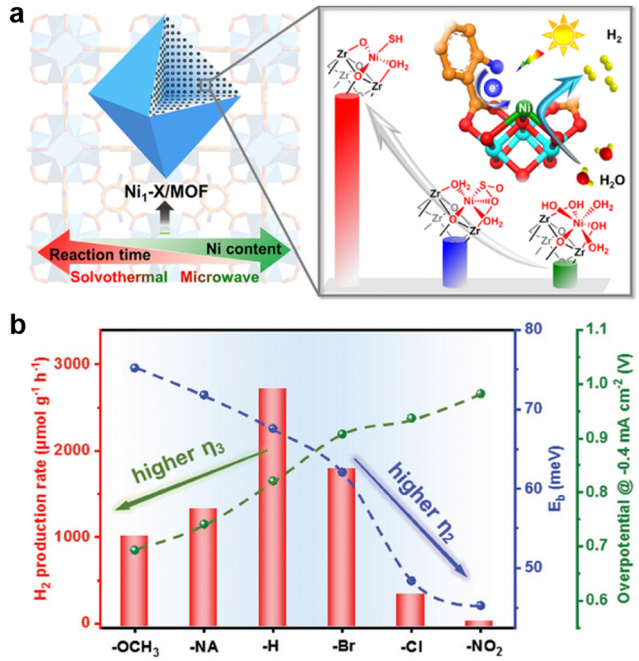

Fig. 5 (a) Schematic illustration showing the fabrication of coordination environment-modulated Ni_1–X/UiO-66-NH_2 with different photocatalytic H_2 production activities. Adapted with permission from ref. 74. Copyright 2021 ACS. (b) The E_b and overpotential (for HER)-dependent H_2 production rate of UiO-66-NH_2@Pt@UiO-66-X with changed –X groups to modulate the coordination environment. Adapted with permission from ref. 83. Copyright 2023 Wiley.

withdrawing/donating ability of the –X groups is nonlinear. Furthermore, Xu *et al.* encapsulated three different Pt cocatalysts into UiO-66-NH_2, with the microenvironment modulated by capping or partially removing polyvinylpyrrolidone (PVP or rPVP).[85] The presence of PVP decreased the electrical conductivity and hampered the electron transfer between MOF and Pt, resulting in greater photocatalytic H_2 activity of Pt@UiO-66-NH_2 than that of Pt_{PVP}@UiO-66-NH_2 and Pt_{rPVP}@UiO-66-NH_2.

3.2. Multivariability

The prerequisite for developing bi- or multifunctional catalysis is the incorporation of different catalytic centers into a single catalyst, which can cooperatively catalyze sequential, stepwise, tandem, *etc.*, reactions.[86] Due to their structural designability, chemical variety, and inherent rigidity, MOFs are very promising catalysts for multivariate catalysis, including photo(thermal) catalysis, *via* synergistic effects. The synthesis of multivariate (MTV)-MOFs by mixing ligands was first reported by Yaghi and coworkers, wherein up to eight functionalities can be successfully integrated into MOF-5.[87] Since then, the introduction of multiple functionalities into MOFs to realize the potential of MOFs for multivariate catalysis has attracted increasing attention.[88–90] For instance, by combining the dynamic spacer installation approach with metal chelation and covalent postmodification processes, Cao *et al.* installed ligands with different lengths into the robust prototype MOF LIFM-28 for the construction of MTV MOFs.[91] These MTV MOFs show activity in different catalytic reactions as well as in multivariate catalysis of sequential or stepwise reactions.

Based on reticular chemistry, MTV MOFs can be synthesized by using a mixture of ligands that have the same geometry and metrics but distinct lengths and degrees of functionalization.[92] This is vital in MOF-based photocatalysis because it allows bandgap modulation to influence key photocatalytic processes and pore size modulation to modify the substrate diffusion. Bryant *et al.* presented a MTV library of Ti-MOFs (Fig. 6a and b), in which eleven isoreticular hex rod-packed MOFs named UCFMTV-*n* and UCFMTV-*n*-*x*% with the formula Ti_6O_9[links]$_3$ were successfully prepared (*n* is the number of *p*-arylene rings in the linear oligo-*p*-arylene dicarboxylates, and *x*% is the percentage of multivariate links with electron-donating groups).[93] Benefiting from the varied linker sizes and amine electron-donating group functionalization, the pore sizes and energy gaps of these MTV MOFs are well regulated, and their effects on the photooxidation of benzyl alcohol were studied in detail (Fig. 6c). As a result, UCFMTV-4–30%, which has the longest pore size and an appropriate content of electron-donating groups, exhibited the highest turnover rate, which is approximately 18-fold faster than that of the representative Ti-MOF photocatalyst MIL-125 (Fig. 6d).

To realize synergistic light harvesting, charge carrier separation and transfer processes, Zhang *et al.* organized photosensitive and photothermal units uniformly into a single MOF.[94] The solvothermal reactions of $HoCl_3{\cdot}6H_2O$, $Cd(OAc)_2{\cdot}4H_2O$, and different ratios of $NiCl_2{\cdot}6H_2O$ with the organic ligand 3-fluoropyridine-4-carboxylic acid (HFNA) afforded a stable 3D framework, named Ho_6–Cd_xNi_{1-x}–N_4, with a (4,12)-connected ftw topology (Fig. 7a and b). After simple sulfurization at 120 °C by using different amounts of thioacetamide, Ho_6–Cd_xNi_{1-x}–NS integrated with well-dispersed photosensitive Cd–NS and photothermal Ni–NS single sites was obtained (Fig. 7c). Upon light absorption of the connected FNA^- ligands, abundant photoelectrons generated around the photosensitive Cd–NS sites first transferred to the Ho_6 clusters and then to adjacent photothermal Ni–NS sites (Fig. 7d). Benefiting from the ultrashort molecule-scale electron transfer path, the suppressed recombination of the photoinduced charge carriers and the facilitated reaction rate by the presented photothermal effect, Ho_6–$Cd_{0.76}Ni_{0.24}$–NS exhibited a boosted H_2 production rate of 40.06 mmol g^{-1} h^{-1}.

3.3. Steric effects

Steric effects are often invoked as a feature of nanoporous materials that can affect the catalytic activity and selectivity.[95] In contrast to traditional porous materials, such as zeolite anmesoporous silica, one unparalleled advantage of MOFs for catalysis is their highly adjustable physical/chemical environments (organic ligands, metal centers, pore sizes or pore shapes), which are promising platforms for regulating steric effects to realize target catalysis.[96–99] It is acknowledged that the aperture and shape of MOFs play complementary roles in controlling steric effects.[100]

For instance, Wei *et al.* realized precision syntheses by utilizing the pore confinement effect of MIL-88B, a Fe(III)

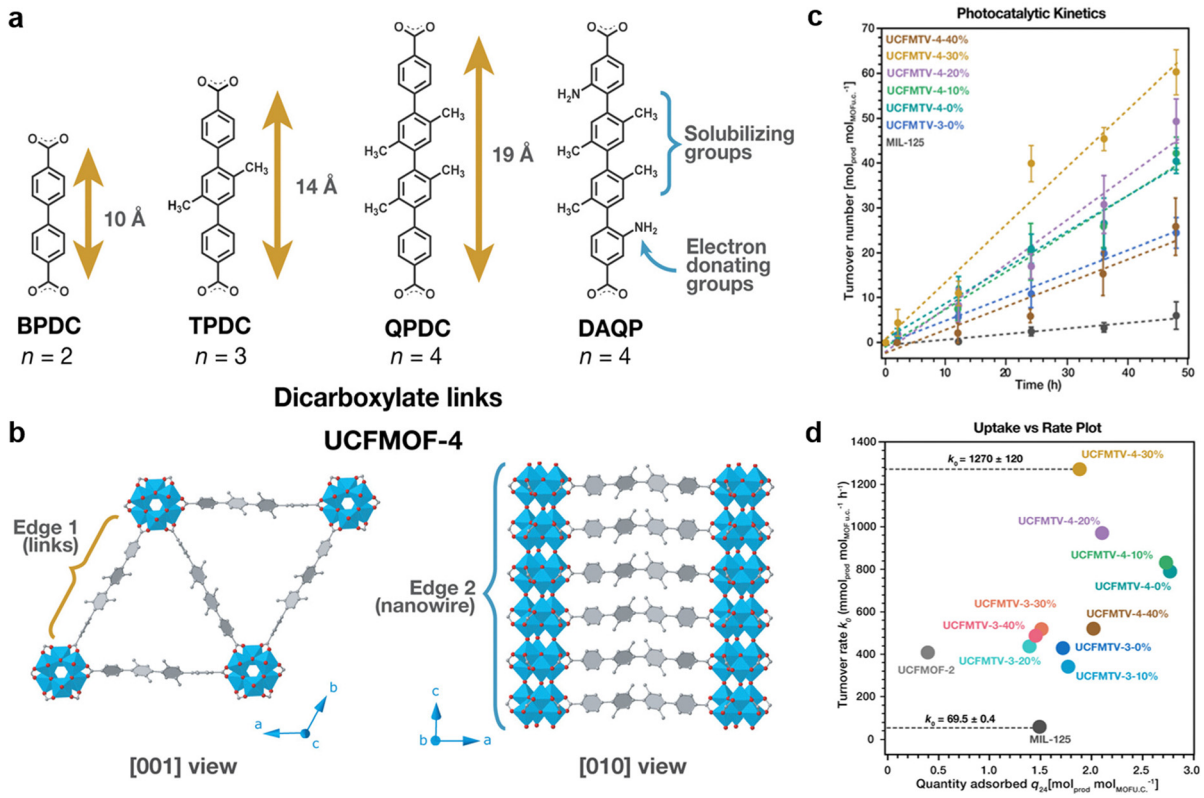

Fig. 6 (a) Different dicarboxylate ligands used for the fabrication of UCFMTV-*n*-*x*%. (b) Crystal structure of UCFMOF-4 viewed from the [001] and [010] directions. (c) Photocatalytic kinetic plots for benzyl alcohol oxidation and (d) relationship between the substrate uptake at 24 h (q_{24}) and turnover frequency (k_0) over the different photocatalysts. Adapted with permission from ref. 93. Copyright 2023 ACS.

dicarboxylate framework wherein a regular triangle is defined by every three adjacent Fe(III) ions located on the same channel.[96] The highly oriented coordination bond arrangement of the octahedral Fe(III) ions can contribute to the fixation of three molecules for the [2+2+2] coordination-templated cyclotrimerization reaction. Bing *et al.* anchored single-site Cu^{I} active metal centers and alkali metal Cs^{+} onto the deprotonated $[Zr_{12}O_8(\mu_3\text{-}O\text{-})_8(\mu_2\text{-}O\text{-})_6(\text{carboxylate})_{18}]^{14-}$ secondary building units (SBUs) of a Zr_{12}-MOF.[97] In this Cu- and Cs-integrated MOF, the spatially proximate bimetallic Cu^{I}_2 centers can prompt the activation of H_2 *via* bimetallic oxidative addition as well as the direct C–C coupling of methanol and formyl species. Yang *et al.* prepared a Pd nanocube (NC)@ZIF-8 composite with a core–shell structure and demonstrated that it was an efficient photothermal catalyst for the hydrogenation of olefins upon light irradiation because of the excellent photothermal effects of Pd NCs.[98] Furthermore, because the ZIF-8 shell has a well-defined pore structure that can function as a molecular sieve, selective hydrogenation of olefins with specific sizes on the Pd NC@ZIF-8 composite can be realized (Fig. 8). These examples offer the opportunity to enhance the activity and selectivity of MOF-based photo(thermal) catalysis by rationally employing steric effects.

3.4. Defect and facet engineering

Traditionally, perfect MOFs, in which the metal motifs and organic ligands are perfectly coordinated, are highly pursued to fully exploit their potential for multifunctional applications. Nevertheless, defective MOFs have been demonstrated to be prevalently formed in general synthetic processes due to the uncoordinated metal and ligands or vacancies in the framework. Unexpectedly, defective MOFs frequently exhibit superior activity in contrast to their perfect counterparts in various fields because of their increased porosity and abundant active sites.[101–105] Thus, the defects of MOFs can also be utilized as an additional dimensionality to tailor the MOF photo(thermal)-catalytic performance.[106–111] For instance, Wang *et al.* optimized the CO_2 photoreduction performance of UiO-66-NH_2 by tailoring its defect type and ligand vacancy degree. In their work, by simply regulating the molar ratio of the defect modulator (formic acid, FA) to the carboxylate ligand, UiO-66-NH_2 with different defect types and varied degrees of ligand vacancies can be obtained.[107] With increasing FA molar equivalent, the defect type changed from missing-linker (ML) to missing-cluster (MC), and the ligand vacancy degree also increased after thermal treatment of the samples to remove the thermolabile modulator FA. It was found that the ML defect decreased the Zr atom-dominated LUMO energy, while the MC defect increased the absorption energy. As a result, ML UiO-66-NH_2-ML-100 with a ligand vacancy exhibited the best activity toward CO_2 photoreduction.

Very recently, by using different powers of Ar radio frequency plasma, Wang *et al.* prepared Fe-based MOF catalysts with regulated defects of terminal inorganic ligands (OH^- and H_2O) and/or bridging organic ligands, which can result in the

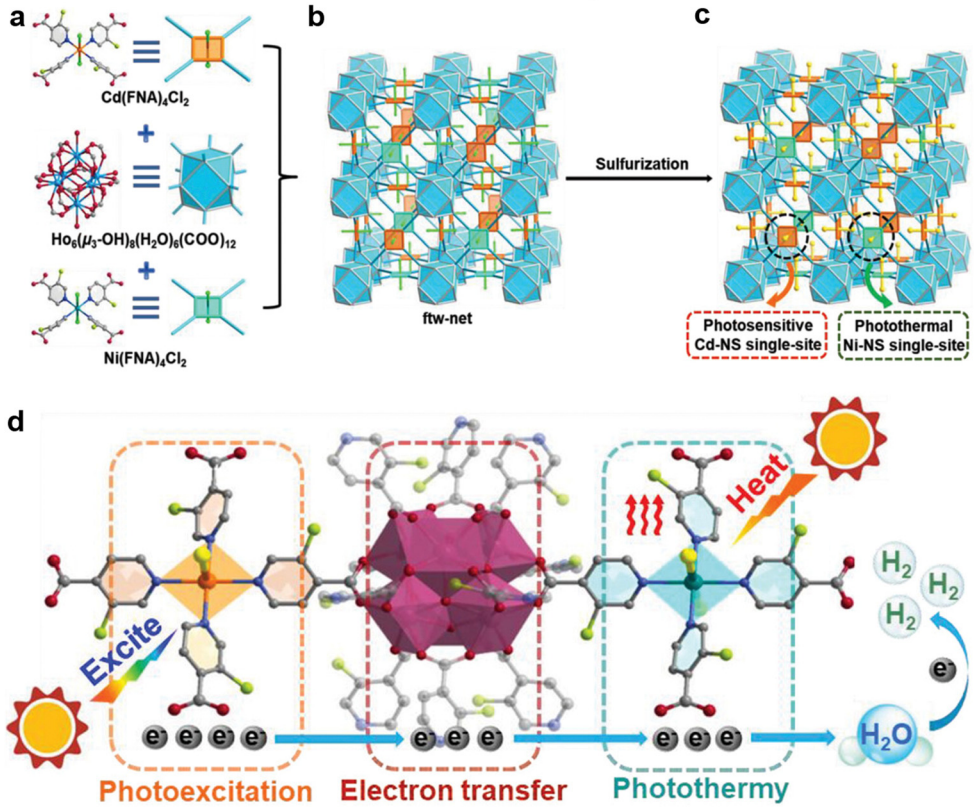

Fig. 7 (a) Secondary building units in Ho_6–Cd_xNi_{1-x}–N_4, topological structures of (b) Ho_6–Cd_xNi_{1-x}–N_4 and (c) Ho_6–Cd_xNi_{1-x}–NS, and (d) proposed reaction mechanism and electron transfer path in Ho_6–Cd_xNi_{1-x}–NS under light irradiation. Adapted with permission from ref. 94. Copyright 2024 Wiley.

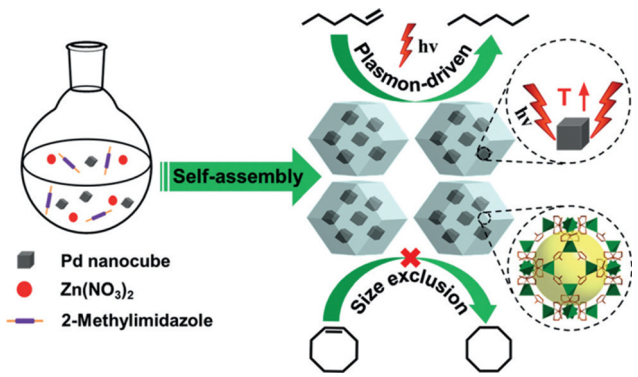

Fig. 8 Schematic illustration showing the synthesis of Pd NCs@ZIF-8 and its photothermal effect-driven selective hydrogenation of olefins. Reproduced with permission from ref. 98. Copyright 2016 Wiley.

generation of different coordinatively unsaturated Fe centers (Fig. 9a).[111] Compared to the pristine MIL-100(Fe) with a nonporous compact surface, the MIL-100(Fe) samples, which were treated by plasma at powers of 50, 100, 200, and 300 W for 10 min, became highly porous. The different thermal behaviors of MIL-100(Fe) and MIL-100(Fe)-200 W (Fig. 9b) indicated that the defects of the former are only terminal inorganic ligands, while those of the latter are dominated by both terminal inorganic ligands and bridging organic ligands. The NH_3 synthesis activity of these plasma-treated photocatalysts from N_2-saturated water was proven to be dependent on the defect type and degree in the catalysts (Fig. 9c). The best activity of MIL-100(Fe)-100 W is due to the abundant exposed coordinatively unsaturated Fe sites induced by the dual defects, which possess different local electron structures to reduce the energy barrier of the rate-limiting step of N_2 reduction.

Facet engineering is an efficient approach for exposing various atomic arrangements on the surface of metal and metal oxide catalysts to modulate the kinetics and activity of catalytic reactions.[112–115] With regard to photocatalysis, through facet engineering, the light harvesting, surface electronic structure, and transport efficiency of surface electrons, which are vital for determining the photocatalytic performance, can be regulated.[116–118] Due to their crystalline structures and diverse active sites on different facets, MOFs have the potential to expose specific facets with more reactive sites for specific reactions through facet engineering. To date, facet engineering *via* simply controlling the morphology of MOFs, such as ZIF-8, MOF-5, and HKUST-1, has been realized.[119–123] For example, by using a crystal engineering method, Yang *et al.* prepared a bulky Ni-MOF and two nickel metal–organic layers (Ni-MOLs) with different exposed crystal facets, named Ni-MOL-100 and Ni-MOL-010 with abundant exposed (100) and (010) facets, respectively.[119] When used as photocatalysts for CO_2 photoreduction, Ni-MOL-100 exhibited an obvious increased catalytic activity for converting

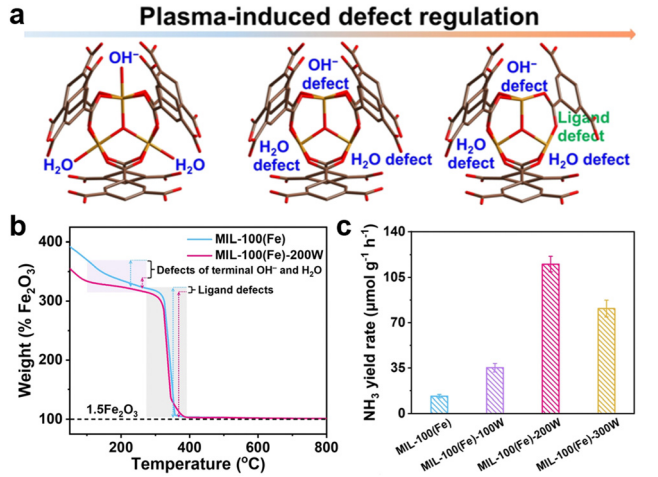

Fig. 9 (a) Schematic illumination showing the plasma-assisted fabrication of MOF photocatalysts with different types of defects. (b) Thermal behavior study of MIL-100(Fe) and MIL-100(Fe)-200 W. (c) Photocatalytic NH_3 yield rates over plasma-treated MIL-100(Fe) samples with different powers. Adapted with permission from ref. 111. Copyright 2024 Wiley.

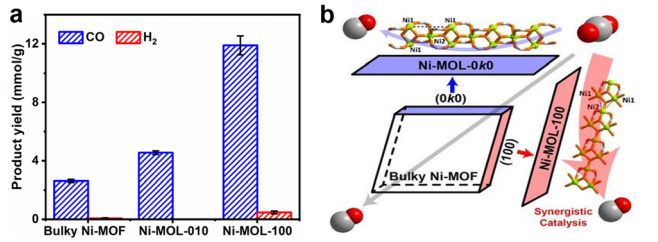

Fig. 10 (a) Facet-dependent photocatalytic activity for CO_2 reduction over Ni-MOFs and (b) the proposed mechanism for the excellent performance of Ni-MOL-100. Adapted with permission from ref. 119. Copyright 2021 Wiley.

CO_2 to CO compared with that of Ni-MOL-010 and bulky Ni-MOF (Fig. 10a). Results show that the excellent performance of Ni-MOL-100 is due to the synergistic catalysis provided by the two coordinatively unsaturated and close (3.50 Å) nickel sites on the surface of the (100) facet (Fig. 10b).

4. Strategies for improving MOF-based photo(thermal) catalytic performance

Because MOFs are assembled by metal nodes with organic linkers, the photocatalytic activity of MOFs can come from either the metal nodes and/or the organic ligands. For example, pristine zirconium, titanium, iron, or cerium oxo cluster-based robust MOFs have been intensively utilized as photocatalysts because of the intrinsic photoactivity of these types of clusters, which can evoke the formation of ROS and trigger electron transfer reactions.[124–126] Meanwhile, when photoactive molecules, such as porphyrin, pyrene, and anthracene, are adopted as organic linkers, the prepared pristine MOFs also show catalytic activity for various photochemical reactions.[127–129] Although the direct use of pristine MOFs as photocatalysts is very promising because of their facile synthetic processes and they can also provide good platforms for studying structure–activity relationships, their application in photocatalysis is still restricted for their limited light harvesting, charge generation and separation, and reaction activities. To further optimize the photocatalytic activity and widen the application field of pristine MOF photocatalysts, various modification/composite strategies are commonly introduced.[35,130–132] According to the general photo(thermal) catalytic mechanism and unique advantages of MOF-based photo(thermal) catalysts,[24–28] herein, several representative strategies from the perspectives of structural functionalization of MOFs and the fabrication of MOF-based composites with the aim of improving three intrinsic key photocatalytic processes and photothermal effect to enhance the photo(thermal) catalytic performance are listed.

4.1. Structural functionalization of MOFs

4.1.1. Functionalization of organic ligands. In contrast to the inorganic metal sites within MOFs, which are viewed as semiconductor quantum dots, the organic linkers within MOFs commonly serve as light-harvesting antennae to stimulate and conduct charge carriers. Therefore, organic ligand functionalization is a rational and simple method for obtaining efficient MOF-based photo(thermal)catalysts with a high light response.[133–138]

Typically, organic ligands can be functionalized by *in situ* or postmodification methods. First, ligand functionalization can be achieved in the *in situ* preparation of MOFs.[139,140] For example, Qiu *et al.* prepared a series of Ce-UiO-66 MOFs to evaluate the effect of functionalized ligands on photocatalytic activity.[133] Results show that the ligand functionalization had an obvious effect on the bandgaps and valence band (VB) potentials of these

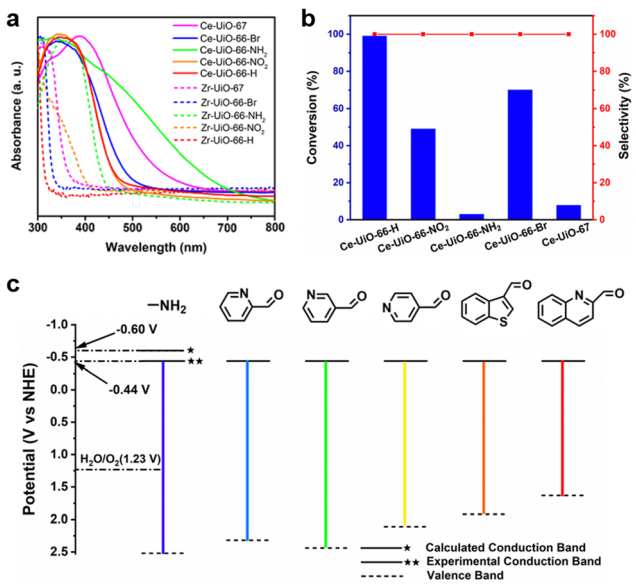

Fig. 11 (a) UV-vis diffuse reflectance spectra and (b) photocatalytic activities of various Ce-UiO-66 MOFs. Adapted with permission from ref. 133. Copyright 2020 Wiley. (c) Bandgaps of NH_2-MIL-125(Ti) grafted with different aromatic heterocycles. Adapted with permission from ref. 134. Copyright 2018 Elsevier.

photocatalysts (Fig. 11a and b). When used for photocatalytic oxidation of benzyl alcohol, Ce-UiO-66-H, Ce-UiO-66-NO_2 and Ce-UiO-66-Br that possess more positive VB potentials than benzyl alcohol (1.88 V *vs.* NHE), offered better substrate conversions. In contrast, Ce-UiO-66-NH_2 and Ce-UiO-67, which have more negative potentials, exhibited much lower conversions.

Ligand functionalization can also be realized by postmodification of MOFs. To extend the light absorption, Wu *et al.* provided NH_2-MIL-125(Ti) MOFs modified with different aromatic heterocycles *via* a facile postgrafting strategy of the Schiff base chemical reaction.[134] Density functional theory (DFT) calculations were adopted to study the effect of postgrafting on the band gap structures (Fig. 11c), which showed that QUI-MIL-125(Ti) (QUI = 2-quinolinecarboxaldehyde) had the narrowest band gap and the best visible light absorption, benefiting from the strong conjugation of QUI with NH_2-MIL-125(Ti). This result was also supported by the calculated HOMO and LUMO of the aromatic heterocycle-grafted MOFs. The photocatalytic tests of oxidation of benzyl alcohol suggested that these modified MOFs all had significantly enhanced activity over pristine NH_2-MIL-125(Ti), particularly QUI-MIL125(Ti), which showed the highest photoactivity (88% conversion) and can be successfully applied to various substituted alcohols.

In addition to improving the light harvesting of MOFs, the ligand functionalization strategy is also capable of enhancing the CT and/or EnT processes in photocatalysis. The use of a single MOF ligand with donor–acceptor–donor characteristics or two MOF ligands, one of which is an electron/energy donor and the other is an electron/energy acceptor, can result in donor–acceptor MOFs (D–A MOFs).[141–145] Upon irradiation, D–A MOFs with excellent light harvesting, charge separation and mobility, and long e^-–h^+ pair lifetimes can exhibit superior photocatalytic activity. Jin *et al.* prepared a D–A–D-type pyrazole–benzothiadiazole–pyrazole organic ligand with a conjugated π-system and used it to construct the robust D–A MOF photocatalyst JNU-204 (Fig. 12a).[141] Because of its good light absorption, appropriate band gap, and rapid charge separation, as evidenced by the optical and electrochemical characterization results, JNU-204 exhibited exceptional photocatalytic activity for three types of aerobic oxidation reactions. Recently, Xu *et al.* prepared a D–A MOF (Zr-NDI-H_2DPBP) *via* integrating an electron donor porphyrin ligand (5,15-di(*p*-benzoato)porphyrin, H_2DPBP) into an electron acceptor naphthalene diimide (NDI)-based Zr-MOF (Zr-NDI) based on the two dicarboxylic ligands with similar lengths (Fig. 12b).[142] The experimental and theoretical calculation results indicated that abundant ROS $O_2^{\bullet-}$ and $^1O_2$ were generated due to the efficient photoinduced electron transfer (PET) from H_2DPBP to NDI and the EnT process provided by the photosensitized H_2DPBP upon irradiation, respectively. As a result, Zr-NDI-H_2DPBP showed a boosted imine generation rate of up to 136 mmol g^{-1} h^{-1}.

Using energy donors and acceptors as ligands to construct mixed-ligand MOFs is also an ingenious route to building D–A MOFs but is still a major synthetic challenge. Fiankor *et al.* integrated the secondary porphyrin acceptor ligand H_2TCPP/NiTCPP (TCPP = meso-tetrakis(4-carboxyphenyl)porphyrin) into

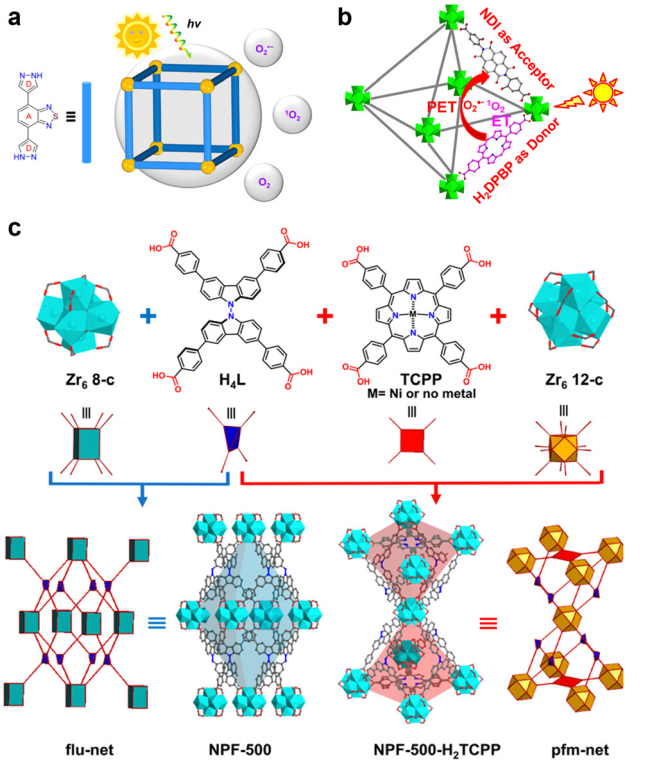

Fig. 12 (a) A D–A–D-type ligand-based D–A MOF JNU-204 for photocatalytic aerobic oxygenation. Adapted with permission from ref. 141. Copyright 2021, ACS. (b) PET and EnT processes over the D–A mixed-ligand MOF Zr-NDI-H_2DPBP. Adapted with permission from ref. 142. Copyright 2023 ACS. (c) The formation process of NPF-500 and D–A MOF NPF-500-H_2TCPP/NiTCPP. Adapted with permission from ref. 143. Copyright 2021, ACS.

a photosensitive *N*,*N*′-bicarbazole (donor)-based Zr-MOF NPF-50 (NPF = Nebraska porous framework).[143] Due to the presence of coordinatively unsaturated metal sites in the equatorial planes of the octahedron cages, H_2TCPP/NiTCPP was placed precisely into the framework of NPF-50 (Fig. 12c). Benefiting from the high degree of spectral overlap between the emission spectrum of *N*,*N*′-bicarbazole and the absorption spectrum of porphyrin, an efficient EnT process can occur upon light irradiation, contributing to the improved photoactivity for oxygenation of thioanisole.

4.1.2. Functionalization of metal nodes. Metal nodes possess coordinatively unsaturated sites that can function as redox and/or Lewis acidic active sites for catalyzing a wide range of organic transformations.[146] However, the metal nodes in MOFs often have limited functionality as single metal sites, restricting the application in photocatalysis. The exposed unsaturated metal nodes are usually saturated by –OH/–OH_2 groups that are conducive to incorporate active species, allowing node functionalization toward "*de novo*" synthesis and postsynthetic treatment.[147] The immobilization of additional metal ions and/or the photoactive species at the MOF nodes are the two essential functionalization strategies for improving photocatalytic performance.[148]

It has been reported that additional metal ions can be incorporated at MOF nodes to prepare the heterometallic MOFs

or the mixed-metal MOFs. Within the past two decades, the introduction of different metal ions into the MOF nodes to construct heterometallic MOFs has been regarded as an effective method to enrich the topology type and improve the physical and chemical properties of MOFs.[149] Commonly, heterometallic MOFs are prepared either through "*de novo*" synthetic or postsynthetic ion-exchange approach. For instance, based on the "*de novo*" synthesis by using metal ions with similar ion radius and Coulomb charge, Wang *et al.* synthesized five heterometallic MOF-74 with two, four, six, eight, and ten divalent metal cations, respectively.[150] In their continuing work, the sequences of some cations within these heterometallic MOF-74 were also revealed *via* the use of atom-probe tomography.[151] Benefiting from the synergy of different metal ions, heterometallic MOFs have been demonstrated to exhibit better performance in fields of adsorption, catalysis, magnetism, *etc*, than their monometallic MOFs, although their long-term stability and large-scale preparation methods are still limited.[149]

Due to better overlap with the π* orbital of the organic ligand, mixed-metal MOFs facilitate the generation of charge-separated states with long lifetimes for enhanced photocatalysis.[152] Bhattacharyya *et al.* constructed series of Ce- and/or Ti-doped UiO-66-NH_2-type MOFs.[153] The spectroscopic and photodynamic tests revealed an improved ligand-to-cluster charge transfer (LCCT) process in the Ce- and Ce/Ti-doped MOFs, and deactivation of the intramolecular charge transfer (ICT) process was also evidenced by fs-upconversion experiments. A more efficient LCCT rather than ICT and increased long-lived charges within mixed-metal MOFs leads to higher activity toward the photocatalytic degradation of the pollutant dye Nile blue. In addition, trimetallic MOFs, wherein a multi-electron-channel system can be constructed to accelerate the separation of charge carriers, have shown potential in efficient photocatalytic organic transformations.[94] For instance, Melillo *et al.* measured the photocatalytic water splitting performance of five UiO-66 samples containing one, two, or three different metal ions on the metal clusters, the results demonstrated that the trimetallic UiO-66(Zr/Ce/Ti) exhibited the highest efficiency benefiting from its enhanced charge separation efficiency for the oxygen evolution half reaction.[154]

Metal node functionalization with photosensitive species has also been utilized to improve the visible light absorbance of MOFs. By microwave-assisted coordinative binding of Fe(III) ions to the Zr-oxo clusters of UiO-6, Xu *et al.* prepared a MOF-based photocatalyst, denoted as Fe-UiO-66, for selective inert C–H bond oxidation (Fig. 13a).[155] Studies indicated that $Fe(III)^{3+}$ was stabilized on the metal nodes *via* Fe–O–Zr connections. Fe(III) modification affects the electronic structure of UiO-66, in which the intrinsic absorption edge redshifts, indicating an extended visible light response range. In addition, due to the metal-to-cluster charge transfer (MCCT) from Fe(III) to Zr-oxo clusters, the holes generated from Fe-UiO-66 exclusively oxidize H_2O to •OH (Fig. 13b), which possesses adequate oxidizing capacity to activate stubborn C–H bonds. Moreover, $O_2^{\bullet-}$ also forms due to O_2 get electrons easily in this system, which further promotes the oxidation process. As a result, toluene was selectively oxidized to benzoic acid (Fig. 13c).

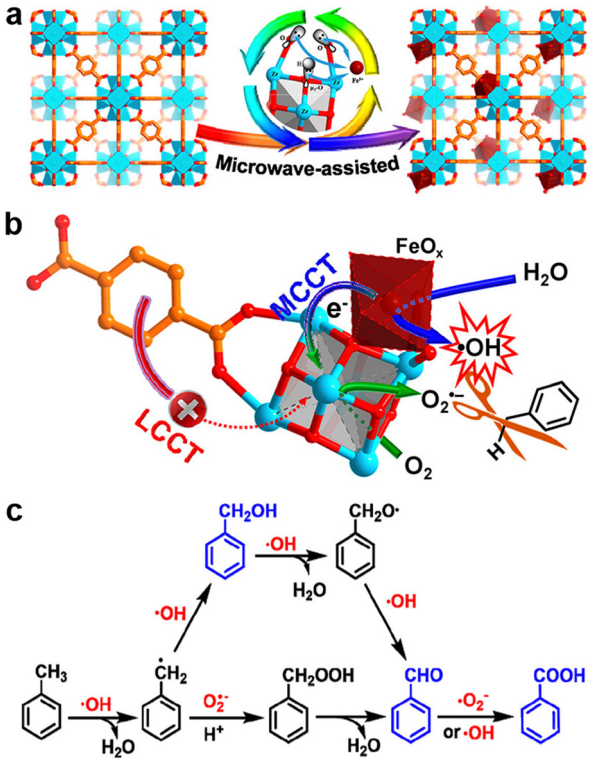

Fig. 13 Schematic illustration of (a) the synthesis, (b) the photoinduced MCCT process, and (c) proposed mechanism of toluene oxidation on Fe-UiO-66 with grafted FeO_x on the Zr-oxo cluster. Adapted with permission from ref. 155. Copyright 2019 ACS.

Postmodification of reticular MOFs is an appealing approach for realizing metal node functionalization in confined spaces.[156] Gutiérrez *et al.* prepared two novel MOF photocatalysts by anchoring two different photosensitizers, perylene-3-carboxylic acid (PC1) and perylene-3-butyric acid (PC2), into MOF-520 *via* a postfunctionalization route.[157] Fortunately, the good spatial distribution of perylenes inside the MOFs was supported by the single structure of MOF-520-PC1, which allowed in-depth study of the photophysical properties and mechanism. The results showed that both the photocatalysts exhibited excellent activity for the C–C bond reductive dimerization reaction, because the highly distributed perylenes within the MOFs could function as single units that avoid easy aggregation.

4.1.3. Pore space functionalization. MOFs are porous materials featuring tuned pore parameters, such as porosity, pore size and shape, and pore distribution, which allow functionalization with photosensitive species and/or additional active sites for improving photocatalysis. On the one hand, homogeneous photosensitive species can be heterogenized by MOF cage encapsulation, leading to modified light harvesting and efficient spatial separation of charge carriers.[158,159] On the other hand, additional active sites, such as metal NPs and semiconductors with very small particle sizes,[160] can be introduced into the MOF pore space, forming heterojunctions with matched energy levels to improve charge separation. Broadly speaking, ligand functionalization and metal node functionalization that occur in the pore space can all be categorized as pore functionalization, which will

not be repeated here.[161] This section focuses on the functionalization that has the greatest influence on the pore environment, where there is no direct interaction/connection between guest species and the ligands/metal nodes of MOFs.

Photosensitizers are widely used as photocatalysts to initiate organic conversion due to their good absorption properties and long lifetimes of excited states.[162–166] The encapsulation of photosensitizers into MOFs is thus vital for enhancing the photocatalytic activities of MOFs,[156,167–170] and fortunately, this can be realized by pore space functionalization. For example, Lü *et al.* adopted a partial ligand substitution approach to encapsulate the metallophthalocyanine molecule Zn-H_4Pc (H_4Pc = 2,9,16,23-tetrakis(4-pentyloxycarbonyl)-phthalacyanine), which has excellent light-harvesting ability, into the pore of UiO-67 (Fig. 14a).[167] Under the synergistic effect of separated h^+ and e^- generated by the photoexcited ZnPc moieties, UiO-67-ZnPc exhibited remarkably promoted photocatalytic activity in the oxidation of 1-naphthol with a high 1,4-naphthoquinone yield (97%) and selectivity (>99%), while the pristine UiO-67 was almost inactive.

A versatile template-directed synthesis approach using homogeneous photosensitizers as the structure-directing templates was developed by Yang *et al.* to prepare new types of MOF photocatalysts with encapsulated photosensitizers.[168] For example, a polypyridine ruthenium(II) complex, denoted as $[Ru\text{-}(bpy)_3]^{2+}$ (bpy = 2,2′-bipyridine), can be successfully immobilized into a series of MOFs with zeolite-like structures (Fig. 14b). Due to the well-dispersed photosensitive $[Ru\text{-}(bpy)_3]^{2+}$ and the facilitated mass transport induced by the high porosity of MOFs, the obtained Ru(bpy)$_3$@MOFs exhibited outstanding photocatalytic activity for the oxidation of benzyl halides and cyclization of tertiary anilines and maleimides.

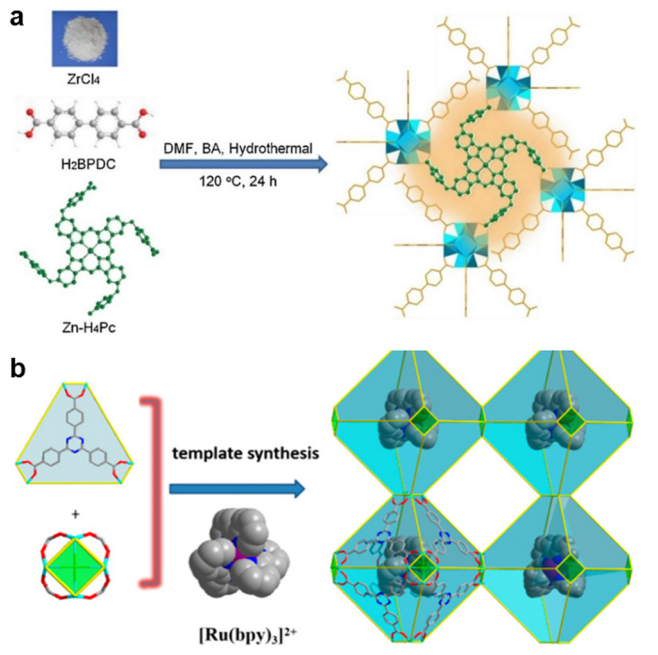

Fig. 14 (a) The incorporation of Zn-H_4Pc into MOF UiO-67. Adapted with permission from ref. 167. Copyright 2020 Elsevier. (b) The template-directed preparation of zeolite-like MOFs with an encapsulated photosensitizer. Adapted with permission from ref. 168. Copyright 2019 ACS.

Additionally, a series of dyes@UiO-66s were developed by encapsulating fluorescein (FL), rhodamine B (RhB), or eosin Y (EY) into the pore spaces of UiO-66 and Bim-UiO-66.[171] Highly stable dyes can efficiently sensitize MOF hosts, which has an important effect on band structures and the corresponding photocatalytic performances. Amongst, FL@Bim-UiO-66 was demonstrated to exhibit superior activity for the green synthesis of various [1,2,5]thiadiazole[3,4-*g*]benzoimidazoles with excellent yields (>98%), stability, and reusability.

Pore space functionalization of MOFs through integration with bimetallic NPs is a potential approach to optimize the photocatalytic properties of MOFs.[172] For example, Sun *et al.* encapsulated bimetallic CuPd nanoclusters into the pore space of NH_2-UiO-66(Zr) by combining the double-solvent impregnation method with a chemical reduction process.[173] The encapsulated Cu acted as an electron mediator to promote the electron transfer from photoexcited MOF to metallic Pd. As a result, CuPd@NH_2-UiO-66(Zr) exhibited improved photocatalytic activity in contrast to the single metal-loaded Pd@NH_2-UiO-66(Zr) for Suzuki coupling reactions.

Keggin-type polyoxometalates (POMs) have been demonstrated to be good catalysts for CO_2 cycloaddition reactions, but their wide application is limited by their low recycling stability and high energy input.[174] Fang *et al.* functionalized the pore space of a Zr–ferrocene (Zr–Fc) MOF with PMo_{12} (phosphomolybdate, $PMo_{12}O_{40}^{3-}$) *via* electrostatic interactions.[175] Combining the abundant Lewis sites provided by PMo_{12} with the outstanding photothermal effect of Zr–Fc MOF, the resulting PMo_{12}@Zr–Fc MOF catalyst exhibited significant photothermal catalytic activity and recycling stability for CO_2 cycloaddition under mild conditions.

4.2. MOF-based composites

4.2.1. MOFs with metal nanoparticles (NPs). Metal NPs are considered to integrate with MOFs to optimize the photocatalytic activity mainly because of the following aspects:[85,173,176–186] (1) NPs with surface plasmon resonance can extend light harvesting while maintaining their redox capacity; (2) Schottky junctions are sometimes formed between MOFs and NPs, which are able to efficiently improve the charge carrier separation and transfer; and (3) the interaction between NPs and the support can mediate the electronic states of the metal and thus influence the catalyst.

Commonly, redox-inert supports are not suitable for catalysis resulted from their weak electronic interaction with metal species.[187,188] Sun *et al.* used inert or active MOF supports to anchoring Pt NPs and studied their photocatalytic performances.[176] Surprisingly, the activity of the inert MOF ZIF-8 composited with Pt NPs (Pt/ZIF-8) for the aerobic oxidative coupling of benzylamine (BA) was much greater than that of the reducible MOF composites Pt/UiO-66 and Pt/MIL-125 (Fig. 15). The experiments and theoretical calculations indicated that the higher Pt electron density in Pt/ZIF-8 was the reason for the higher photocatalytic activity, which mainly caused by Schottky junction-driven electron transfer from ZIF-8 to Pt and the irreversible electron injection to ZIF-8 by Pt interband excitation.

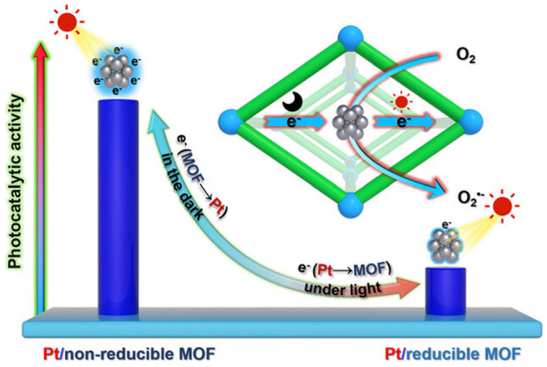

Fig. 15 The photocatalytic activity of the different Pt/MOF composites toward the oxidative coupling of BA. Reproduced with permission from ref. 176. Copyright 2022 Wiley.

This accounts for the superior activity of Pt/ZIF-8 to its counterparts *via* the stronger generation capacity of $O_2^{\bullet-}$.

By using an advanced double-solvent approach and then a reduction treatment carried out in a H_2/Ar atmosphere,[189] Xiao *et al.* successfully fabricated the noble-metal-free photocatalyst Cu/Cu@UiO-66 by simultaneously encapsulating Cu quantum dots (QDs) into the pores and loading CuNPs onto the surface of UiO-66.[177] The prepared CUO-0.1 (0.1 is the mass fraction of Cu in Cu/Cu@UiO-66) exhibited significantly promoted photocatalytic performance for the partial oxidation of aromatic alcohols. This can be contributed from the synergy of the plasmonic effect of CuNPs and Schottky junction between Cu QDs and UiO-66, facilitating the light absorbance and charge separation to generate abundant ROS of $O_2^{\bullet-}$.

The extra heat required for the nitroarene hydrogenation reaction with endothermic nature can be considered to be replaced by solar energy *via* the plasmonic effect of metal nanocrystals.[190] Wang *et al.* reported a simple dissolution/coordination method to encapsulate octahedral Cu_2O nanocrystals in a typical MOF, HKUST-1.[191] By carefully controlling the balance between Cu_2O etching and MOF shell growth, the oriented growth of HKUST-1 on Cu_2O nanocrystals can be realized. After *in situ* reduction of the obtained Cu_2O@HKUST-1 during NH_3BH_3 hydrolysis, a Cu@HKUST-1 composite photocatalyst with well-maintained morphology was obtained. Compared to the Cu/HKUST-1 sample synthesized by traditional methods, in which Cu nanocrystals are randomly deposited inside HKUST-1 particles, Cu@HKUST-1 exhibited better activity and cycle stability for the one-pot tandem synthesis of aromatic imines from nitrobenzene and benzaldehyde benefiting from the photothermal effect of Cu and the Lewis acidity of MOFs.

4.2.2. MOFs with semiconductors. Semiconductors have attracted much attention in photocatalysis since Fujishima and Honda first demonstrated photocatalytic water splitting in 1972.[192–195] The photocatalytic efficiency of MOFs could be improved through coupling with semiconductors to form composites with synergistic photocatalytic behaviors, especially those with heterojunction structures, where photoexcited e^-/h^+ can commonly efficiently migrate between each other's conduction/valence bands.[196–200] For example, as a typical semiconductor, CdS, which has a strong light-harvesting capacity in the visible light region, has been intensively utilized in photocatalysis.[201–203] Wu *et al.* encapsulated CdS QDs with several nanometers in size into the chromium-based MOF MIL-101 *via* a double-solvent strategy.[204] Compared to the pristine MOF, the obtained CdS@MIL-101 composite catalyst exhibited excellent performance in the synthesis of symmetrical or asymmetric imines *via* photocatalytic coupling of amines and alcohols or self-coupling of amines (Fig. 16). The outstanding activity of the composite photocatalyst is attributed to the promoted light absorption capacity as well as the strong interaction between CdS QDs and MIL-101, which contributes to the effective generation and separation of charge carriers.

Carbon nitride (C_3N_4), a polymer semiconductor, has been widely developed as a metal-free and green photocatalyst because of its excellent stability and simple synthesis.[205–209] It is also a potential candidate to composite with MOFs, for the improved photocatalytic properties.[210–213] For instance, by using a facile solvothermal method, Liu *et al.* successfully loaded highly stable UiO-66-NH_2 onto hexagonal phosphorus-doped tubular C_3N_4 (*p*-TCN).[214] Due to the improved light-harvesting capacity gifted by *p*-TCN as well as the efficient CT between *p*-TCN and UiO-66-NH_2, the achieved *p*-TCN@UiO-66-NH_2 photocatalyst exhibited good performance in the coupling of amines to imines.

Very recently, Daliran *et al.* encapsulated the nontoxic lead-free halide perovskite semiconductor $CsCu_2I_3$ into the channels of the highly stable mesoporous MOF PCN-222(Fe).[215] By adopting an antisolvent/inverse solvent infiltration method in which the MOF support and $CsCu_2I_3$ were used as precursors, $CsCu_2I_3$ was grown *in situ* and immobilized into the voids of PCN-222(Fe). The obtained composite $CsCu_2I_3$@PCN-222(Fe) was demonstrated to be a benchmark photocatalyst for a one-pot selective photooxidation/Knoevenagel domino reaction with O_2 (1 atm). Mechanistic studies indicated that the superior photocatalytic activity was derived from the cooperation and synergistic effects between $CsCu_2I_3$ and PCN-222(Fe), which

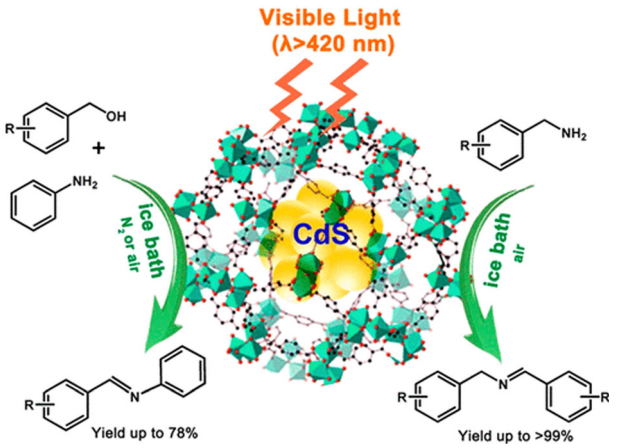

Fig. 16 The CdS@MIL-101 photocatalyst with excellent activity for the synthesis of symmetrical and asymmetric imines. Reproduced with permission from ref. 204. Copyright 2019 ACS.

supported the efficient generation of $O_2^{\bullet-}$ and $^1O_2$ in the photocatalytic system.

Semiconductor materials have obvious advantages for utilizing the near-infrared light of noble metal NPs due to their high extinction coefficient and wide band tunability.[216] For instance, copper chalcogenides with photothermal properties similar to those of gold NPs exhibit great potential in photothermal catalysis.[217] Wang *et al.* successfully constructed a well-defined core–shell Cu_7S_4@ZIF-8 nanostructure in which the core and shell provided photothermal and catalytic functionality, respectively.[218] Upon irradiation by a 1450 nm laser, the surface temperature of the hierarchical Cu_7S_4 hollow microsphere core increased to 94 °C due to the strong LSPR absorption. The rapid light-to-heat transformation caused the Cu_7S_4 core to function as a nanoheater to promote the cyclocondensation reaction catalyzed by the surrounding ZIF shell, which possesses dual acid–base catalytic sites for the promoted photothermal catalysis.

4.2.3. MOFs with covalent-organic frameworks (COFs). As a new porous organic polymer, COFs have shown potential in photo(thermal) catalysis due to their high surface area, excellent chemical stability, and adjustable CT properties.[219–224] Hybridizing MOFs with COFs can not only maintain the respective traits of individual components, including abundant active sites and large surface areas, but also improve the catalytic activity present in each.[225–227]

Currently, core–shell MOF@COF hybrid materials are commonly fabricated by grafting amino-functionalized MOFs with imine-based COFs.[228–233] As a representative, Lu *et al.* reported a facile seed growth approach, mainly utilizing the chemical Schiff base reaction between the aldehyde at the COF and amino groups on MOF, to coat MOF NH_2-MIL-125 with COF TAPB-PDA, affording NH_2-MIL-125@TAPB-PDA sample.[228] Interestingly, the thickness of the COF shell can be controlled simply by changing the concentration of COF monomers used. Photocatalytic experiments showed that this core–shell MOF@COF hybrid structure furnished the highest yield for oxidation of benzyl alcohol to benzaldehyde, in contrast to the pure MOF and COF. The superior photocatalytic activity was due to the accelerated transfer of e^- and h^+ between the MOF and COF with the presence of covalent bonds.

Another representative example for constructing a core–shell MOF@COF hybrid utilizing the above method was reported by Zhang *et al.*[229] In this work, NH_2-MIL-125, named Ti-MOF, which contains amino functional groups allowing further covalent bridging, was adopted as the MOF core, while TpTt-COF, which is functionalized with triazine and keto, was chosen as the shell. In the hybrid process, Ti-MOF-CHO possessing covalent connecting sites was first prepared by reacting Ti-MOF with 2,4,6-triformylphloroglucinol (Tp). Then, by changing the ratio of Ti-MOF-CHO and TpTt-COF precursors, an ultrathin nanobelt-like TpTt shell with more accessible active sites can be obtained. Due to the efficient photoinduced electron migration from the Ti-MOF core to the TpTt shell and the concentrated electrons on the decorated Pd NPs, the resulting Pd@Ti-MOF@TpTt catalyst showed significantly greater photocatalytic activity than that of the Ti-MOF, TpTt-COF, and Ti-MOF@TpTt hybrid for the cascade reactions of ammonia borane (AB) hydrolysis and nitroarene hydrogenation.

5. Organic transformations over MOF-based photocatalysis

Benefiting from the unique photophysical characteristics, for instance, effective charge separation and high charge carrier mobility, MOFs have been considered as promising photocatalysts for diverse types of organic transformations, such as oxidation, reduction, coupling, tandem, and synergistic redox reactions (Fig. 17). The representative organic transformation reactions using MOF-based photocatalysts are summarized in Table 1.

5.1. Oxidation reactions

To date, photocatalytic organic oxidations with different reaction types have been developed, including selective oxidation of aromatic alcohols, oxidation coupling of amines, selective sulfoxidation reactions, and C–H oxidation.[41,271,272] There is often more than one ROS evolved in a photocatalytic system, which results in different distributions of products. For example, during the oxidation of benzyl alcohol, the existence of ROS $^{\bullet}OH$ could lead to the overoxidation byproduct of benzyl acid, which can be suppressed by utilizing mild ROS, such as $O_2^{\bullet-}$ or $^1O_2$. Due to their unique excitation and CT/EnT mechanism, MOFs are often used as photocatalysts for various oxidation reactions.[28,273]

5.1.1. Selective oxidation of aromatic alcohols. The selective oxidation of aromatic alcohols is vital in the chemical industry since it is a basic route for accessing the corresponding aldehydes and ketones, which are versatile structural units for the preparation of fine chemicals.[274–277] The conventional noncatalytic methods for these reactions requiring either the usage of toxic and caustic heavy metal oxidants ($K_2Cr_2O_7$, $KMnO_4$, *etc.*) under harsh operating conditions, or precious metals/metal complexes as catalysts and O_2 as the main oxidant, which is cost and contaminate. To address this issue, the photocatalytic alcohol oxidation route, which is green and sustainable, has attracted much attention.[133,167,177,234–236,278–282]

Chromium-based MOFs (Cr-MOFs) are very attractive MOF species for various potential applications because of their high porosity and stability.[283–286] However, the reported Cr-MOFs are still limited because of their complicated synthesis. By the direct solvothermal reaction of the precursors porphyrin H_2TCPP and $Cr(NO_3)_3$ with the addition of trifluoroacetic acid and benzoic acid as modulators, a porphyrinic Cr-MOF, named Cr-PCN-600, was successfully prepared by Oudi *et al.*[234] Upon visible light irradiation, Cr-PCN-600 can generate rich ROS $O_2^{\bullet-}$ and $^1O_2$ *via* CT and EnT processes, respectively, contributing to its superior catalytic performance for selective oxidation of benzyl alcohol to benzaldehyde compared with that of MIL-101 (Cr), Cr_2O_3, and the corresponding H_2TCPP linker.

Coupling heterogeneous photocatalysis with photo-Fenton-like catalysis is an efficiently method for ROS generation under mild conditions.[287–292] By using *N*,*N*′-bis(4-pyridylmethyl)

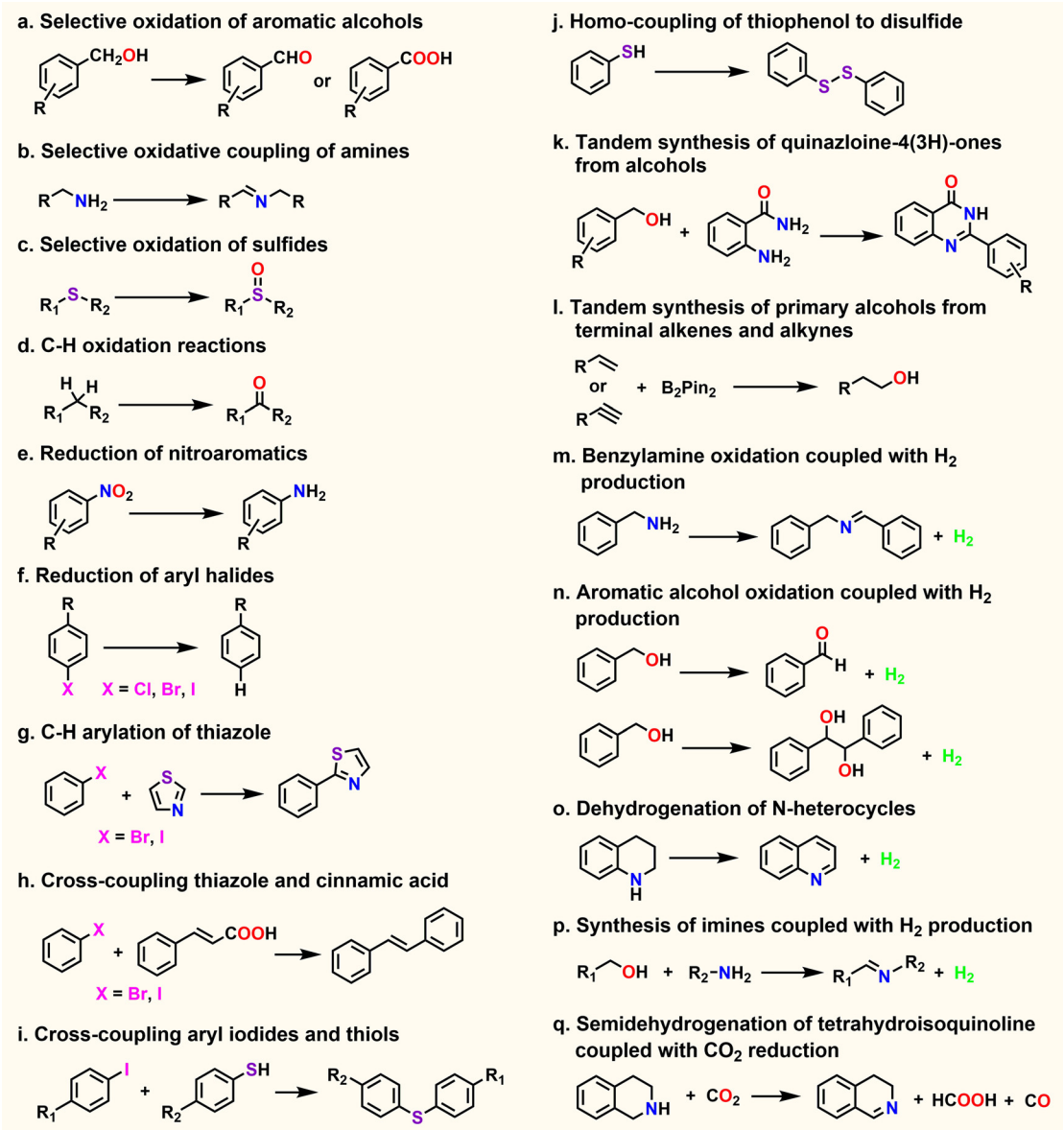

Fig. 17 Representative photocatalytic organic transformation reactions over MOF-based photocatalysts.

naphthalenediimide (DPNDI) as the photosensitizer, Cu(I) ions as the Fenton-like catalytic active sites, and the Dawson-type polyanion $[P_2W_{18}O_{62}]^{6-}$ as the oxidation catalyst, Si *et al.* prepared a novel MOF, named Cu(I)W-DPNDI (Fig. 18).[235] During the photocatalytic process, Cu(I) and $[P_2W_{18}O_{62}]^{6-}$ underwent continuous electron transfer to produce $^{\bullet}OH$ and $O_2^{\bullet-}$. Moreover, the reaction between $O_2^{\bullet-}$ and $^{\bullet}OH$ radicals, as well as the disproportionation reaction of $^{\bullet}OH$, can simultaneously produce abundant $^1O_2$, making Cu(I)W-DPNDI an excellent photocatalyst for the selective oxidation of benzyl alcohols to benzaldehyde.

In addition to the above selective oxidation of aromatic alcohols to aldehydes, the synthesis of carboxylic acids from aromatic alcohols by photocatalysis was also realized by using a binary system of NH_2-MIL-125(Ti)/NaBr.[236] In this photocatalytic process, photoexcited electrons can transfer from Br^- to Ti–O oxo-clusters within NH_2-MIL-125(Ti) to generate $Br_2^{\bullet-}$ instead of $Br^{\bullet}$ in one step. Subsequently, the Ti^{3+} generated by the reduction of the Ti–O oxo-clusters can interact with O_2 to produce ROS $O_2^{\bullet-}$, which can combine with the earlier formed $Br_2^{\bullet-}$ to facilitate the conversion of aromatic alcohols with various electron withdrawing or donating substituents into the corresponding carboxylic acids. Notably, when aliphatic primary alcohols are used as the substrates, satisfactory conversion and selectivity can also be obtained by using this photocatalytic system.

5.1.2. Selective oxidative coupling of amines. As an important procedure that popular in laboratories and industries, the selective oxidative coupling of amines to imines has received increasing attention because imines are crucial nitrogen (N)-containing reaction intermediates in agricultural, pharmaceutical, and synthetic chemistry.[293–296] However, the synthesis of imines *via* traditional coupling procedures suffers from low

Table 1 Summary of MOF-based photocatalysts for representative organic transformations

Catalyst	Reaction	E_g [eV]	Reaction conditions	Conversion[a] [%]	Ref
Cr-PCN-600	Oxidation of benzyl alcohol to benzaldehyde	1.71	1 mmol [S], 10 mg [P], CH_3CN, 32 °C, 40 h, visible LED (−)	98	234
Cu(I)W-DPNDI		2.22	0.5 mmol [S], 10 mg [P], H_2O + C_2H_5OH, r. t., 16 h, white LED (−)	75	235
NH_2-MIL-125(Ti)/NaBr	Oxidation of alcohols to carbonyl acids	2.41	0.2 mmol [S], 5 mg [P], $CH_3COOC_2H_5$, r. t., 12 h, light module (450 nm)	100	236
PCN-222	Oxidation of amines to imines	1.82	0.1 mmol [S], 5 mg [P], CH_3CN, r. t., 1 h, Xenon lamp (<420 nm)	100	237
Ti-PMOF-DMA		1.97	0.3 mmol [S], 5 mg [P], CH_3CN, r. t., 30 min, red LED [(623 ± 8 nm)]	94	238
JNU-207		1.90	2.0 equiv. [S], 1 mol% [P], CH_3CN, r. t., 24 h, blue LED (455 nm)	94	138
Bodipy@Co_{16}-MOF-BDC		2.81	0.5 mmol [S], 5 mg [P], CH_3CN + CH_2Cl_2, r. t., 3 h, Xenon lamp (>400 nm)	100	239
2D PMOF(Ti)		1.96	0.3 mmol [S], 5 mg [P], CH_3OH, r. t., 45 min, red LED (623 nm)	94	240
PCN-222/HOOC-TEMPO		1.80	0.3 mmol [S], 5 mg [P], CH_3OH, r. t., 20 min, red LED [(660 ± 8 nm)]	90	241
In_2S_3/NU-1000	Oxidation of sulfides to sulfoxides	—	0.3 mmol [S], 20 mg [P], CD_3OD, r. t., 3 h, visible LED (450–700 nm)	94	242
Zr-MOF		2.07	0.3 mmol [S], 5 mg [P], H_2O, r. t., 2 h, blue LED (425 nm)	100	243
Zn-AcTA		2.58	0.35 mmol [S], 5 mg [P], CH_3OH, r. t., 9 h, blue LED (427 nm)	96	244
Fe-UiO-66		3.02	47.2 μmol [S], 10 mg [P], CH_3CN, r. t., 3.5 h, Xenon lamp (≥380 nm)	97	155
Zn-TCPP(Mn)	Oxidation of C–H	1.94	0.5 mmol [S], 5 μmol [P], CH_3CN, 30 °C, 12 h, blue LED (420 nm)	95	245
Ce–AQ		—	1 mmol [S], 5 μmol [P], CH_3CN, r. t., 14 h, blue LED (395 nm)	54	246
Pd/MIL-101(Fe)	Oxidative amidation	2.58	0.2 mmol [S], 20 mg [P], THF, r. t., 24 h, blue LED (460 nm)	94	247
In-TPBD-20	Oxidative cyanation/cyclization	2.55	0.2 mmol [S], 5 μmol [P], CH_3CN, r. t., 12 h, blue LED (455 nm)	92/67	248
Ce-UiO(66)-BDC	Decarboxylative oxygenation	2.98	0.5 mmol [S], 7.5 μmol [P], toluene, r. t., 24 h, blue LED (420–460 nm)	86	249
TBUPP-Cu MOF	Oxidation of 5-hydroxymethylfurfural	1.84	12.5 μmol [S], 5 mg [P], CH_3CN, r. t., 24 h, blue LED (430 nm)	99	250
NU-1000	Iodo-/(*Z*)-selective-perfluoroalkylation of olefins	—	0.25 mmol [S], 6.25 μmol [P], CH_3CN, r. t., 12 h, visible LED (405 nm)	93/76	59
UiO-68-TDP	Synthesis of tetrahydroquinolines	—	0.2 mmol [S], 4 mg [P], CH_3CN, r. t., 12 h, blue LED (≤450 nm)	82	251
Cu@$UN_{300/6}$	Functionalization of terminal alkynes	—	0.08/0.13 mmol [S], 5 mg [P], CH_3CN, r. t., 12 h, Xenon lamp (−)	92/87	252
FL@Bim-UiO-66	Synthesis of imidazobenzothiadiazoles	2.23	0.1 mmol [S], 0.6 mol% [P], CH_3CN, r. t., 2 h, blue LED (400–470 nm)	92	171
Zn-MOF	Reduction of nitroarenes	2.20	0.1 mmol [S], 5 mg [P], C_2H_5OH, r. t., 4 h, Xenon lamp (≥420 nm)	99	253
Pd/Ti-MOF	Reductive *N*-formylation of nitroarenes	2.30	0.3 mmol [S], 30 mg [P], H_2O, r. t., 6 h, white LED (−)	98	254
Cd-SNDI	Activation of aryl halides	—	0.05 mmol [S], 5 mol% [P] dibutylamine, 40 °C, 4 h, blue LED (455 nm)	90	255
Pd/MIL-101(Fe)	Cinnamic acid decarboxylation cross-coupling	2.58	0.25 mmol [S], 20 mg [P] DMA, r. t., 24 h, blue LED (460 nm)	95	256
Zr_{12}–Ir–Ni	Cross-coupling of aryl iodides and thiols	—	0.5 mmol [S], 0.25 mg [P] CH_3CN, 55 °C, 48 h, blue LED (410 nm)	91	257
TMU-34(-2*H*)	Cross-coupling of sulfides to disulfides	2.15	2.5 mmol [S], 5 mmol% [P], CH_3CN, r. t., 1.5 h Hg lamp (−)	99	258
Pt_{2-2}@MOF	Buchwald–Hartwick reaction	2.81	0.25 mmol [S], 5 mg [P], H_2O + C_2H_5OH, r. t., 3 h, Xenon lamp (>440 nm)	80	259
PCN-224-SO_4	Tandem semisynthesis of artemisinin	—	0.106 mmol [S], 4 mg [P], CH_2Cl_2, 5–10 °C, 6 h, LED lamp (−)	98	260
Fe@PCN-222(Fe)	Tandem synthesis of quinazolin-4(3*H*)-ones	1.65	0.5 mmol [S], 30 mg [P], CH_3CN, 40 °C, 32 h, visible LED (−)	75	261
JNM-20	Tandem synthesis of primary alcohols	1.49	0.2 mmol [S], 5 mol% [P], CH_3CN, r. t., 12 h, white LED (−)	77	262
Pt/PCN-777	Amine oxidation coupled with H_2 production	—	50 μL [S], 10 mg [P], DMF, r. t., –, Xenon lamp (−)	—	263
NiCdS@MIL-101		—		99	264

Table 1 (*continued*)

Catalyst	Reaction	E_g [eV]	Reaction conditions	Conversion[a] [%]	Ref
			1 mmol [S], 5 mg [P], CH_3CN, r. t., 10 h, blue LED (470 nm)		
CdS@MIL-53(Fe)	Alcohol oxidation coupled with H_2 production	—	0.5 mmol [S], 5 mg [P], CH_3CN, r. t., –, Xenon lamp (> 420 nm)	—	265
UiO-66(Zr)		—	0.1 mmol [S], 10 mg [P], CH_3CN, r. t., 48 h, Xenon lamp (380–800 nm)	95	266
Porphyrin-MOFs	Dehydrogenation of N-heterocycles coupled with H_2 production	—	0.4 mmol [S], 7 mg [P], pyridine, r. t., 2 h Xenon lamp (> 390 nm)	—	267
Co-MIX		2.57	0.5 mmol [S], 2 mg [P], DMF, r. t., 20 h, blue LED (420 nm)	—	268
Ni/CdS/TiO_2@MIL-101	C–N formation coupled with H_2 production	—	0.1 mmol [S], 0.6 mg [P], CH_3CN, 27 °C, 24 h, blue LED (470 nm)	92	269
MOF-253-Ru(dcbpy)	THIQ oxidation coupled with CO_2 reduction	—	0.08 mmol [S], 10 mg [P], CH_3CN, r. t., 5 days, white LED (–)	92	270

[a] Conversion of one representative substrate is given; [S] = substrate; [P] = photocatalyst; r. t. = room temperature.

selectivity and poor substituent tolerance and cannot meet the requirements of the pharmaceutical and biotechnological industries.[297] Recently, the selective oxidative coupling of amines to imines by photocatalysis, which can overcome the above difficulties, has been considered a potential alternative strategy.[60,138,142,176,237–239,253,298–309]

Xu *et al.* studied the oxidative coupling of amines to imines reaction by adopting the porphyrinic MOF PCN-222 as the representative photocatalyst (Fig. 19a).[237] Due to the LCCT process within PCN-222, oxygen-centered active centers formed by photoexcited electron transfer from porphyrin linkers to Zr-oxo clusters can react with O_2 to produce $O_2^{\bullet-}$. Moreover, $^1O_2$ can also be provided by the EnT process through porphyrin linkers. As a result, PCN-222 showed superior photocatalytic performance for this reaction, benefiting from the combination of the LCCT and EnT processes.

In addition, by employing *N*,*N*′-dimethylacetamide (DMA) and *N*,*N*′-diethylformamide (DEF) as solvents, Sheng *et al.* reported the solvent-controlled preparation of two Ti-based porphyrinic MOFs, Ti-PMOF-DMA and Ti-PMOF-DEF.[238] The results showed that both DMA and DEF are coordinated to the Ti-oxo clusters of the two MOFs, but due to the lower electron density of DMA, electron migration from the H_2TCPP ligand to the Ti-oxo clusters in Ti-PMOF-DMA is easier. As a result, with the synergistic effect of h^+ and $O_2^{\bullet-}$ generated upon light irradiation, Ti-PMOF-DMA exhibited increased activity for the oxidative coupling of amines to the corresponding imines (Fig. 19b).

The Zn-based MOF JNU-204 was found to be an efficient photocatalyst for aerobic oxidation reactions by Jin *et al.* due to the presence of a D–A–D-type pyrazole-bridging ligand.[141] However, further investigation indicated that the Zn clusters within the MOF had little effect on the photocatalytic performance. Therefore, the researchers constructed JNU-207 by replacing the Zn clusters in JNU-204 with Co clusters, which optimized the electron-transfer efficiency.[138] The enhanced $O_2^{\bullet-}$ and $^1O_2$-generating capacities of JNU-207 were verified, accounting for the better photocatalytic activity of JNU-207 in the oxidative coupling of amines to imines and the oxidative coupling of tertiary anilines with maleimides (Fig. 19c).

5.1.3. Selective oxidation of sulfides. The selective oxidation of sulfides to prepare corresponding sulfoxides is a valuable chemical process because sulfoxides are important for synthesizing drug molecules, physiologically active molecules, and natural products.[310,311] Traditionally, various oxidants, such as O_2, peroxides, and transition metal salts, have been used to realize the selective oxidation of sulfides to sulfoxides, but harsh reaction conditions are required and also accompanied by poor activity/selectivity.[312] The photoinduced selective conversion of sulfides to sulfoxides is highly desirable because of its environmental friendliness and sustainability.[240–244,313–320]

In contrast to 3D MOFs, 2D MOFs have obvious advantages, such as more abundant active sites and promoted photoexcited carrier separation and transfer, are very promising for utilization in photocatalysis.[321–323] For instance, Sheng *et al.* prepared a 2D Ti-based porphyrin MOF [2D PMOF (Ti)] and evaluated its activity for photocatalytic aerobic oxidation of sulfides to sulfoxides upon irradiation by red light.[240] The results showed that 2D PMOF (Ti) provided better performance for this type of reaction than other reported photocatalysts and had good cycle stability.

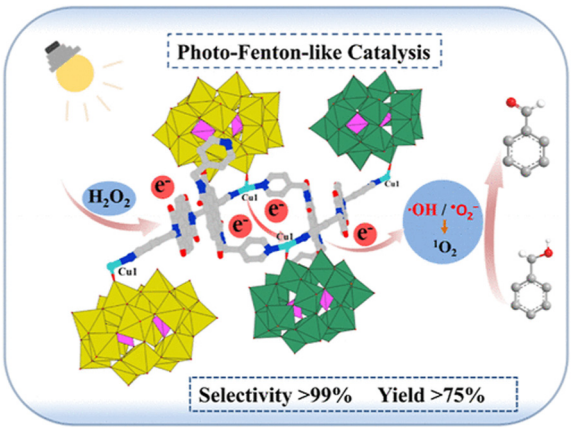

Fig. 18 Cu(I)W-DPNDI coupled photocatalysis with Fenton-like catalysis for selective oxidation of benzyl alcohol. Reproduced with permission from ref. 235. Copyright 2023 ACS.

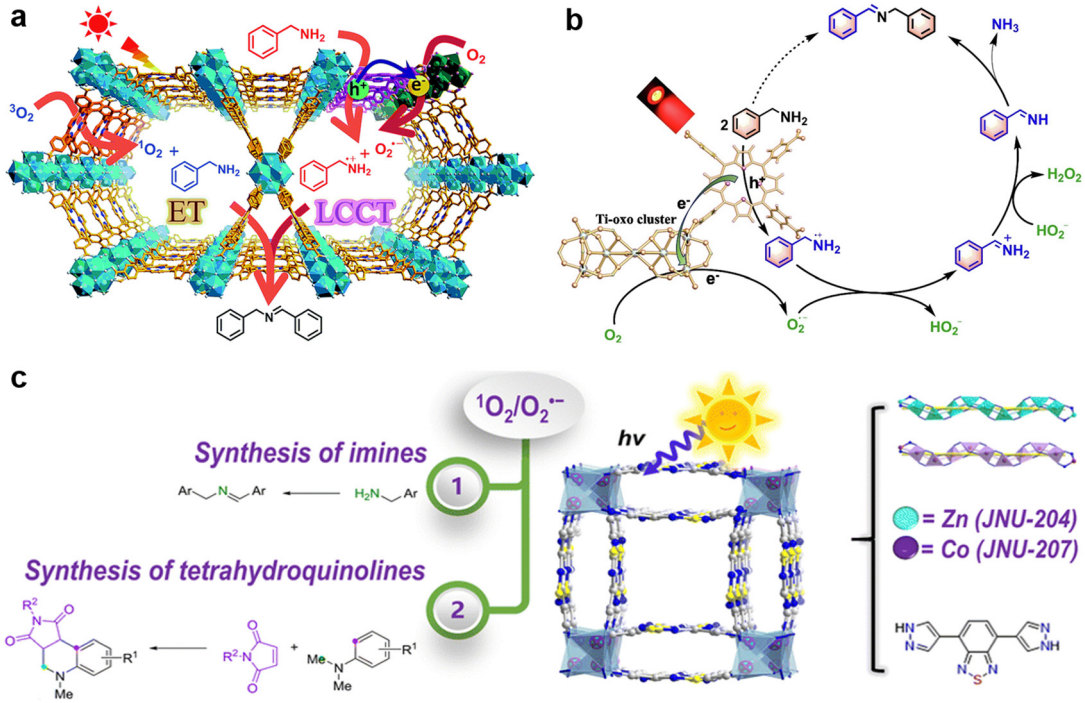

Fig. 19 (a) PCN-222 with combined LCCT and EnT processes for photocatalytic oxidative coupling of amines to imines. Adapted with permission from ref. 237. Copyright 2018 RSC. (b) A proposed mechanism for the selective oxidation of BA over Ti-PMOF-DMA. Adapted with permission from ref. 238. Copyright 2022 Elsevier. (c) Schematic illustration showing the oxidative coupling of amines and tertiary anilines over photocatalysts JNU-207 and JNU-204. Adapted with permission from ref. 138. Copyright 2022 Wiley.

A mechanistic study revealed that the reaction pathway was established in the CT process, which contributes to the generation of the primary ROS $O_2^{\bullet-}$ (Fig. 20).

Very recently, based on a novel designed photoactive perylenediimide carboxylic ligand, Chen *et al.* prepared a new Zr-MOF possessing an ultrahigh porosity composed of triangular micropores and hexagonal mesopores.[319] By irradiating crystalline sample of this Zr-MOF with encapsulated thioanisole under blue light, the successful transformation of methylphenyl sulfide to the oxidation product methylphenyl sulfoxide was fully proven. The photocatalytic oxidation activity of sulfides to sulfoxides was further demonstrated in aqueous solution by using different sulfides as substrates. As the proposed reaction mechanism for this system, the formed high-energy excited state [Zr-MOF]* upon light irradiation can directly transfer energy to O_2 to generate the ROS $^1O_2$ *via* intermolecular transfer. Meanwhile, it can first seize an e^- from the substrate sulfide to form the radical anion $[Zr\text{-}MOF]^{\bullet-}$, which then transfers one e^- to O_2 to yield another ROS $O_2^{\bullet-}$. These two possible pathways contribute to the superior photocatalytic performance.

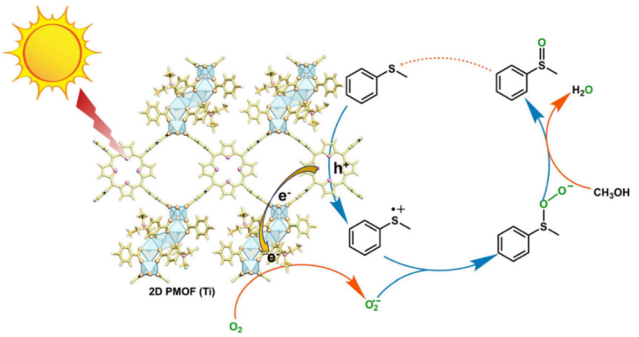

Fig. 20 The proposed photocatalytic mechanism of 2D PMOF (Ti) for the selective aerobic oxidation of sulfides. Reproduced with permission from ref. 240. Copyright 2022 Elsevier.

As a semiconductor with a broad visible-light response capacity, indium sulfide (In_2S_3), which possesses a suitable band gap (2.0–2.4 eV), has excellent photosensitivity and photoconductivity and sufficient reducing power for O_2 molecule activation.[324–327] Wang *et al.* fabricated a *Z*-scheme heterojunction photocatalyst, In_2S_3/NU-1000, wherein NU-1000 is a Zr-MOF with high porosity assembled by the octahedral Zr_6 cluster with a photoactive pyrene linker.[242] When used as a photocatalyst for the oxidation of sulfides to sulfoxides, the In_2S_3/NU-1000 composite displayed excellent performance mainly due to the formation of a *Z*-scheme heterojunction between In_2S_3 and NU-1000, which improved the CT for the effective generation of $O_2^{\bullet-}$ and $^1O_2$.

5.1.4. C–H oxidation reactions. Selective oxidation of inert C(sp^3)–H bonds to directly provide value-added fine chemicals is an essential procedure in organic synthesis.[328–334] Unfortunately, due to the high stability of C(sp^3)–H bonds, high temperature and/or high pressure for the generation of ROS as well as strong oxidants (H_2O_2, *tert*-butyl hydroperoxide,

etc.) are often necessary, which results in inevitable oxidant waste and serious consumption of the equipment. Therefore, replacing traditional thermocatalysis with photocatalysis to activate molecular oxygen, an inexpensive and environmentally friendly oxidant, *via* CT and/or ET processes under mild conditions is particularly desirable.[155,245,246,335–340]

A representative example of employing MOF-based photocatalyst for the selective oxidation of inert C–H bonds was proposed by Wang *et al.*, wherein a synergistic enzyme-like catalysis strategy was utilized.[245] Specifically, Zn-TCPP(Mn) with a Mn-porphyrin ligand [TCPP(Mn)] as the active site of O_2 and a 2,7-dipyridinyl fluoren-9-one (FL) ligand as the active site of the C–H bond was rationally synthesized by a one-pot solvothermal reaction. In the photocatalytic test system for C–H bond oxidation, *N*-hydroxyphthalimide, which can react with the FL ligand *via* proton-coupled electron transfer to generate the hydrogen atom transfer (HAT) agent phthalimide *N*-oxyl radical, was added. Benefiting from the synergistic photoactivation of O_2 by Zn-TCPP(Mn) and the formation of inert C(sp^3)–H bonds by the HAT agent, the selective and efficient oxidation of inert C–H bonds was achieved.

Recently, Ji *et al.* from the same group constructed a MOF (Ce–AQ) integrated binuclear Ce–O–Ce moieties with anthraquinone groups, which possesses excellent oxygen activation capacity for the selective oxidation of inert C–H bonds (Fig. 21a).[246] Upon light irradiation, the uniformly distributed Ce–O–Ce moieties consisting of Ce^{IV}–O clusters are excited by a ligand-to-metal charge-transfer (LMCT) process to produce oxygen bridge radicals, which are then converted to carbon radicals by abstracting a hydrogen atom from the inert C–H bonds through a regular HAT process. Meanwhile, the abundant $^1O_2$ generated from the activation of O_2 by the anthraquinone groups *via* an EnT process under another photon excitation can combine with the carbon radicals to form peroxy radicals, which then hydrolyze to furnish the selective oxidation products with carbonyl groups by interacting with the unsaturated coordinated Ce ions. During this process, the mixed-valence oxygen bridge is regenerated and can be utilized in the next catalytic cycle.

Han *et al.* synthesized a highly delocalized MOF Zn-TACPA with a 3-fold interpenetrated framework by using vinyl-functionalized triphenylamine and bipyridine as ligands toward ligand functionalization (Fig. 21b).[339] In addition to the optimized photoredox potential, a triphenylamine ligand functionalized with vinyl bonds can also improve the light-harvesting capacity of the MOF, allowing O_2 to be powerfully activated *via* a single-electron-transfer (SET) process upon irradiation. Furthermore, the optimized electron transfer of Zn-TACPA benefiting from the improved conjugation degree of the triphenylamine ligand in the framework provided by the introduced vinyl bonds can realize the rapid activation of O_2. As a result, O_2 was very efficiently activated by Zn-TACPA to generate $O_2^{\bullet-}$, which combines with the abundant Lewis acid sites of Zn^{2+} to increase the photooxidation activity of glycine esters and styrenes involving inert C(sp^3)–H bond oxidation compared with that of a structurally similar but vinyl-free triphenylamine-based MOF.

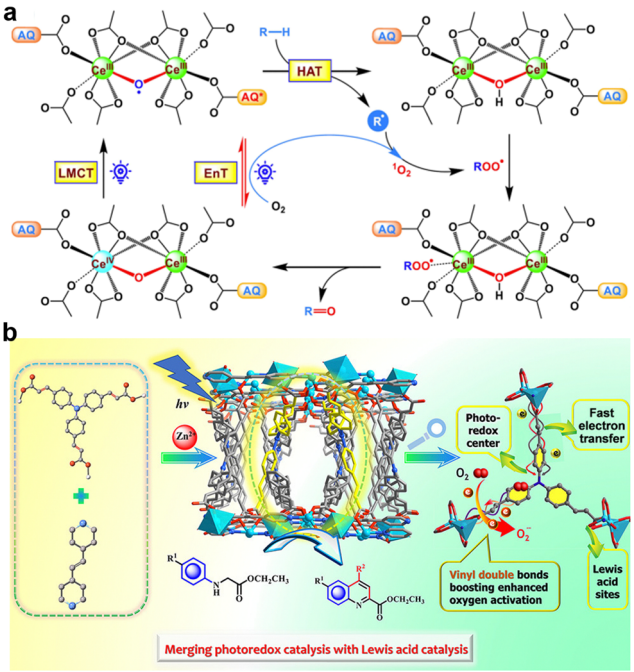

Fig. 21 (a) The Proposed reaction mechanism of Ce–AQ for the selective oxidation of inert C(sp^3)–H bonds. Adapted with permission from ref. 246. Copyright 2022 ACS. (b) Schematic illustration of the synthesis of Zn-TACPA and its use in the photooxidation of glycine esters and styrenes involving inert C(sp^3)–H bond oxidation. Adapted with permission from ref. 339. Copyright 2022 ACS.

5.1.5. Other oxidation reactions. In addition to the types of oxidation reactions described above, MOF-based photocatalysts have also been applied to other oxidation reactions.[28,250,273] For example, to challenge the green synthesis of amide bonds with visible light, Jiang *et al.* prepared three Fe-MOFs with distinct Fe–O clusters and Lewis acid sites, followed by the encapsulation of Pd NPs.[247] Benefiting from the easily photoexcited Fe_3-oxo clusters, abundant Lewis acid sites for improving the condensation reaction between aldehydes and amines, and electron-rich Pd NPs for reducing O_2 to $O_2^{\bullet-}$, Pd/MIL-101(Fe) displayed the highest photocatalytic performance for amide bond formation. Notably, by using only O_2 or air as the green oxidant, various aldehydes, alcohols and toluene can react with amines and be efficiently converted to the corresponding amide compounds in heterogeneous photocatalysis.

The construction of the tetrahydroquinoline (THQ) motif is highly important because it is an important skeleton of many natural products and pharmaceutical agents.[341] Li *et al.* integrated a photoactive thiadiazolopyridine (TDP) ligand into a stable UiO-68 isoreticular Zr-MOF *via* a simple one-pot synthetic strategy, and the resulting mixed-ligand MOF UiO-68-TDP was demonstrated to be an excellent photocatalyst for the synthesis of THQs through the oxidative cyclization of *N*,*N*-dimethylanilines and maleimides in an open air atmosphere.[251] As a possible photocatalytic mechanism, photoexcited UiO-68-TDP (PC*) can activate O_2 in air to produce $^1O_2$ and $O_2^{\bullet-}$ *via* EnT or SET processes, respectively. Simultaneously, PC* and $^1O_2$ can oxidize *N*,*N*-dimethylaniline through a SET process to produce the corresponding radical

cation, which is then deprotonated by $O_2^{\bullet-}$ to afford the α-aminoalkyl radical. Subsequently, a new radical is formed by the radical addition of maleimide to the α-aminoalkyl radical, accompanied by intramolecular cyclization to generate the crucial intermediate. Eventually, desired product is generated through the ROS-mediated electron and proton separation of the intermediate.

The oxidative cyanation and cyclization products of aryl tertiary amines are important intermediates in the synthesis of N-containing bioactive compounds.[342] By carefully modulating the stacking patterns of the photoactive A–π–D chromophore ligand, Hou *et al.* prepared 2-fold and 4-fold interpenetrated indium-based MOFs, noted as In-TPBD-20 and In-TPBD-50, respectively, and studied their interpenetration degree-dependent performances of light harvesting and O_2 activation.[248] The ROS assay experiments showed that, compared to In-TPBD-50, In-TPBD-20 possessed a greater capacity to generate $O_2^{\bullet-}$ while a weaker capacity to generate $^1O_2$. Theoretical calculations further verified that O_2 adsorbed on In-TPBD-50 is more likely to trigger the conversion of $O_2^{\bullet-}$ to $^1O_2$ through a spin–flip electron transfer process. As a result, In-TPBD-20, which has a high $O_2^{\bullet-}$ generation rate, was a robust photocatalyst for various oxidative cyanations and cyclizations.

The catalytic decarboxylative oxygenation of arylacetic acids to afford C–O bond-forming products, including aldehydes and ketones, is also a meaningful reaction in organic transformation and industrial chemistry.[343] Jin *et al.* developed a green synthetic method for UiO-66-type Ce(IV)-MOFs and studied their photocatalytic activities for the decarboxylative oxygenation of 4-fluorophenylacetic acid with oxygen as the oxidant.[249] The catalytic tests showed that Ce-UiO-66, with an appropriate LMCT energy and a high light response under excitation by blue LEDs (420–460 nm), exhibited the best performance and could be utilized to other arylacetic acids. A mechanistic study indicated that the coordination of the substrate arylacetic acid RCH_2COOH to the Ce(IV) nodes within Ce-UiO-66-BDC can be achieved by exchanging the hydroxyl groups on Ce(IV) nodes. The formed Ce(IV) cluster-$OCOCH_2R$ adduct and the subsequent photolysis of this adduct initiated by LMCT determine the subsequent organic transformation process.

The aerobic oxidative coupling of terminal alkynes is an important but challenging reaction in the field of organic synthesis.[341] Recently, Li *et al.* developed a hierarchical MOF-based single-site Cu catalyst that can serve as an efficient photocatalyst for this reaction.[252] Compared to the common thermolyzing approach that uses mixed-ligand MOF as a precursor, in this work, mesopores were introduced into UiO-66-NH_2 by adopting a simple approach of controlled partial linker thermolysis (Fig. 22a). The obtained hierarchical $UN_{300/6}$ (where 300/6 represents the temperature of 300 °C and time of 6 h) was demonstrated to have obvious mesopores with large apertures at 6–11 nm, where atomically dispersed Cu species can be located by coordinating the intact amino groups with divalent $Cu(II)^{2+}$ ions, followed by photoreduction at room temperature. Based on characterization and control experiments, a possible reaction mechanism of the obtained single-site Cu catalyst $Cu@UN_{300/6}$ for this reaction was also proposed. Upon light irradiation, the electron-deficient benzoquinone was reduced to generate a crucial radical anion, which can interact with the Cu-acetylide intermediate to provide the product (Fig. 22b). Notably, this photocatalyst was also demonstrated to show good activity for the hydroalkylation of terminal alkynes, and the corresponding reaction mechanism is shown in Fig. 22c. An electron first transfers from the photoexcited $Cu@UN_{306}$ to TBHP to produce a *tert*-butoxy radical (^{t}BuO$^\bullet$), which then works as a HAT agent to activate THF. The sequential interaction between the generated radical of THF and the Cu-acetylide intermediate can afford the hydroalkylation product.

5.2. Reduction reactions

Compared to photocatalytic oxidation reactions, photocatalytic reduction reactions, such as CO_2 reduction, N_2 reduction, and H_2 production, can provide more valuable chemicals from common materials.[344–355] To date, MOF-based photocatalysts have been widely applied in the photocatalytic oxidation based organic transformations and photoreduction reactions mentioned above; however, there are few reports on the use of MOF-based photocatalysts in photoreduction reactions of organic transformation.[253–255]

Recently, Chen *et al.* prepared a novel 3D Zn-MOF based on a photoactive organic linker and used it for the photoreduction of aromatic nitro compounds.[253] Upon direct interaction of the photoexcited Zn-MOF with nitrobenzene, no product was observed, possibly because no protons were present during the reaction. However, after the introduction of hydrazine hydrate ($N_2H_4{\cdot}H_2O$), which can reduce oxidative holes and produce the protons needed for the photoreduction reaction with clean N_2 as the only byproduct, aniline (AN) can be obtained. As a result, in the presence of $N_2H_4{\cdot}H_2O$, various nitroaromatics were selectively reduced to ANs with the use of the Zn-MOF photocatalyst.

The traditional synthesis of N-formylated products through the formylation of ANs is limited by the usage of toxic formylating sources and the generation of wastes.[356,357] Thus, it is necessary to develop sustainable approaches for synthesizing *N*-formylated compounds from nitroaromatics. Kar *et al.* constructed a photocatalyst, Pd-decorated Ti-MOF, which can be successfully applied in one-pot reductive *N*-formylation of nitroarenes with HCOOH as both the H_2 and formylating source.[254] A detailed mechanistic study indicated that the photogenerated charge carriers, which contributed to the generation of CO_2 and H_2 *via* the photodecomposition of HCOOH, accounted for the *N*-formylation. The resulting dissociative H_2 was adsorbed at the Pd active sites, reducing nitroarene to AN and converting it to *N*-formyl AN through the adsorbed HCOOH or CO_2 and H_2.

The activation of inert bonds, such as the reductive cleavage of aryl halide bonds through the SET pathway, is a cornerstone of synthetic chemistry.[358] Recently, Zeng *et al.* constructed a MOF, named Cd-SNDI, in which the NDI dye was decorated with S-bearing branches, and S···S-bridged nonaromatic NDI stacking was obtained (Fig. 23a and b).[255] The separation of the NDI cores by interdye aromatic stacking was inhibited by

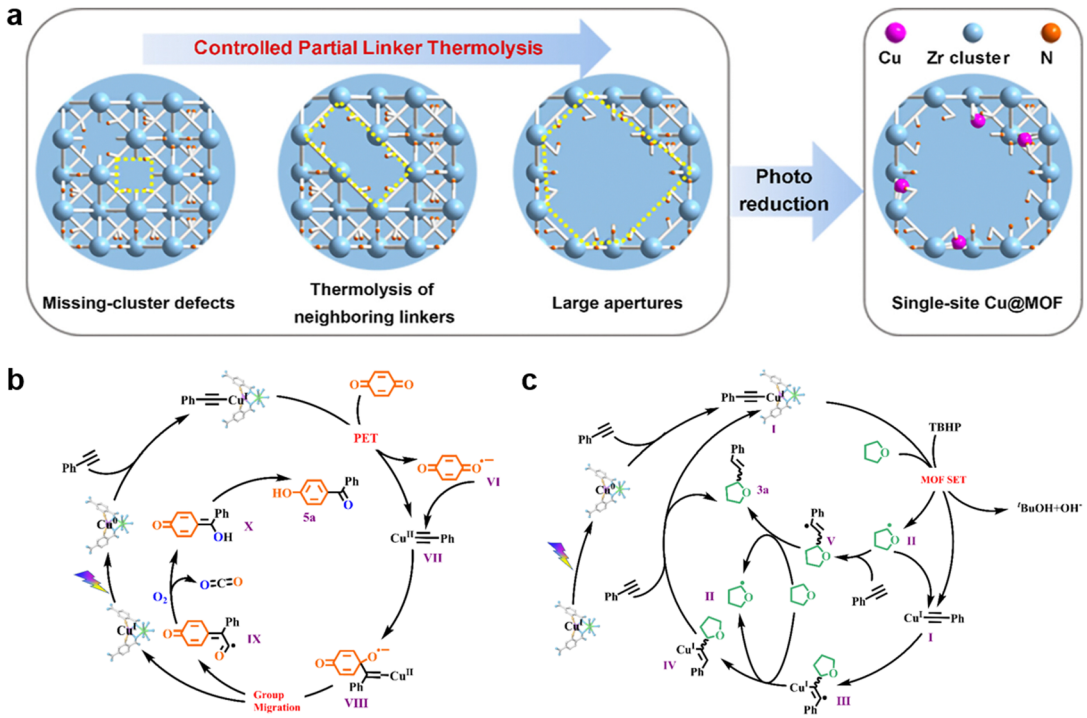

Fig. 22 (a) Schematic illustration showing the preparation of Cu@$UN_{300}/_6$. Proposed mechanisms of photocatalytic (b) aerobic oxidative coupling and (c) hydroalkylation of terminal alkynes over Cu@$UN_{300/6}$. Adapted with permission from ref. 252. Copyright 2023 Wiley.

coordination-oriented structural coercions, promoting the linking of neighboring NDI units *via* S-mediated noncovalent interactions (Fig. 23c). Benefiting from the interligand S···S contacts, which bridged the CT throughout the nonaromatic stacked NDI string in a long-range order way (Fig. 23d–f), the redox potential of a single excited-state NDI/$NDI^{\bullet-}$ unit can be maintained. Moreover, since S-branches with electron-donating ability are prone to connect with electron-deficient inert substrates, the probability of contact between the generated excited states and the substrates improved (Fig. 23g). As a result, high-efficiency photoreduction of aryl halides as well as the successive formation of C_{Ar}–C/S/P/B bonds based on Cd-NDI were realized.

5.3. Coupling reactions

Benefiting from their wide application in modern synthetic organic chemistry, catalyzed homo- and cross-coupling

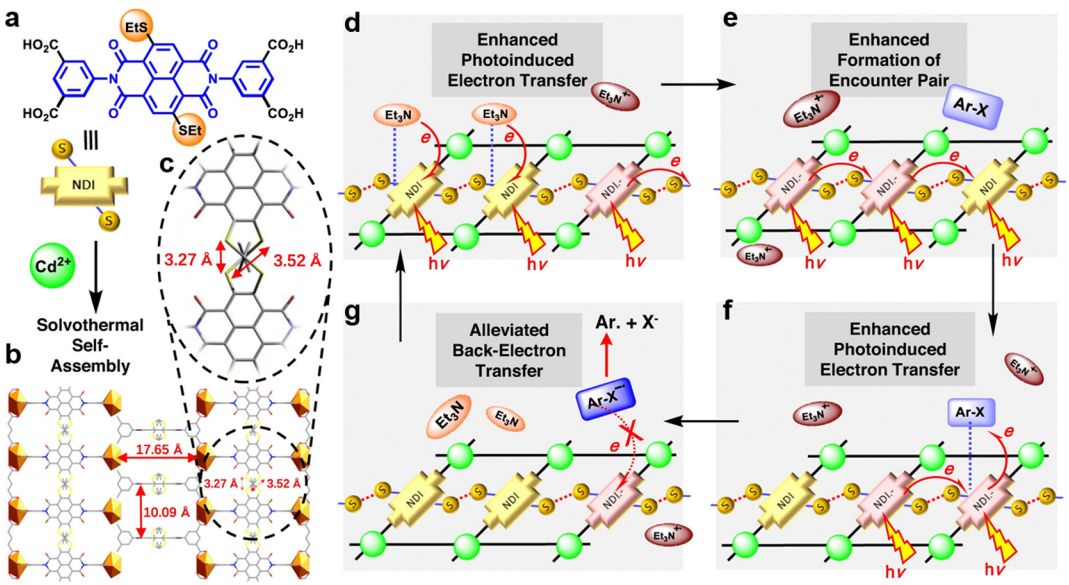

Fig. 23 (a) and (b) Structures of H_4SNDI and Cd-SNDI with the nonaromatic assembly of NDI units. (c) The S···S contact between adjacent NDI units. (d)–(g) Schematic illustration showing the one catalytic cycle in Cd-SNDI. Reproduced with permission from ref. 255. Copyright 2023 Nature.

reactions have received much attention since the realization of the Grignard reagent-assisted Ni-catalyzed coupling of aryl and alkenyl halides in 1972.[359] In contrast to the traditional thermal catalytic systems used for coupling reactions that require high temperature, photocatalytic coupling reactions under mild conditions have attracted increasing research attention.[156,256,258,259,360–366] Nevertheless, because it is difficult to understand and design suitable catalytic systems, the development of coupling reactions by photocatalysis is still in its infancy.

The C–H arylation reaction and decarboxylation cross-coupling reaction are two art methods for C–C bond formation.[367,368] Cheng *et al.* modulated the microenvironment of Pd NPs by using Fe-MOFs with different framework structures.[256] The photocatalytic tests of thiazole C–H arylation and cinnamic acid decarboxylation cross-coupling were conducted. Results showed that the Pd/MIL-101(Fe) photocatalyst possessed the highest activity for both types of reactions due to its most effective electron migration from Fe–O clusters to Pd NPs. It was proposed that the C–H arylation was realized following a three-step procedure, namely, (i) activation of the C–halogen bond by Pd NPs, (ii) aryl radical generation, and (iii) subsequent radical addition. However, the decarboxylation cross-coupling was carried out mainly follows the procedure (i), during which the selectivity of the products depended on the base additives.

The development of efficient and green approaches for C–S bond formation has attracted increasing interest due to the universality of C–S bonds in the fields of chemistry and medicine.[369,370] Zhu *et al.* utilized a robust and porous Zr_{12} MOF, named Zr_{12}–Ir–Ni, combined an Ir(III) photoredox catalyst with a Ni(II) cross-coupling catalyst for the formation of C–S bonds between aryl iodides and thiols (Fig. 24).[257] Benefiting from well-isolated Ni catalysts, the space confinement of Ir catalysts, as well as the close proximity (*ca.* 0.6 nm) between them, the transfer of electrons and thiophenol radicals from Ir to Ni(II) centers accelerated the catalytic cycle, and Zr_{12}–Ir–Ni exhibited a turnover number of up to 38 500.

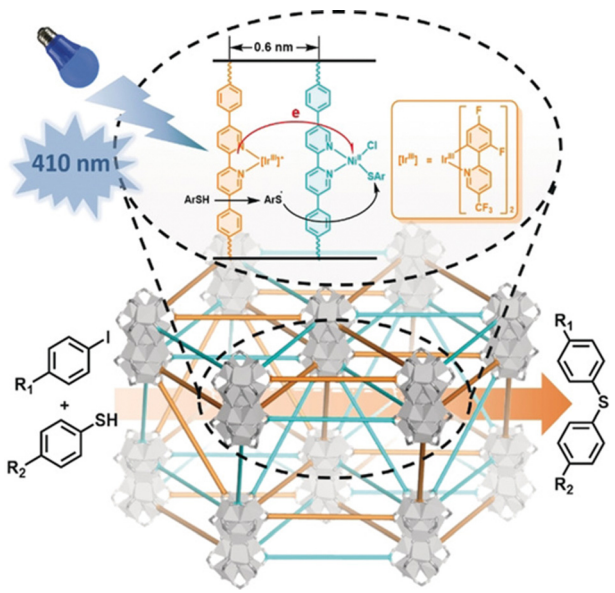

Fig. 24 Zr_{12} MOF merged with the photoredox Ir catalyst and the cross-coupling Ni catalyst for efficient C–S bond formation. Reproduced with permission from ref. 257. Copyright 2018 Wiley.

The coupling reactions that form disulfide bonds (–S–S–) are at the center of attention in synthetic organic chemistry due to their critical role in the biochemistry of life and unique application in the industry of –S–S– bonds.[371] Razavi *et al.* constructed a mixed-ligand Zn-MOF, TMU-34(-2*H*), using 4,4′-oxybis(benzoic acid) (H_2OBA) as the carboxylic linker and tetrazine-functionalized 3,6-di(pyridin-4-yl)-1,2,4,5-tetrazine (DPT) as the pillar.[258] Upon visible-light irradiation, the excited neutral tetrazine sites within the DPT pillars with photogenerated redox activity accept one electron from the reactants to generate tetrazine radical anions as electron mediator sites, which can then be transferred to other substrates in the reaction system to complete the synthesis of disulfides in an efficient way.

5.4. Tandem reactions

In contrast to traditional one-catalyst/one-reaction systems, tandem reactions are highly desirable for further catalysis because they can realize one-pot multiple organic transformations without separation or purification of the intermediates.[372–376] Despite their enormous advantages in terms of atom and step economy, tandem reactions are still in their infancy because of the great challenge in designing and synthesizing efficient catalysts with multifunctional active sites that can work synergistically to conduct multiple organic transformations in one pot. As one class of excellent solid supports, MOFs can be hierarchically immobilized with different catalysts in an ordered fashion to overcome the above challenge and are promising heterogeneous photocatalysts for tandem reactions.[260–262,377–383]

Artemisinin is currently the most efficient drug for treating malaria, however, its traditional synthetic approaches are still accompanied by complicated reaction and treatment steps as well as high cost.[384] Feng *et al.* prepared a series of porphyrinic MOF-based tandem photocatalysts, PCN-22*X*-SO_4 (X = 2, 3, 4), through postsynthetic treatment of acid-stable PCN-22*X* with dilute sulfuric acid.[260] A stability screening experiment supported that PCN-222-SO_4 is a potentially excellent photocatalyst for the tandem synthesis of artemisinin. As expected, under the conditions of visible light and O_2, PCN-222-SO_4 exhibited the best efficiency for the synthesis of artemisinin among reported photocatalysts, although with a selectivity between 50–60% resulting from byproducts that were unavoidably formed during the $^1O_2$ ene step. The excellent performance of this tandem photocatalytic process was benefited from the synergistic effect of the photosensitivity and abundant acid sites of PCN-222-SO_4.

The synthesis of quinazolinones has attracted much attention because their derivatives commonly have outstanding pharmacological and biological properties, such as antibacterial, anti-inflammatory and anticancer activities.[385] Ghaleno *et al.* developed a simple one-step strategy to decorate the nodes of PCN-222(Fe) with Fe(III), wherein the metal precursor Fe(III) chloride can remove the benzoic acids through the *in situ* generated HCl

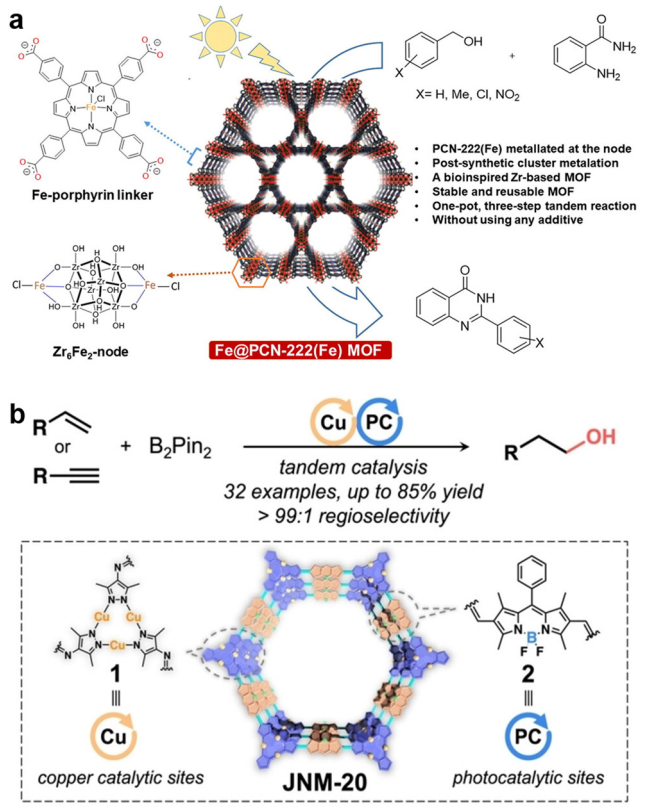

Fig. 25 (a) Schematic illustration of tandem synthesis of quinazloine-4(3*H*)-ones over Fe@PCN-222(Fe). Adapted with permission from ref. 261. Copyright 2019 Elsevier. (b) Schematic illustration of JNM-20 with integrated metal and photocatalytic systems for tandem synthesis of primary alcohols. Adapted with permission from ref. 262. Copyright 2023 Wiley.

and metalation of the Zr_6-nodes.[261] The resulting bioinspired MOF, Fe@PCN-222(Fe), was successfully applied as a photocatalyst to prepare quinazolin-4(3*H*)-ones *via* a one-pot three-step tandem reaction process (oxidation-cyclization-oxidation) from alcohols and 2-amonibenzamide (Fig. 25a). The excellent performance was contributed from the bifunctional characteristic of Fe@PCN-222(Fe), which can function as a photoredox as well as Lewis acid catalyst.

The development of efficient catalysts for synthesizing primary alcohols with terminal alkenes and alkynes as hydrocarbon feedstocks is particularly urgent due to their intensive application in chemical and pharmaceutical industries.[386,387] *Via* the Schiff-base condensation reaction between Cu(I) unit (Cu-CTU) and boron dipyrro–methene (Bodipy) ligand, Lin *et al.* have prepared a new 2D MOF, denoted as JNM-20 (Fig. 25b).[262] Benefiting from the good light-harvesting capacity of Bodipy and the large π-conjugated structure, JNM-20 possesses high charge separation efficiency. JNM-20 can catalyze the one-pot tandem synthesis of primary alcohols from terminal alkenes and alkynes with remarkable regioselectivity, high yields, and broad substrate compatibility. The detailed mechanism study indicated that the outstanding performance was derived from the synergistic effect of the Cu-catalyzed hydroboration and the photocatalyzed aerobic oxidation, which were provided by Cu-CTU and Bodipy ligands, respectively.

5.5. Synergistic redox reactions

Photocatalytic organic transformations to prepare useful molecules can provide a potential alternative for the synthesis of industrially relevant chemicals. However, to increase the reaction efficiency, in some cases, sacrificial reagents, including electron acceptors or donors, are added to photocatalytic organic reaction systems.[388] Such additives increase the consumption of e^- or h^+, limiting the practical application of photocatalytic organic transformation systems. Recently, the construction of dual-function photocatalytic systems, which can simultaneously utilize photogenerated h^+ and e^- to realize the selective oxidation and reduction of value-added products, has been considered as an ingenious strategy to overcome this obstacle.[389–394] Herein, we introduce several representative MOF-based bifunctional photocatalysis systems for coupling selective organic transformations with H_2 production or CO_2 reduction.

5.5.1. Benzylamine oxidation coupled with hydrogen production. The first example of a synergistic redox reaction over MOF-based photocatalysts was reported by Liu *et al.*, wherein a representative MOF, PCN-777, was adopted to realize BA oxidation coupled with H_2 production in the presence of a Pt cocatalyst (Fig. 26a).[263] From both the experimental and calculation results, PCN-777, which has a large π-conjugated ligand,

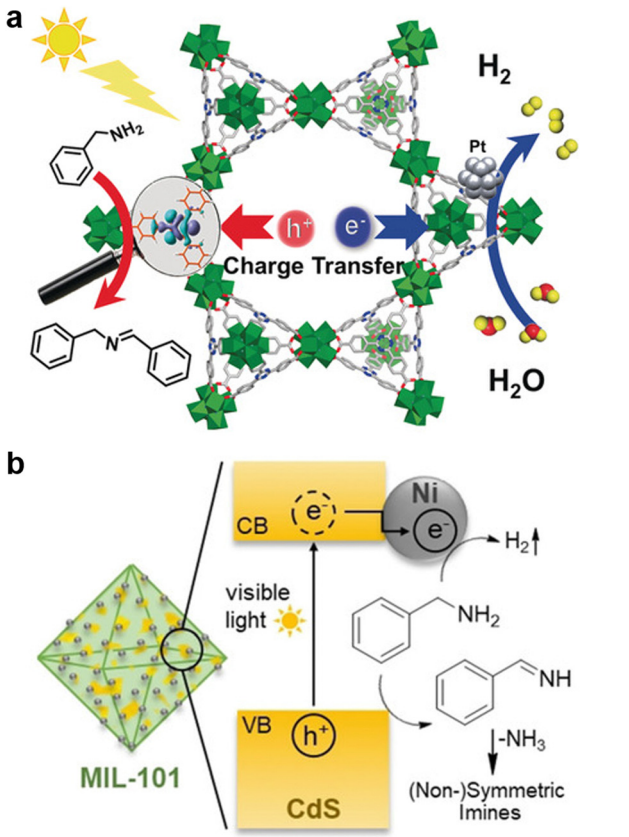

Fig. 26 (a) Schematic illustration showing the BA oxidation coupled with H_2 production over the photocatalyst Pt/PCN-777. Adapted with permission from ref. 263. Copyright 2018 Wiley. (b) Schematic illustration of BA dehydrogenation under liberation of H_2 over Ni/CdS@MIL-101. Adapted with permission from ref. 264. Copyright 2020 Wiley.

exhibited a much greater separation efficiency for photogenerated carriers than did MOF-808, which has a similar topology and the same coordination environment of Zr-oxo clusters but has a short ligand. As a result, without the addition of a sacrificial agent, the Pt/PCN-777 composite photocatalyst can efficiently convert BA to *N*-benzylbenzaldimine (*N*-BBA) at a rate of 0.49 mmol g^{-1} h^{-1} with > 99% selectivity, and a simultaneous H_2 evolution rate of 0.33 mmol g^{-1} h^{-1} can be achieved. It can be inferred that during the synergistic redox process, the photogenerated e^- reduce protons to H_2, while the h^+ oxidize BA to carbocationic species ($PhCH_2NH_2^{\bullet+}$), which is an important intermediate for the generation of *N*-BBA.

Klarner *et al.* reported another example of BA oxidation coupled with H_2 production.[264] The novel noble metal-free MOF-based photocatalyst system Ni/CdS@MIL-101 was prepared by decorating CdS NPs onto the outface of single MIL-101(Cr) crystallites and infiltrating bis(cyclopentadienyl)-Ni(II) into the pore, which was followed by reduction to Ni_0. The photocatalytic activity test showed that Ni/CdS@MIL-101 can efficiently oxidize BA with the simultaneous production of one equivalent of H_2. Furthermore, asymmetric imines can also be synthesized when using another amine that cannot be dehydrogenated by the photocatalyst under identical conditions. The excellent synergistic redox performance is attributed to the electrons around the Ni NPs involving in the reduction reaction for H_2 production, while the hole residue in the VB participates in BA oxidation (Fig. 26b). Notably, this is also the first example of photocatalytic acceptorless amine dehydrogenation.

5.5.2. Aromatic alcohol oxidation coupled with hydrogen production. Li *et al.* constructed a dual-function photocatalyst, CdS/MIL-53(Fe), for photocatalytic selective oxidation of benzyl alcohol coupled with H_2 production without the use of sacrificial agents.[265] Upon light irradiation, a *Z*-scheme electron transfer process between CdS and MIL-53(Fe) was believed to occur in the photocatalytic system. Specifically, e^- in the LUMO of MIL-53(Fe) and h^+ in the HOMO of CdS easily recombine, leading to the accumulation of e^- in the LUMO of CdS to reduce H^+ to generate H_2, while h^+ accumulate in the HOMO of MIL-53(Fe) to oxidize benzyl alcohol to form benzaldehyde. The evolution rate of H_2 (2.33 mmol g^{-1} h^{-1}) and the yield of benzaldehyde (2.83 mmol g^{-1} h^{-1}) are both much greater than those of CdS or MOF alone, demonstrating that a synergistic redox cycle occurred by the combination of CdS and MOF.

Due to the confusion of the radical species involved, it is still challenging to develop light-induced photocatalysts for the controllable preparation of vicinal diols through the dehydrogenation of alcohols.[395,396] Recently, Hao *et al.* realized the visible light-induced acceptorless dehydrogenation of alcohols to vicinal diols coupled with H_2 production over the well-known UV-responsive UiO-66(Zr), benefiting from a LMCT process between absorbed alcohols and coordination unsaturated $Zr(IV)^{4+}$.[266] The high selectivity of this system for vicinal diols was attributed to the formation of hydrogen bonds between alcohols and μ_3-OH in UiO-66(Zr), which inhibits the deprotonation of O–H bond and promotes the formation of C–C coupling products (Fig. 27). Notably, the oxidation products

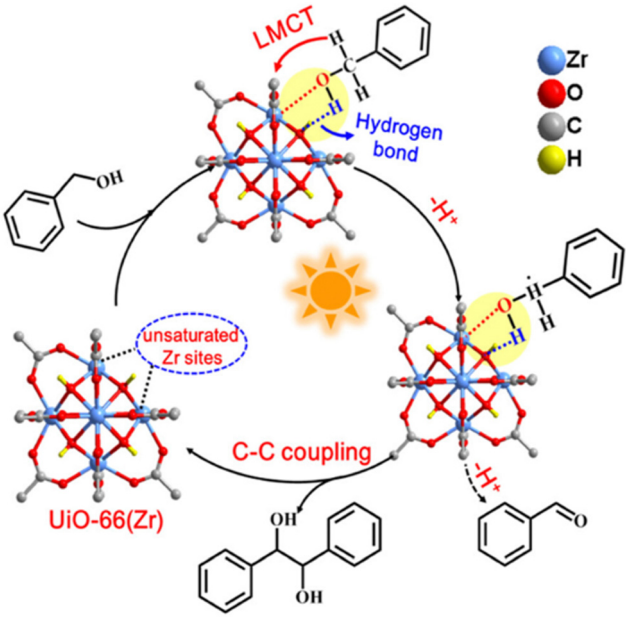

Fig. 27 Proposed mechanism for the light-induced acceptorless dehydrogenation of alcohols to vicinal diols coupled with H_2 production over UiO-66(Zr). Adapted with permission from ref. 266. Copyright 2022 ACS.

in the synergistic redox process can be converted to aldehydes after the deposition of Pt NPs onto UiO-66(Zr).

5.5.3. Dehydrogenation of N-heterocycles coupled with hydrogen production. The dehydrogenation of N-heterocycles is a vital organic transformation reaction in the pharmaceutical industry that is commonly conducted under thermal conditions and has been demonstrated to be light-initiated under ambient conditions by using MOF-based photocatalysts.[267,268,397–399] For instance, Gong *et al.* studied the photocatalytic activities of a series of porphyrin-based MOFs for the dehydrogenation of N-heterocycles with H_2 production.[267] These MOFs are constructed by using the same porphyrin ligand, *i.e.*, H_2TCPP, in which the distances between H_2TCPP active sites are different. There was a linear correlation between the catalytic activity and the reciprocal of the interaction site distance. PCN-223, which has the shortest interaction site distance, exhibited the best performance in the acceptorless dehydrogenation of THQ. Furthermore, the volumetric density of the active site was shown to have an irregular effect on the catalytic activity. It was found that the interactive site distance is a significant factor in determining the photocatalytic activity for the dehydrogenation of N-heterocycles.

Recently, by adopting a multicomponent strategy, Li *et al.* synthesized a mixed-ligand MOF, Co-MIX, in which two photoactive ligands were incorporated.[268] Because redox-active Co metal sites can facilitate the photoreduction of protons to H_2 and photogenerated h^+ can promote the oxidation of substrates, Co-MIX exhibited excellent photocatalytic performance for the semidehydrogenation of 1,2,3,4-tetrahydroisoquinoline (THIQ) coupled with H_2 production. Upon light irradiation, the oxidation product 3,4-dihydroisoquinoline was obtained at a rate of 1.50 mmol g^{-1} h^{-1}, while the H_2 production rate was

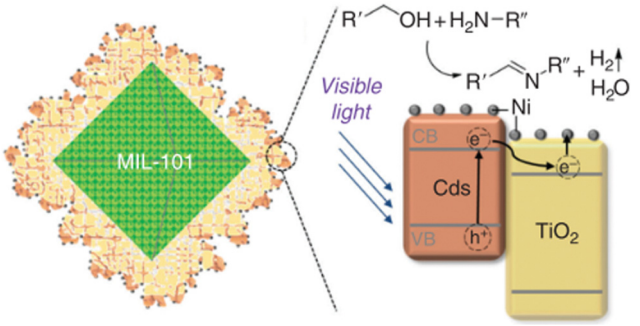

Fig. 28 Schematic illustration of the Ni/CdS/TiO_2@MIL-101 photocatalyst for the synthesis of imines from alcohols and amines coupled with H_2 production. Reproduced with permission from ref. 269. Copyright 2019 CSIRO.

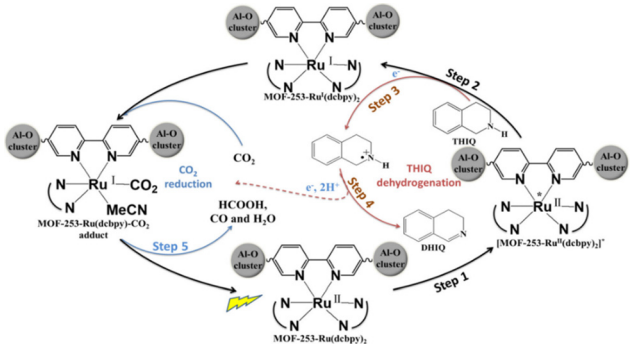

Fig. 29 Proposed photocatalytic mechanism for the selective semi-dehydrogenation of THIQ coupled with CO_2 reduction over MOF-253-Ru(dcbpy). Reproduced with permission from ref. 270. Copyright 2019 ACS.

1.25 mmol g^{-1} h^{-1}. Control photocatalytic tests supported that the multicomponent strategy is a promising way to optimize the photoactivity of MOFs. Notably, this MOF photocatalyst can also be applied to the selective oxidation of BA coupled with H_2 production.

5.5.4. Other synergistic redox reactions. The synthesis of imines from alcohols and amines has attracted broad interest for the formation of multiple C–N bonds.[400–403] Tilgner *et al.* decorated a Cd/TiO_2 heterojunction supported on MOF MIL-101(Cr) with cocatalytic Ni NPs, and the resulting noble metal-free photocatalyst Ni/CdS/TiO_2@MIL-101 with a core–shell morphology was demonstrated to show outstanding photocatalytic performance for the synthesis of imines from alcohols and amines coupled with H_2 production without the addition of sacrificial electron donors (Fig. 28).[269] Photoexcited electron transfer from the CB of CdS to that of TiO_2 in the CdS/TiO_2 heterojunction occurred. The charge separation efficiency can be further enhanced by the Ni NPs due to the electrical potential gradient at the Ni/semiconductor interface. As a result, the synergistic redox reaction was initiated by spatially separated e^- and h^+, and the Ni NPs acted as electron reservoirs, which contribute to quantitative H_2 production from alcohols (alcohol splitting).

Coupling photocatalytic selective organic transformations with CO_2 valorization into one reaction, which can synergistic allutilize photoexcited e^- and h^+, is particularly desirable because it can meet the goal of sustainable economic and social development.[392] Deng *et al.* prepared MOF-253-Ru(dcbpy) by coordinating Ru to the open *N*,*N*′-chelating sites of MOF-253. MOF-253-Ru(dcbpy) was utilized as a catalyst for photocatalytic semidehydrogenation of THIQ coupled with CO_2 reduction.[270] With regard to the synergistic redox mechanism (Fig. 29), MOF-253-Ru^{II}(dcbpy) is first photoexcited to produce [MOF-253-Ru^{II}(dcbpy)]* (step 1), which is then reduced to [MOF-253-Ru^{I}(dcbpy)]* by the substrate THIQ with the simultaneous production of a THQ radical cation (steps 2 and 3). This radical cation can be converted to the semidehydrogenated product of THIQ by releasing another electron and two protons (step 4). Eventually, CO_2 is reduced to formic acid and CO, and the photocatalyst is regenerated *via* a proton-coupled mechanism (step 5).

6. Organic transformations over MOF-based photothermal catalysis

Upon light irradiation, in addition to e^-- or h^+-engaged surface redox reactions, thermal energy (heat) can also be generated to promote endothermic reactions in the presence of components with photothermal effect in photocatalysts. Currently, photothermal catalysis over MOF-based materials is in its infancy yet highly desirable for efficient solar energy conversion. For instance, benefiting from the large pore structures of MOFs allowing the deposition of NPs with photothermal effect and the excellent absorption capacity of MOFs for CO_2 gas, MOF-based materials exhibit great potential in the photothermal catalysis of CO_2 hydrogenation,[404] which is a typical challenging reaction that requires high activation energy.[405]

The representative organic transformations over MOF-based photothermal catalysis are summarized in Fig. 30 and Table 2, mainly toward the different reaction types of oxidation, reduction, and CO_2 addition reactions. Given that the MOF itself and the NPs incorporated in MOF/NP composite photocatalysts can both display photothermal effect, the distinct reaction mechanisms of photothermal-mediated organic transformations will be strongly elucidated in this section.

6.1. Oxidation reactions

The photothermal effect of the MOF itself is usually attributed to the organic antenna within the framework, which can absorb long wavelength light. Typically, porphyrinic MOFs, with porphyrin ligands as effective photosensitizers, have been considered as potential photothermal catalysts due to their strong light-harvesting capacity in the visible light range. Chen *et al.* reported the photothermal effect of a porphyrinic MOF, PCN-224(M) (M represents the central metal ion of the porphyrin ligand), and fabricated Pt/PCN-224(M) composite catalysts with the synergistic photothermal effects of Pt and MOF, by simple addition of presynthesized PCN-224(M) to a preparation system of Pt NCs (Fig. 31a and b).[406] The synergistic photothermal conversion was fully demonstrated by the obvious differences in the aromatic alcohol oxidation yields when the reaction was carried out at 16 °C to eliminate the photoinduced heat, with heating instead of light

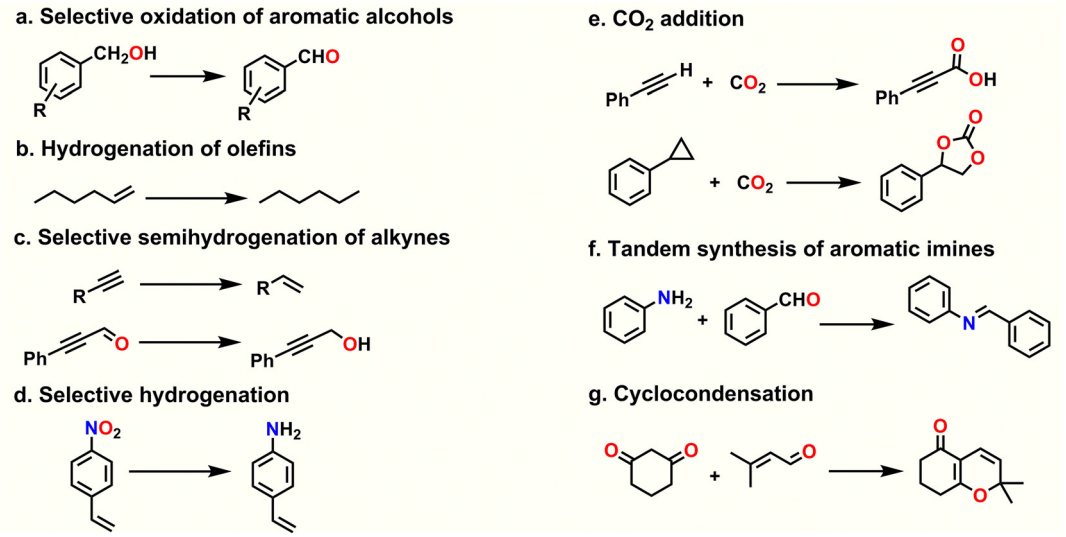

Fig. 30 Representative organic transformation reactions by photothermal catalysis over MOF-based materials.

irradiation, or without external disturbance (Fig. 31c). Furthermore, by simple changing the irradiation light intensity, the electron state of Pt can be regulated through competitive e^- transfer between Pt and PCN-224(Zn), influencing the eventual catalytic activity (Fig. 31d).

Advanced oxidation processes for the decomposition of wastewater pollutants, including antibiotics, pathogenic organisms, and pesticides, are highly desirable for freshwater production.[411] As a typical antibiotic pollutant, the decomposition process of tetracycline (TC), which involves series of organic transformation reactions, requires an effective catalyst.[412] Very recently, Bai *et al.* constructed a dual-functional Co-MOF/carbon nanotube (CNT) photocatalyst, in which the ligand H_2BDC used for MOF synthesis was prepared from the catalytic degradation of waste poly(ethylene terephthalate).[413] Benefiting from the synergistic effect of the localized solar heat derived from the outstanding photothermal effect of CNTs and the abundant open Lewis acid sites of Co-MOF in the composite photocatalyst, peroxymonosulfate can be efficiently activated to generate various ROS, including $SO_4^{\bullet-}$, $^{\bullet}OH$, $O_2^{\bullet-}$ and $^1O_2$, contributing to the superb degradation performance of TC. This work provides a sustainable platform for developing MOF-based materials that combine photothermal and photocatalytic methods with advanced oxidation processes for wastewater purification.

6.2. Reduction reactions

The development of catalytic hydrogenation reduction reactions that can avoid the use of heat, high-pressure H_2, and hydride reagents to replace traditional ones is highly desirable.[414] High-efficiency conversion of sunlight to heat *via* the surface plasmonic properties of metal NPs for hydrogenation reactions is a promising alternative.[415]

Selective semihydrogenation of alkynes to alkenes has received particular attention in both scientific and industrial fields but remains a major challenge.[416] Li *et al.* constructed a core–shell composite of CuPd@ZIF-8, wherein cubic Cu supported Pd were used as the core and porous ZIF-8 was used as the shell.[407] Upon light irradiation, the CuPd@ZIF-8 composite

Table 2 Summary of representative MOF-based photothermal catalysts for organic transformations

Catalyst	Reaction	E_g [eV]	Reaction conditions	Conversion[a] [%]	Ref
Pt/PCN-224(Zn)	Oxidation of benzyl alcohols to benzaldehydes	1.83	20 μmol [S], 20 mg [P], H_2O, 50 min, Xenon lamp (>400 nm)	>99	406
Pd NCs@ZIF-8	Hydrogenation of olefins	—	2 mmol [S], 5 mg [P], $CH_3COOC_2H_5$, 1.5 h, Xenon lamp (–)	100	98
CuPd@ZIF-8	Selective hydrogenation of alkynes	—	0.1 mmol [S], 1 mg [P], CH_3OH, 5 min, Xenon lamp (>400 nm)	97	407
PdAg@ZIF-8	Selective hydrogenation of nitrostyrene	—	0.1 mmol [S], 5.5 mg [P], C_2H_5OH, 20 min, Xenon lamp (>400 nm)	100	408
PMo_{12}@Zr–Fc	CO_2 cycloaddition	5.38	12.5 mmol [S], 5 mg [P], solvent-free, 8 h, Xenon lamp (–)	87	175
FeTPyP		1.10	3 mL [S], 15 mg [P], solvent-free, 5 h, Xenon lamp (–)	—	68
MOF-74(HT)		—	0.87 mmol [S], 15 mg [P], solvent-free, 18 h, Xenon lamp (–)	96	409
Mn-TCPP		—	10 mmol [S], 0.5 mol% [P], solvent-free, 48 h, LED lamp (–)	98	69
Ag/MIL-100(Fe)	Carboxylation of terminal alkynes	—	0.5 mmol [S], 30 mg [P], DMF, 12 h, 12 h, Xenon lamp (420–780 nm)	92	410
Cu_2O@HKUST-1	Tandem synthesis of aromatic amines	—	0.2 mmol [S], 50 mg [P], C_2H_5OH, 10 h, Xenon lamp (–)	100	191
Cu_7S_4@ZIF-8	Cyclocondensation	—	0.1 mmol [S], 10 mg [P], CH_2Cl_2, 6 h laser irradiation (1450 nm)	97	218

[a] Conversion of one representative substrate is given; [S] = substrate; [P] = photocatalyst; r. t. = room temperature.

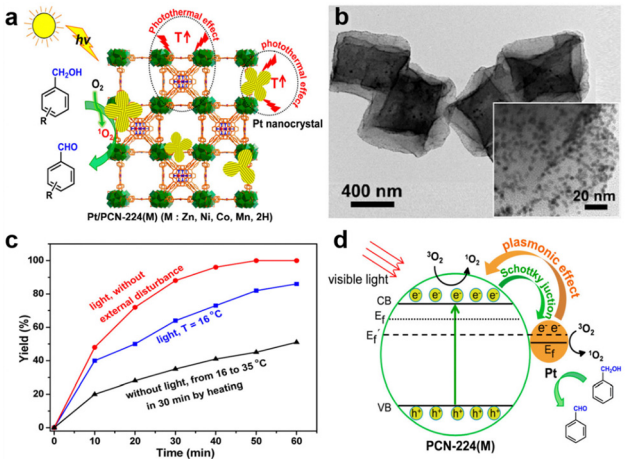

Fig. 31 (a) Schematic illustration of the $^1O_2$-engaged oxidation of alcohols over Pt/PCN-224(M). (b) The representative TEM images of Pt/PCN-224(Zn). (c) Catalytic activity of Pt/PCN-224(Zn) under different conditions. (d) Proposed mechanism for photothermal catalysis over Pt/PCN-224(M). Adapted with permission from ref. 406. Copyright 2017, ACS.

was demonstrated to be an outstanding photocatalyst for alkyne semihydrogenation due to the photothermal effect of Cu NCs and the *in situ* formed active hydrogen species from NH_3BH_3 (Fig. 32a). The Cu–Pd interaction-mediated chemoselectivity is dominated by the steric hindrance effect of the ZIF-8 shell. The catalytic activity of CuPd@ZIF-8 was far exceeded those of other reported metal-based catalysts, with a high turnover frequency of 6799 min^{-1}; in addition, the chemoselectivity remained even upon an extended reaction time.

It is still tricky to realize selective hydrogenation of nitroaromatics in the presence of other reducible groups. Although Pd-based catalysts have been widely utilized in the hydrogenation of nitrocompounds, harsh reaction conditions, including high H_2 pressure and high temperature, are still needed.[417,418] By using Cu_2O as a sacrificial material, Li *et al.* successfully constructed yolk–shell structured PdAg@ZIF-8.[408] In this composite, Ag NCs with excellent LSPR properties can generate heat upon light irradiation to improve the hydrogenation activity of Pd sites. Moreover, the aggregation of small Pd NPs can be avoided under the protection of the MOF shell, which also allows mass transport and the accessibility of Pd sites due to its porous nature. Furthermore, the hollow space between the PdAg core and the MOF shell can contribute to the enrichment of reactants and the preferential adsorption of $-NO_2$ groups. As a result, compared to the core–shell PdAg@ZIF or the PdAg NCs, the yolk–shell structured PdAg@ZIF-8 showed the efficient and selective hydrogenation of nitrostyrene to aminostyrene (Fig. 32b).

6.3. CO_2 addition reactions

CO_2 chemical fixation, which converts CO_2 into valuable chemicals under mild conditions, has attracted increasing amounts of attention because it follows the criteria of green chemistry.[419] However, highly efficient catalysts are still required due to the chemical inertness of CO_2. Ag NPs are active species for CO_2 conversion and are excellent photothermal materials due to their strong LSPR effect.[420] Nevertheless, their catalytic performance is limited by their tendency to aggregate during catalysis. By using a simple solution impregnation-reduction method, Jing *et al.* successfully loaded Ag NPs into MIL-100(Fe) (Fig. 33).[410] The resulting Ag/MIL-100(Fe) composite could be utilized as a photothermal catalyst to efficiently promote the conversion of various aromatic alkynes to the corresponding carboxylic products due to the photothermal effects and catalytic capabilities of both Ag NPs and MIL-100(Fe). Notably, the catalytic performance of the composite under these mild conditions can be impaired by heating, indicating that the conventional heat source should be replaced by light to drive this reaction.

The cycloaddition of epoxides with CO_2 as the C1 source is considered as one of the most promising approaches for the chemical fixation of CO_2 because of the widespread application of the cyclic carbonate products.[421] However, most MOF-based CO_2 cycloaddition reactions have been conducted by direct heating.[422] Chen *et al.* constructed a superstructure MOF and

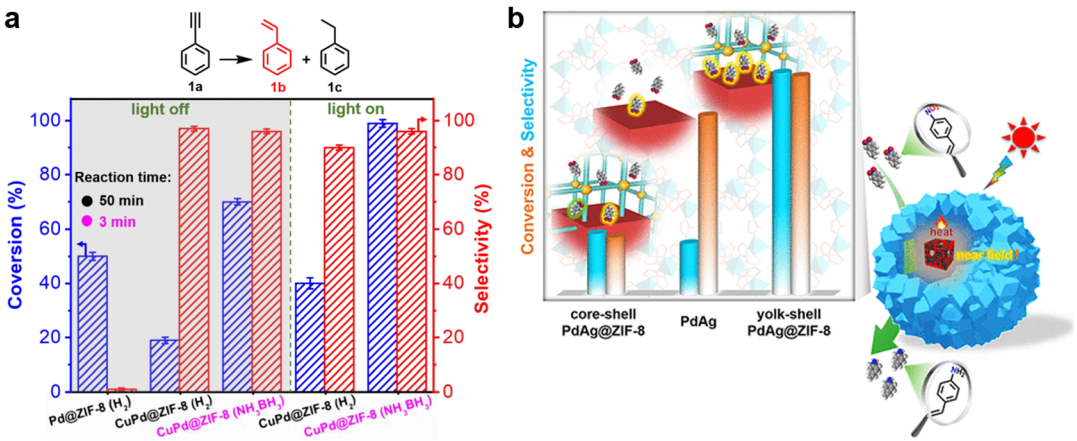

Fig. 32 (a) Semihydrogenation of phenylacetylene over Pd@ZIF-8 (or CuPd@ZIF-8) without (gray background) or with (no background) light irradiation. Adapted with permission from ref. 407. Copyright 2020 ACS. (b) Selective hydrogenation of nitrostyrene to aminostyrene over yolk–shell PdAd@ZIF-8 by photothermal catalysis. Adapted with permission from ref. 408. Copyright 2022 ACS.

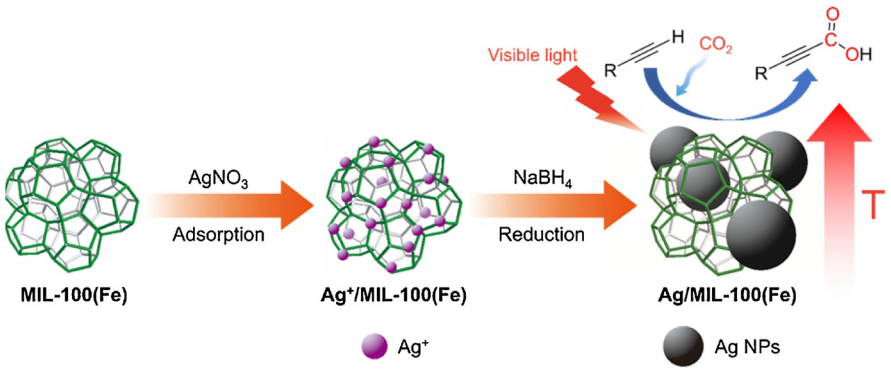

Fig. 33 Schematic illustration showing the synthesis of Ag/MIL-100(Fe) for application in the photothermal conversion of CO_2. Adapted with permission from ref. 410. Copyright 2021 Elsevier.

used it for CO_2 cycloaddition *via* photothermal catalysis.[409] A hierarchical tubular MOF-74 (Cu), named MOF-74-HT, was prepared by immersing a rod-like precursor MOF into a mixed solution of methanol and H_2O with the addition of sodium dodecyl benzene sulfonate as the modulator. The resulting MOF-74-HT with cavities in the core and well-aligned nanosheet arrays on the outer surface showed superior photothermal catalytic performance in the CO_2 cycloaddition with styrene oxide due to the combined photothermal conversion and catalytic capacities.

7. Advanced characterization techniques

The conventional characterization techniques, such as mass spectroscopy, gas chromatograph mass spectroscopy, gas chromatograph, and nuclear magnetic resonance spectroscopy, are used to identify the reaction products and/or determine the yields of products. However, these techniques show limitation in characterizing the reaction intermediates. Thus advanced characterization techniques, which can unveil the key processes in photo(thermal) catalysis, are crucial for understanding the intrinsic mechanisms involved in photo(thermal) catalytic reactions. Benefiting from the atomically well-defined and adjustable structures of MOFs, the photo(thermal) catalytic mechanisms of MOFs in organic transformations can be discussed in depth with the help of advanced characterization techniques. In this section, representative characterization techniques for determining charge reaction kinetics, identifying photo(thermal) catalytic intermediates, and elucidating the related mechanisms are discussed.

7.1. Transient absorption spectroscopy

To determine the CT kinetics, conventional electrochemical characterization techniques, including electrochemical impedance spectroscopy, transient photocurrent spectroscopy, and time-resolved photoluminescence spectroscopy, are readily available. However, their wide application is limited by their low temporal resolution, ranging from microseconds to seconds. TA spectroscopy, which can probe both photogenerated e^- and h^+ and boasts exceptional temporal resolution up to the femtosecond (fs) range, has become a powerful experimental technology for studying ultrafast electronic dynamics processes in MOF-based photo(thermal) catalytic systems for organic transformations.[255,423]

The accessibility of $(dye^{\bullet-})^*$ to reaction substrates, which can alleviate the consumption of back-electron transfer, plays a crucial role in photocatalytic organic reduction reactions.[424] As mentioned above, by regulating the aromatic stacking mode of dyes relative to the CT kinetics in MOFs, Zeng *et al.* realized the efficient photoreduction of inert aryl halides to form C_{Ar}–C/S/P/B bonds.[255] To obtain a deeper understanding, the fs-TA spectra of the radical anionic samples of the organic ligand H_4SNDI and the MOF photocatalyst Cd-SNDI were recorded. After the radical anionic H_4SNDI and Cd-SNDI were irradiated with a laser at 630 nm for *ca.* 1 ps, an excited-state absorption band with a broad coverage band of 400–550 nm was obtained (Fig. 34a and c), providing a decay time (τ) of 93 ps (probed at 445 nm, Fig. 34b) and 164 ps (probed at 480 nm, Fig. 34d), respectively. The τ value of Cd-SNDI was comparable to that of reported $(NDI^{\bullet-})^*$. Moreover, the excited-state absorption of H_4SNDI was blue-shifted and narrower. These results indicate that the prolonged excited-state lifetime of $(NDI^{\bullet-})^*$ in Cd-SNDI enhances the CT process by increasing the accessibility of $(NDI^{\bullet-})^*$ to the substrate to promote the photoreduction efficiency of aryl halides.

7.2. Time-resolved photoluminescence spectroscopy

TRPL spectroscopy can be utilized to decipher the electron dynamics in the photoinduced process by detecting the average lifetime. Furthermore, the reduced lifetime can also be used to study the simultaneous electron transfer from excited photoactive units to catalytic active sites or the EnT process in photocatalytic systems related to ROS generation, both of which are crucial in MOF-based photo(thermal) catalysis for organic transformations.[143,156,269]

By using the mixed-ligand MOF NPF-500-H_2TCPP as a photocatalyst, Fiankor *et al.* realized the efficient photocatalytic oxidation of thioanisole benefiting from the EnT process from the *N*,*N*′-bicarbazole ligand H_4L to the porphyrin ligand H_2TCPP.[143] TRPL technology was used to verify the EnT process in NPF-500-H_2TCPP. The emission lifetime of H_4L in NPF-500-H_2TCPP collected at 440 nm upon excitation at 280 nm was much shorter than that in NPF-500 (Fig. 35), indicating that the

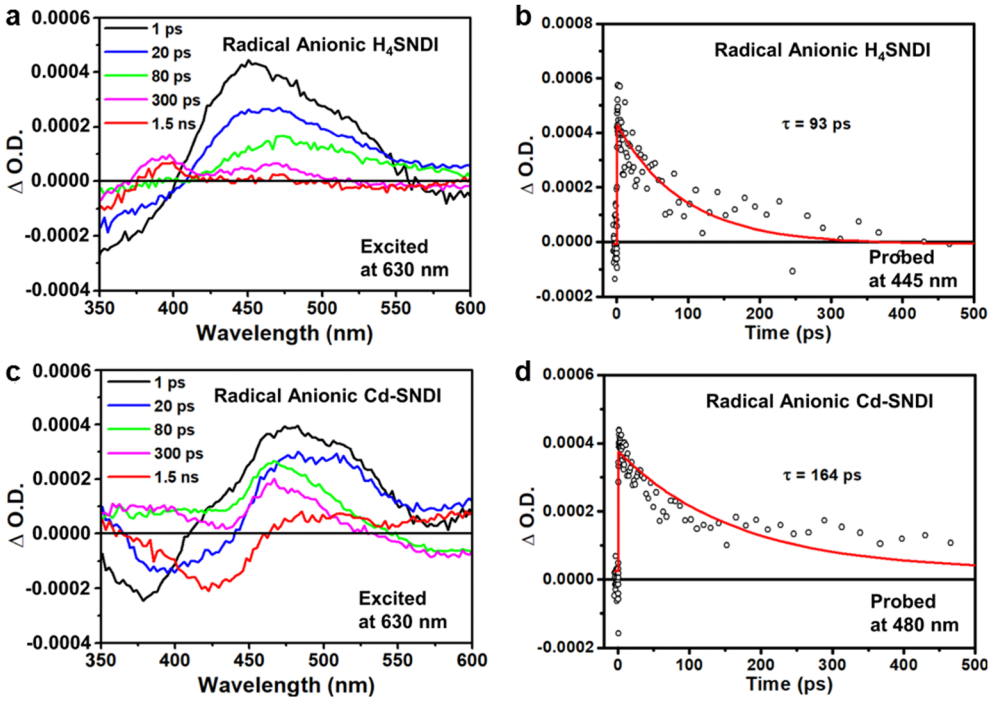

Fig. 34 fs-TA spectra of (a) radical anionic H_4SNDI and (c) Cd-SNDI. The corresponding kinetic traces of (b) H_4SNDI and (d) Cd-SNDI recorded at 445 nm and 480 nm, respectively. Adapted with permission from ref. 255. Copyright 2023 Nature.

integrated H_2TCPP can quench the emission of H_4L. In addition, by fitting the emission decay kinetics, the average emission lifetimes of L in NPF-500 and NPF-500-H_2TCPP were 2.34 and 0.73 ns, respectively. The reduced lifetime further confirmed the efficient EnT process in NPF-500-H_2TCPP, which can mediate the generation of ROS $^1O_2$ for the oxidation of thioanisole.

7.3. X-ray absorption spectroscopy

Based on synchrotron radiation, XAS can probe the local coordination environment of an element by monitoring fluctuations in the absorption of an ejected photoelectron. Generally, XAS is divided into two forms, namely, X-ray absorption near edge structure (XANES) and extended X-ray absorption fine structure (EXAFS) spectroscopy, which can be used to determine the valence states and the coordination structure information (coordination elements, bond lengths, and coordination numbers) of catalytically active metal sites within MOF-based photo(thermal) catalysts for organic transformations, respectively.[423,425]

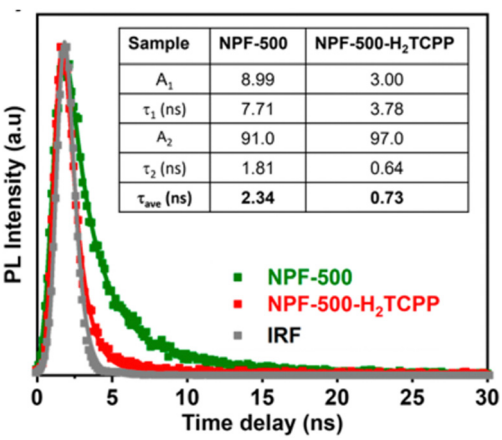

Fig. 35 Emission lifetime decay of the H_4L ligand in NPF-500 and NPF-500-H_2TCPP at 440 nm with an excitation wavelength of 280 nm. Adapted with permission from ref. 143. Copyright 2021, ACS.

To address the Pd reoxidation problem and efficiently improve Pd catalyst turnover for oxidative transformations, Li *et al.* successfully synthesized MOF-based photocatalysts UiO-67-Ir-PdX_2 (X = OAc, TFA), wherein spatially proximate Ir(III) and Pd(II) catalysts were integrated (Fig. 36a).[423] XAS was performed to reveal the oxidation states and coordination environments of Pd and Ir in UiO-67-Ir–PdX_2. Based on XANES results of various standard species (Fig. 36b and d), the oxidation states of Pd(II) and Ir(III) are similar to those of their homogeneous counterparts. Fitting of the EXAFS data for UiO-67-Ir–Pd(OAc)$_2$ at the Pd K-edge revealed that the coordination number of Pd was approximately 4, and the average bond length of Pd–O/N was 2.00 Å (Fig. 36c). The EXAFS characteristic of UiO-67-Ir–Pd(OAc)$_2$ at the Ir L3 edge suggested that the Ir center was six-coordinated, and the average bond lengths of Ir–N_{ppy}, Ir–C_{ppy}, and Ir–C_{bpy} were 2.05 Å, 1.97 Å, and 2.12 Å, respectively (Fig. 36d). These XAS results fully demonstrated that the fabricated Ir(III) and Pd(II) catalysts in the UiO-66 framework possess well-defined coordination geometries and can contribute to the high turnover numbers in various photocatalytic oxidative organic transformations.

7.4. *In situ* Fourier transform infrared spectroscopy

In situ Fourier transform infrared (FTIR) spectroscopy, which has high sensitivity and a fast characterization speed, is a

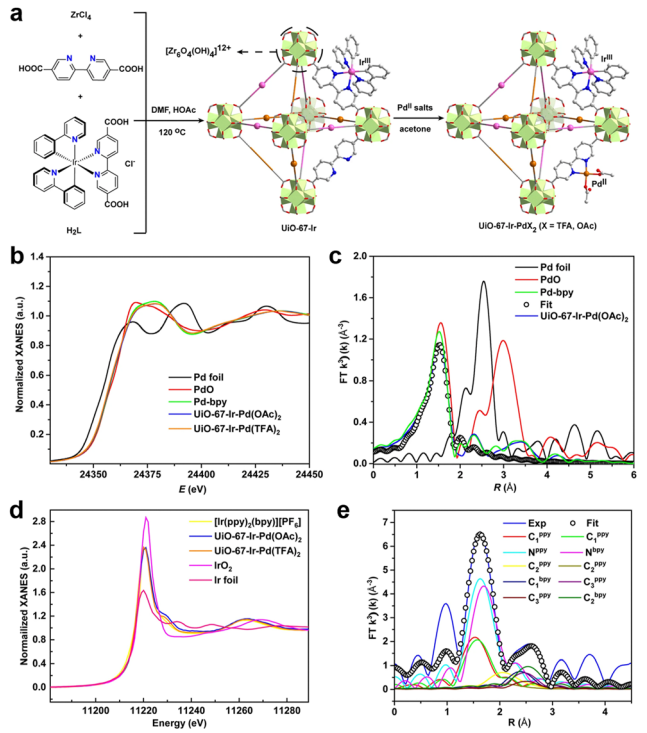

Fig. 36 (a) The synthetic procedure of UiO-67-Ir–PdX_2. (b, d) Normalized XANES features, and EXAFS spectra in R space for (c) Pd K-edge adsorption and (e) Ir L_3-edge adsorption of UiO-67-Ir–$Pd(OAc)_2$ and its counterparts. Adapted with permission from ref. 423. Copyright 2022 Nature.

powerful technique that can be adopted by organic chemists for structural analysis. The characteristic vibration frequencies attributed to specific functional groups in the FTIR spectrum can be utilized to identify the chemical structures of unknown reaction intermediates (a process that resembles "fingerprinting") over MOF-based photo(thermal) catalysis for organic transformations, conducing related mechanism studies at the molecular scale.[175,298]

To further reveal the influence of surface functional sites, including the fully exposed Ti sites and the abundant oxygen vacancy sites, in the NH_2-MIL-125(Ti) nanosheet (MTN) photocatalyst modified with surface Pd on the oxidation of BA, *in situ* FTIR was conducted.[298] In contrast to that of free BA molecules (1300 cm^{-1}), the characteristic peak of C–N bonds in the BA molecules absorbed on the surface of the MTNs shifts to a lower wavenumber (1280 cm^{-1}, Fig. 37a), suggesting that the C–N bonds in BA can be polarized and activated by the low-coordinate Ti metal sites in the MTNs *via* strong chemical adsorption to form Ti–N coordination bonds to enhance BA transformation. Moreover, the adsorption behavior of MTNs for the target product *N*-BBA was also studied. The inappreciable signal of the peak attributed to the C=N bond of the adsorbed product on the spectrum (Fig. 37b) indicates that the product would not be adsorbed on MTNs, supporting that overoxidation can be inhibited in this photocatalytic system.

7.5. Diffuse reflectance infrared Fourier transform spectroscopy

Diffuse reflectance infrared Fourier transform (DRIFTS) spectroscopy, which can collect diffuse scattered signals from infrared radiation on powder samples, is widely applied for probing the structural information of species involved in photocatalytic processes. With regard to organic transformations by MOF-based photo(thermal) catalysis, DRIFTS can be used to trace reaction intermediates, detect the structural information of products, and assess the electron states of catalytic sites.[58,176,256,408]

DRIFTS was carried out to obtain direct evidence of the unique advantages of the hollow microenvironment in yolk–shell nanostructured PdAg@ZIF8 on the selective adsorption and enrichment of substrates, which play a crucial role in the photothermal-catalyzed hydrogenation of nitrostyrene to vinylaniline.[408] Under light irradiation, signals belonging to the $-NO_2$ and –C=C– groups appear simultaneously at 5 min for the core–shell counterpart (Fig. 38a), suggesting its weak substrate enrichment effect and the lack of selective adsorption on both substrates. In contrast, with regard to the yolk–shell nanostructure, the signal of the $-NO_2$ group emerges rapidly within 1 min, and no signal attributed to the –C=C– group is observed (Fig. 38b), indicating that the yolk–shell nanostructure has an excellent capacity to enrich the substrate and selectively adsorbs the $-NO_2$ group. Based on these results,

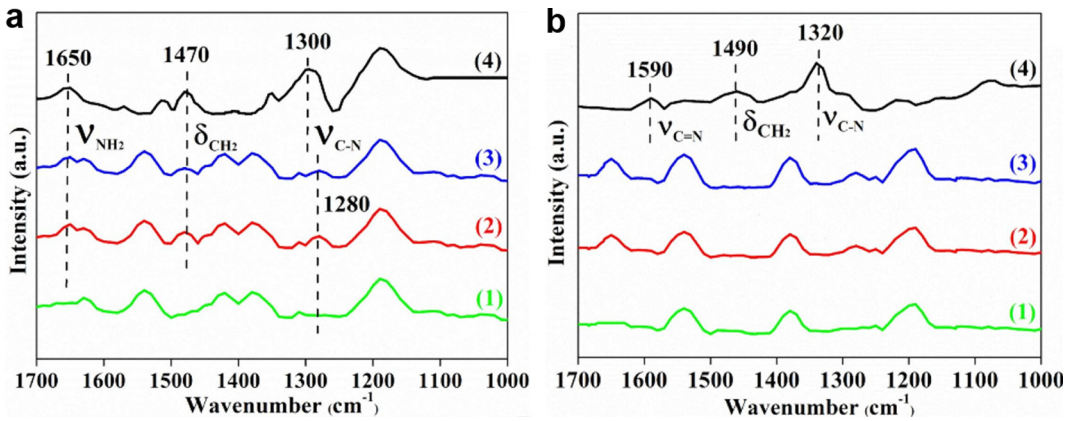

Fig. 37 *In situ* FTIR spectra of MTNs for (a) BA, and (b) *N*-BBA adsorption. (1) After degassing. (2) Adsorption of BA/*N*-BBA. (3) Further evacuation of excess BA/*N*-BBA at chemisorption. (4) BA/*N*-BBA in KBr. Adapted with permission from ref. 298. Copyright 2022 Elsevier.

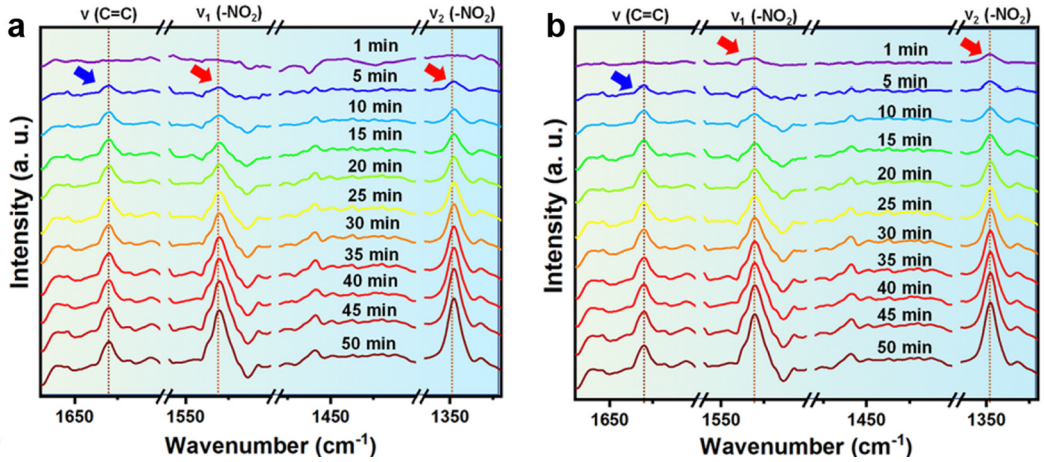

Fig. 38 Time-dependent DRIFTS for nitrobenzene and styrene mixture over PdAg@ZIF-8 catalysts with (a) core–shell and (b) yolk–shell structures under light irradiation. Adapted with permission from ref. 408. Copyright 2022 Elsevier.

the differences in the activity and selectivity of these two photocatalysts can be well understood.

7.6. Electron paramagnetic resonance spectroscopy

EPR spectroscopy is an indispensable technique for monitoring unpaired electrons in materials. Under a static magnetic field, the resonance transitions between different electron spin levels highly depend on the geometric structure and chemical microenvironment of paramagnetic species, which provides accurate EPR signals. As far, EPR spectroscopy has been intensively utilized in MOF-based photo(thermal) catalytic systems to detect various paramagnetic species, including active radicals and transition metal ions involved in organic transformation reactions.[142,155,237,238,248,266,360]

To elucidate the light-induced electron transfer mechanism during the photocatalytic toluene oxidation process by Fe-UiO-66, *in situ* EPR was carried out.[155] After light irradiation in air, an EPR peak at g = 2.02 attributed to $O_2^{\bullet-}$ absorbed on the Zr-oxo clusters appears, while the peak at g = 4.10 assigned to high-spin Fe(III) decreases (Fig. 39a). In addition, with the use of methanol as a hole sacrificial agent and under light irradiation in a N_2 atmosphere, the signal at g = 2.00 ascribed to oxygen-centered active sites in Zr-oxo clusters can be observed upon accepting e^- from Fe(III) (Fig. 39b). However, this signal significantly decreased after the introduction of air, indicating e^- transfer from the Zr-oxo cluster to O_2 molecules. Based on these *in situ* EPR results, e^- transfer from Fe(III) to the Zr-oxo-cluster, namely, the MCCT process, which contributes to the generation of ROS $O_2^{\bullet-}$, can be evidenced.

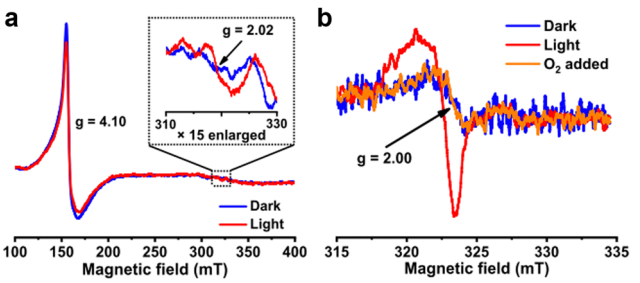

Fig. 39 EPR spectra for the detection of (a) changes in the Fe state before and after irradiation in air and (b) e^- transfer before and after irradiation in N_2 over Fe-UiO-66. Adapted with permission from 155. Copyright 2019 ACS.

8. Summary and outlook

This review comprehensively summarizes recent outstanding progress in the field of MOF-based photo(thermal) catalysis for organic transformations. The main focused aspects include the general mechanisms, the unique advantages of MOFs in photo(thermal) catalysis, common strategies to improve the performance of MOF-based photo(thermal) catalysts, the application of MOF-based photo(thermal) catalysts in organic transformation reactions of oxidation, reduction, coupling, tandem, synergistic redox, and CO_2 addition, as well as advanced characterization techniques that can help researchers understand the mechanisms of MOF-based photo(thermal) catalytic organic transformations. Although MOF-based photo(thermal) catalysts have provided a new platform for organic transformation because of their diverse structures, high specific surface area, and adjustable photophysical properties, this research is still at an early stage. Therefore, herein, some personal insights for advancing the long-term and high-quality development of this research area have been proposed.

First, the types of MOFs used for organic transformation reactions by photo(thermal) catalysis are limited. Currently, mainly Zr-, Ti-, and Cr-based MOFs have been widely studied, while MOF skeletons with traditional transition metals and lanthanides as metal centers are relatively rare. Moreover, in most cases, precious metal complexes such as Ru, Pd, Rh, and Ir are incorporated into and/or supported on MOF skeletons to function as efficient photosensitizers or cocatalysts, which is not favorable from the principle of economy. Hence, synthesis of MOFs with desired metal ions as well as the development of cost-effective sensitizers or cocatalysts are desirable for the

further exploration of MOF-based photo(thermal) catalysts for organic transformations.

Second, the scope and efficiency of organic transformation reactions employing MOF-based photo(thermal) catalysts is still limited. To address this issue, MOFs with new/specific structures should be considered: (i) for tandem reactions, heterometallic MOFs consisting of more than one type of metal elements can realize the synergistic catalysis of different metal ions/clusters are suitable;[426–429] (ii) for photocatalytic asymmetric catalysis, chiral MOFs integrated with photoactive ingredients are targeted;[430,431] (iii) for high reaction efficiency, hierarchically porous MOFs with hierarchical pores can promote reaction kinetics *via* facilitating the diffusion rate and mass transfer of substrates,[432,433] and low-dimensional MOFs with selectively increased active sites or facets,[434–437] are desirable; (iv) for improved reaction selectivity, MOFs with atomically dispersed metal sites can function as durable photocatalysts, are targeted.[438]

Third, although pristine MOFs have been demonstrated to be popular photocatalysts, their application in photo(thermal) catalytic organic transformations is still restricted by their limited active sites. Coupling MOFs with other photo(thermal) active materials (such as metal NPs, POMs, and semiconductors) to construct MOF composites is promising way to develop this field. In this regard, low-temperature synthetic approaches for MOFs,[439,440] which can be utilized to construct MOF composites based on fragile compounds, are highly desirable. In addition, the fabrication of MOF-based core–shell composites,[183,441] which possess more exposed active sites, suppressed aggregation behavior in the photo(thermal) process, as well as efficient interfacial charge transfer and separation facilitated by the tight interaction between the core and shell, is also one of the most promising approaches worthy of attention. Moreover, synergistic catalysis by integrating photocatalysis with photothermal catalysis is believed to be an ideal way to improve the photocatalytic performance toward organic transformations.[442–444]

Fourth, there are still some vague points in the mechanistic study of MOF-based photo(thermal) catalytic organic transformations. More detailed and clearer interpretations of the structure–activity relationship, temporal evolution of the photo-induced electron transition, charge carrier dynamics, and interactions between the excited states and the substrates are still needed. In addition, in contrast to the well-understood CT process, there is still room to clarify and understand the EnT mechanism, as well as the emerged HAT mechanism which has been recently utilized for MOF-based photocatalytic organic transformations through bond energy and polar match effect between the substrate and the HAT catalyst.[445] Therefore, coupling advanced *in situ* or *operando* characterization techniques with computational chemistry or physics, which has been introduced to study the photo(thermal) catalysis of MOFs but at its infancy, is especially desirable for the development of the next generation of efficient MOF-based photo(thermal) catalysts for organic transformation reactions.

Last but not least, to realize industrial practical applications, many important factors still need to be carefully considered: (i) the reaction/cyclic stability and activity due to the structure collapse and/or the mechanical damage of MOFs during the photo(thermal) catalytic process; MOF-derived nano-materials consisting of metals, oxides, chalcogenides, phosphides, or carbides embedded in porous carbon matrix, which possess enhanced stability and effective photocatalytic efficiency, could be considered as the extensibility of the MOF-based photo-(thermal) catalysts for organic transformations;[446,447] (ii) the unsatisfactory selectivity to target products in most MOF-based photo(thermal) catalytic systems; (iii) the lack of a scientific and recognized measure of efficiency that allows to get an unequivocally evaluation on the catalytic performances of different photocatalytic systems; (iv) the relatively low cost/performance ratio resulting from the high cost of functional components in MOF-based photo(thermal) catalysts, likely precious metal complexes and porphyrin derivatives; and (v) the potential problems that emerges when large-scale reactions for industrial production are conducted.

In summary, organic transformations driven by MOF-based photo(thermal) catalysts are still in their infancy, and there are both promising opportunities and tricky challenges. If these challenges can be solved due to the ever-increasing progress in the synthesis of MOF-based materials and the in-depth study of the properties and catalytic mechanisms of MOF-based photo(thermal) catalysts, a bright future wherein MOF-based photocatalysts contribute to the mass production of high-value-added chemicals utilizing real-life solar fuel can be envisioned.

Data availability

No primary research results, software or code have been included and no new data were generated or analysed as part of this review.

Conflicts of interest

There are no conflicts to declare.

Acknowledgements

This work is supported by the National Key Research and Development Program of China (2021YFA1500400), the NSFC (22331009, U22A20401, 22205005), the Natural Science Foundation of Hunan Province (2023JJ30010), the Natural Science Foundation Project of Changsha City (kq2208217), the Strategic Priority Research Program of the Chinese Academy of Sciences (XDB0450302 and XDB0540000), and Fundamental Research Funds for the Central Universities (WK9990000137).

References

1 A. F. de Almeida, R. Moreira and T. Rodrigues, *Nat. Rev. Chem.*, 2019, **3**, 589–604.
2 A. Jordan, C. G. J. Hall, L. R. Thorp and H. F. Sneddon, *Chem. Rev.*, 2022, **122**, 6749–6794.

3 W. Li, A. Elzatahry, D. Aldhayan and D. Zhao, *Chem. Soc. Rev.*, 2018, **47**, 8203–8237.
4 A. Vega-Penaloza, J. Mateos, X. Companyo, M. Escudero-Casao and L. Dell'Amico, *Angew. Chem., Int. Ed.*, 2021, **60**, 1082–1097.
5 Y. Lee and M. S. Kwon, *Eur. J. Org. Chem.*, 2020, 6028–6043.
6 Y. Markushyna and A. Savateev, *Eur. J. Org. Chem.*, 2022, e202200026.
7 P. Li, T. Zhang, M. A. Mushtaq, S. Wu, X. Xiang and D. Yan, *Chem. Rec.*, 2021, **21**, 841–857.
8 W. Zeng, X. Ye, Y. Dong, Y. Zhang, C. Sun, T. Zhang, X. Guan and L. Guo, *Coord. Chem. Rev.*, 2024, **508**, 215753.
9 C. K. Prier, D. A. Rankic and D. W. C. MacMillan, *Chem. Rev.*, 2013, **113**, 5322–5363.
10 D. A. Nicewicz and T. M. Nguyen, *ACS Catal.*, 2014, **4**, 355–360.
11 N. A. Romero and D. A. Nicewicz, *Chem. Rev.*, 2016, **116**, 10075–10166.
12 D. Rota Martir and E. Zysman-Colman, *Chem. Commun.*, 2019, **55**, 139–158.
13 Y.-L. Li, A.-J. Li, S.-L. Huang, J. J. Vittal and G.-Y. Yang, *Chem. Soc. Rev.*, 2023, **52**, 4725–4754.
14 T. Banerjee, F. Podjaski, J. Kroeger, B. P. Biswal and B. V. Lotsch, *Nat. Rev. Mater.*, 2021, **6**, 168–190.
15 C. Dai and B. Liu, *Energy Environ. Sci.*, 2020, **13**, 24–52.
16 T.-X. Wang, H.-P. Liang, D. A. Anito, X. Ding and B.-H. Han, *J. Mater. Chem. A*, 2020, **8**, 7003–7034.
17 X. Yuan and H. Remita, *Top. Curr. Chem.*, 2022, **380**, 32.
18 T. Li, Y. Li, C. Guo and Y. Hu, *Chem. Commun.*, 2024, **60**, 2320–2348.
19 K. Sun, Y. Qian and H.-L. Jiang, *Angew. Chem., Int. Ed.*, 2023, **62**, e202217565.
20 J.-D. Xiao, R. Li and H.-L. Jiang, *Small Methods*, 2023, **7**, 2201258.
21 S. Navalón, A. Dhakshinamoorthy, M. Álvaro, B. Ferrer and H. García, *Chem. Rev.*, 2023, **123**, 445–490.
22 H. Liu, M. Cheng, Y. Liu, J. Wang, G. Zhang, L. Li, L. Du, G. Wang, S. Yang and X. Wang, *Energy Environ. Sci.*, 2022, **15**, 3722–3749.
23 J.-D. Xiao and H.-L. Jiang, *Acc. Chem. Res.*, 2019, **52**, 356–366.
24 S. Subudhi, D. Rath and K. M. Parida, *Catal. Sci. Technol.*, 2018, **8**, 679–696.
25 X. Yu, L. Wang and S. M. Cohen, *CrystEngComm*, 2017, **19**, 4126–4136.
26 X. Deng, Z. Li and H. Garcia, *Chem.– Eur. J.*, 2017, **23**, 11189–11209.
27 H. Zhang, R. Sun, D.-C. Li and J.-M. Dou, *Chin. J. Struct. Chem.*, 2022, **41**, 2211071–2211083.
28 G. Lu, F. Chu, X. Huang, Y. Li, K. Liang and G. Wang, *Coord. Chem. Rev.*, 2022, **450**, 214240.
29 I. S. Khan, L. Garzon-Tovar, D. Mateo and J. Gascon, *Eur. J. Inorg. Chem.*, 2022, e202200316.
30 Q. Wang, Q. Gao, A. M. Al-Enizi, A. Nafady and S. Ma, *Inorg. Chem. Front.*, 2020, **7**, 300–339.
31 T. Zhang, Y. Jin, Y. Shi, M. Li, J. Li and C. Duan, *Coord. Chem. Rev.*, 2019, **380**, 201–229.
32 H. Chen, H. S. Jena, X. Feng, K. Leus and P. Van der Voort, *Angew. Chem., Int. Ed.*, 2022, **61**, e202204938.
33 M. Rosaria di Nunzio, E. Caballero-Mancebo, B. Cohen and A. Douhal, *J. Photochem. Photobiol., C*, 2020, **44**, 100355.
34 R. Ham, C. J. Nielsen, S. Pullen and J. N. H. Reek, *Chem. Rev.*, 2023, **123**, 5225–5261.
35 A. Dhakshinamoorthy, Z. Li, S. Yang and H. Garcia, *Chem. Soc. Rev.*, 2024, **53**, 3002–3035.
36 V. H. Dang, T.-A. Nguyen, M.-V. Le, D. Q. Nguyen, Y. H. Wang and J. C. S. Wu, *Chem. Eng. J.*, 2024, **484**, 149213.
37 Q. Tang, T. Li, W. Tu, H. Wang, Y. Zhou and Z. Zou, *Adv. Funct. Mater.*, 2024, **34**, 2311609.
38 H. Shen, M. Yang, L. Hao, J. Wang, J. Strunk and Z. Sun, *Nano Res.*, 2022, **15**, 2773–2809.
39 S. Fukuzumi, J. Jung, Y. Yamada, T. Kojima and W. Nam, *Chem. – Asian J.*, 2016, **11**, 1138–1150.
40 R. Su, Y. Zhu, B. Gao and Q. Li, *Water Res.*, 2024, **251**, 121119.
41 L. Xiong and J. Tang, *Adv. Energy Mater.*, 2021, **11**, 2003216.
42 H. Han, Y. Yang, J. Liu, X. Zheng, X. Wang, S. Meng, S. Zhang, X. Fu and S. Chen, *ACS Appl. Energy Mater.*, 2020, **3**, 11275–11284.
43 J. Bisquert, A. Zaban, M. Greenshtein and I. Mora-Seró, *J. Am. Chem. Soc.*, 2004, **126**, 13550.
44 D. y Davydova, A. de la Cadena, D. Akimov and B. Dietzek, *Laser Photonics Rev.*, 2016, **10**, 62–81.
45 Y. Xiao, Q. Sun, J. Leng and S. Jin, *J. Phys. Chem. Lett.*, 2024, **15**, 3390–3403.
46 G. E. Cutsail, III and S. DeBeer, *ACS Catal.*, 2022, **12**, 5864–5886.
47 K. Ye, K. Li, Y. Lu, Z. Guo, N. Ni, H. Liu, Y. Huang, H. Ji and P. Wang, *TrAC, Trends Anal. Chem.*, 2019, **116**, 102–108.
48 P. Sindhu, K. S. Ananthram, A. Jain, K. Tarafder and N. Ballav, *Nat. Commun.*, 2022, **13**, 7665.
49 X. Li, J. Yu, D. J. Gosztola, H. C. Fry and P. Deria, *J. Am. Chem. Soc.*, 2019, **141**, 16849–16857.
50 W. Zhang, W. Huang, B. Wu, J. Yang, J. Jin and S. Zhang, *Coord. Chem. Rev.*, 2023, **491**, 215235.
51 J. Guo, Q. Xia, W. Tang, Z. Li, X. Wu, L.-J. Liu, W.-P. To, H.-X. Shu, K.-H. Low, P. C. Y. Chow, T. W. B. Lo and J. He, *Nat. Catal.*, 2024, **7**, 307–320.
52 F. Chen, T. Ma, T. Zhang, Y. Zhang and H. Huang, *Adv. Mater.*, 2021, **33**, 2005256.
53 K. Sharma, A. Kumar, T. Ahamad, S. M. Alshehri, P. Singh, S. Thakur, Q. Van Le, C. Wang, T.-T. Huynh, V.-H. Nguyen and P. Raizada, *Environ. Chem. Lett.*, 2022, **20**, 2781–2795.
54 D. S. Lee, V. K. Soni and E. J. Cho, *Acc. Chem. Res.*, 2022, **55**, 2526–2541.
55 F. Strieth-Kalthoff and F. Glorius, *Chem*, 2020, **6**, 1888–1903.
56 Z. Wang and C. Wang, *Adv. Mater.*, 2021, **33**, 2005819.
57 F. Strieth-Kalthoff and F. Glorius, *Chem*, 2020, **6**, 1888.
58 H. Zhang, S. Liu, A. Zheng, P. Wang, Z. Zheng, Z. Wang, H. Cheng, Y. Dai, B. Huang and Y. Liu, *Angew. Chem., Int. Ed.*, 2024, **63**, e202400965.

59 T. Zhang, P. Wang, Z. Gao, Y. An, C. He and C. Duan, *RSC Adv.*, 2018, **8**, 32610–32620.
60 S.-D. Wang, C.-L. Lai, Y.-X. Zhang, S.-T. Bao, K.-L. Lv and L.-L. Wen, *J. Mater. Chem. A*, 2022, **10**, 20975–20983.
61 K. Sztandera, M. Gorzkiewicz and B. Klajnert-Maculewicz, *Mol. Pharm.*, 2019, **16**, 1–23.
62 I. Kriegel, F. Scotognella and L. Manna, *Phys. Rep.*, 2017, **674**, 1–52.
63 B. Han, Y.-L. Zhang, Q.-D. Chen and H.-B. Sun, *Adv. Funct. Mater.*, 2018, **28**, 1802235.
64 L. Xiao, X. Chen, X. Yang, J. Sun and J. Geng, *ACS Appl. Polym. Mater.*, 2020, **2**, 4273–4288.
65 D. Mateo, J. L. Cerrillo, S. Durini and J. Gascon, *Chem. Soc. Rev.*, 2021, **50**, 2173–2210.
66 O. Shelonchik, N. Lemcoff, R. Shimoni, A. Biswas, E. Yehezkel, D. Yesodi, I. Hod and Y. Weizmann, *Nat. Commun.*, 2024, **15**, 1154.
67 P.-Y. Liao, J.-X. Li, J.-C. Liu, Q. Xiong, Z.-Y. Ruan, L. Tao, W. Deng, S.-D. Jiang, J.-H. Jia and M.-L. Tong, *Angew. Chem., Int. Ed.*, 2024, **63**, e202401448.
68 H. Zhang, G. Zhai, L. Lei, C. Zhang, Y. Liu, Z. Wang, H. Cheng, Z. Zheng, P. Wang, Y. Dai and B. Huang, *J. Colloid Interface Sci.*, 2022, **625**, 33–40.
69 N. Sharma, S. S. Dhankhar and C. M. Nagaraja, *Microporous Mesoporous Mater.*, 2019, **280**, 372–378.
70 M. Zhao, H.-B. Wang, L.-N. Ji and Z.-W. Mao, *Chem. Soc. Rev.*, 2013, **42**, 8360–8375.
71 Y. Zhang, Y. Jiang, A. Nafady, Z. Tang, A. M. Al-Enizi, K. Tan and S. Ma, *ACS Cent. Sci.*, 2023, **9**, 1692–1701.
72 L. Jiao, J. Wang and H.-L. Jiang, *Acc. Mater. Res.*, 2021, **2**, 327–339.
73 J. Sui, M.-L. Gao, B. Qian, C. Liu, Y. Pan, Z. Meng, D. Yuan and H.-L. Jiang, *Sci. Bull.*, 2023, **68**, 1886–1893.
74 X. Ma, H. Liu, W. Yang, G. Mao, L. Zheng and H.-L. Jiang, *J. Am. Chem. Soc.*, 2021, **143**, 12220–12229.
75 S. Wang, Z. Ai, X. Niu, W. Yang, R. Kang, Z. Lin, A. Waseem, L. Jiao and H.-L. Jiang, *Adv. Mater.*, 2023, **35**, 2302512.
76 T. M. Rayder, A. T. Bensalah, B. Li, J. A. Byers and C.-K. Tsung, *J. Am. Chem. Soc.*, 2021, **143**, 1630–1640.
77 J. Sui, H. Liu, S. Hu, K. Sun, G. Wan, H. Zhou, X. Zheng and H.-L. Jiang, *Adv. Mater.*, 2022, **34**, 2109203.
78 S. Natarajan and K. Manna, *ACS Org. Inorg. Au*, 2024, **4**, 59–90.
79 X. Li, L. Liu, X. Ren, J. Gao, Y. Huang and B. Liu, *Sci. Adv.*, 2020, **6**, eabb6833.
80 Y. Chen, R. Gao, S. Ji, H. Li, K. Tang, P. Jiang, H. Hu, Z. Zhang, H. Hao, Q. Qu, X. Liang, W. Chen, J. Dong, D. Wang and Y. Li, *Angew. Chem., Int. Ed.*, 2022, **61**, e202207879.
81 Z. Lu, J. Liu, X. Zhang, Y. Liao, R. Wang, K. Zhang, J. Lyu, O. K. Farha and J. T. Hupp, *J. Am. Chem. Soc.*, 2020, **142**, 21110–21121.
82 W. Gong, X. Chen, W. Zhang, K. O. Kirlikovali, B. Nan, Z. Chen, R. Si, Y. Liu, O. K. Farha and Y. Cui, *J. Am. Chem. Soc.*, 2022, **144**, 3117–3126.
83 S. Wang, Z. Ai, X. Niu, W. Yang, R. Kang, Z. Lin, A. Waseem, L. Jiao and H.-L. Jiang, *Adv. Mater.*, 2023, **35**, 2302512.
84 Z. Li, D. Wang, Y. Wu and Y. Li, *Natl. Sci. Rev.*, 2018, **5**, 673–689.
85 M. Xu, D. Li, K. Sun, L. Jiao, C. Xie, C. Ding and H.-L. Jiang, *Angew. Chem., Int. Ed.*, 2021, **60**, 16372–16376.
86 X. B. Liu and Y. Huang, *Coord. Chem. Rev.*, 2023, **489**, 215173.
87 H. Deng, C. J. Doonan, H. Furukawa, R. B. Ferreira, J. Towne, C. B. Knobler, B. Wang and O. M. Yaghi, *Science*, 2010, **327**, 846–850.
88 X. Xu, L. Gao and S. Yuan, *Dalton Trans.*, 2023, **52**, 15233–15252.
89 S. Ko, U. Ryu, H. Park, A. M. Fracaroli, W. Moon and K. M. Choi, *J. Am. Chem. Soc.*, 2023, **145**, 3101–3107.
90 Y.-Y. Zhu, Y.-Y. He, Y.-X. Li, C.-H. Liu and W. Lin, *Chem. – Eur. J.*, 2024, **30**, e202400842.
91 C.-C. Cao, C.-X. Chen, Z.-W. Wei, Q.-F. Qiu, N.-X. Zhu, Y.-Y. Xiong, J.-J. Jiang, D. Wang and C.-Y. Su, *J. Am. Chem. Soc.*, 2019, **141**, 2589–2593.
92 M. Eddaoudi, J. Kim, N. Rosi, D. Vodak, J. Wachter, M. O'Keeffe and O. M. Yaghi, *Science*, 2002, **295**, 469–472.
93 J. T. Bryant, M. W. Logan, Z. Chen, M. Djokic, D. R. Cairnie, D. A. Vazquez-Molina, A. Nijamudheen, K. R. Langlois, M. J. Markley, G. Pombar, A. A. Holland, J. D. Caranto, J. K. Harper, A. J. Morris, J. L. Mendoza-Cortes, T. Jurca, K. W. Chapman and F. J. Uribe-Romo, *J. Am. Chem. Soc.*, 2023, **145**, 4589–4600.
94 S. Zhang, L. Lu, J. Jiang, N. Liu, B. Zhao, M. Xu, P. Cheng and W. Shi, *Adv. Mater.*, 2024, **36**, 2403464.
95 C. Fang, L. Liu, J. Weng, S. Zhang, X. Zhang, Z. Ren, Y. Shen, F. Meng, B. Zheng, S. Li, J. Wu, W. Shi, S. Lee, W. Zhang and F. Huo, *Angew. Chem., Int. Ed.*, 2021, **60**, 976–982.
96 Y.-S. Wei, M. Zhang, P.-Q. Liao, R.-B. Lin, T.-Y. Li, G. Shao, J.-P. Zhang and X.-M. Chen, *Nat. Commun.*, 2015, **6**, 8348.
97 B. An, Z. Li, Y. Song, J. Zhang, L. Zeng, C. Wang and W. Lin, *Nat. Catal.*, 2019, **2**, 709–717.
98 Q. Yang, Q. Xu, S.-H. Yu and H.-L. Jiang, *Angew. Chem., Int. Ed.*, 2016, **55**, 3685–3689.
99 M. T. Huxley, A. Burgun, H. Ghodrati, C. J. Coghlan, A. Lemieux, N. R. Champness, D. M. Huang, C. J. Doonan and C. J. Sumby, *J. Am. Chem. Soc.*, 2018, **140**, 6416–6425.
100 B. An, Z. Li, Z. Wang, X. Zeng, X. Han, Y. Cheng, A. M. Sheveleva, Z. Zhang, F. Tuna, E. J. L. McInnes, M. D. Frogley, A. J. Ramirez-Cuesta, L. S. Natrajan, C. Wang, W. Lin, S. Yang and M. Schröder, *Nat. Mater.*, 2022, **21**, 932–938.
101 S. Li, W. Han, Q.-F. An, K.-T. Yong and M.-J. Yin, *Adv. Funct. Mater.*, 2023, **33**, 2303447.
102 I. E. Khalil, C. Xue, W. Liu, X. Li, Y. Shen, S. Li, W. Zhang and F. Huo, *Adv. Funct. Mater.*, 2021, **31**, 2010052.
103 Z. Fan, Z. Wang, M. Cokoja and R. A. Fischer, *Catal. Sci. Technol.*, 2021, **11**, 2396–2402.

104 S. Dai, C. Simms, G. Patriarche, M. Daturi, A. Tissot, T. N. Parac-Vogt and C. Serre, *Nat. Commun.*, 2024, **15**, 3434.
105 S. Dissegna, K. Epp, W. R. Heinz, G. Kieslich and R. A. Fischer, *Adv. Mater.*, 2018, **13**, 1704501.
106 L. Pukdeejorhor, S. Wannapaiboon, J. Berger, K. Rodewald, S. Thongratkaew, S. Impeng, J. Warnan, S. Bureekaew and R. A. Fischer, *J. Mater. Chem. A*, 2023, **11**, 9143–9151.
107 S.-Q. Wang, X. Wang, X.-M. Cheng, J. Ma and W.-Y. Sun, *J. Mater. Chem. A*, 2022, **10**, 16396–16402.
108 Y. Kondo, Y. Kuwahara, K. Mori and H. Yamashita, *J. Phys. Chem. C*, 2021, **125**, 27909–27918.
109 G. Ren, J. Zhao, Z. Zhao, Z. Li, L. Wang, Z. Zhang, C. Li and X. Meng, *Angew. Chem., Int. Ed.*, 2023, **63**, e202314408.
110 C. Liu, Y.-Z. Shi, Q. Chen, B.-H. Ye, J.-H. Bi, J. C. Yu and L. Wu, *Rare Met.*, 2024, DOI: 10.1007/s12598-024-02693-x.
111 X. Wang, G. Fan, S. Guo, R. Gao, Y. Guo, C. Han, Y. Gao, J. Zhang, X. Gu and L. Wu, *Angew. Chem., Int. Ed.*, 2024, **63**, e202404258.
112 L. Li, Y. Xia, M. Zeng and L. Fu, *Chem. Soc. Rev.*, 2022, **51**, 7327–7343.
113 H. E. Rudel, M. K. M. Lane, C. L. Muhich and J. B. Zimmerman, *ACS Nano*, 2020, **14**, 16472–16501.
114 X.-M. Cheng, J. Zhao and W.-Y. Sun, *EnergyChem*, 2022, **4**, 100084.
115 Y. Yu, Z. Zhu and H. Huang, *Adv. Mater.*, 2024, **36**, 2311148.
116 S. Sun, L. He, M. Yang, J. Cui and S. Liang, *Adv. Funct. Mater.*, 2022, **32**, 2106982.
117 G. Di Liberto, L. A. Cipriano, S. Tosoni and G. Pacchioni, *Chem. – Eur. J.*, 2021, **27**, 13306–13317.
118 M. Shi, G. Ren, Z. Zhang, Z. Li and X. Meng, *J. Catal.*, 2024, **429**, 115300.
119 W. Yang, H.-J. Wang, R.-R. Liu, J.-W. Wang, C. Zhang, C. Li, D.-C. Zhong and T.-B. Lu, *Angew. Chem., Int. Ed.*, 2021, **60**, 409–414.
120 M.-L. Gao, L. Li, Z.-X. Sun, J.-R. Li and H.-L. Jiang, *Angew. Chem., Int. Ed.*, 2022, **61**, e202211216.
121 F. Guo, M. Yang, R.-X. Li, Z.-Z. He, Y. Wang and W.-Y. Sun, *ACS Catal.*, 2022, **12**, 9486–9493.
122 L. Liu, S. Du, Y. Xiao, X. Guo, S. Jin, G. Shao and F. Zhang, *Appl. Catal., B*, 2023, **338**, 123094.
123 F. Guo, J.-H. Guo, P. Wang, Y.-S. Kang, Y. Liu, J. Zhao and W.-Y. Sun, *Chem. Sci.*, 2019, **10**, 4834–4838.
124 Y. Yan, C. Li, Y. Wu, J. Gao and Q. Zhang, *J. Mater. Chem. A*, 2020, **8**, 15245–15270.
125 G.-Y. Qiao, D. Guan, S. Yuan, H. Rao, X. Chen, J.-A. Wang, J.-S. Qin, J.-J. Xu and J. Yu, *J. Am. Chem. Soc.*, 2021, **143**, 14253–14260.
126 Z. Hu, Y. Wang and D. Zhao, *Chem. Soc. Rev.*, 2021, **50**, 4629–4683.
127 P. D. Harvey, *J. Mater. Chem. C*, 2021, **9**, 16885–16910.
128 F. P. Kinik, A. Ortega-Guerrero, D. Ongari, C. P. Ireland and B. Smit, *Chem. Soc. Rev.*, 2021, **50**, 3143–3177.
129 Y. Chen, A.-G. Liu, P.-D. Liu, Z.-T. Chen, S.-Y. Liu and B. Li, *J. Mater. Chem. A*, 2023, **11**, 18236–18246.
130 T. Kitao, Y. Zhang, S. Kitagawa, B. Wang and T. Uemura, *Chem. Soc. Rev.*, 2017, **46**, 3108–3133.
131 J. Hao, X. Xu, H. Fei, L. Li and B. Yan, *Adv. Mater.*, 2018, **30**, 1705634.
132 Z. Wang, X. Yue and Q. Xiang, *Coord. Chem. Rev.*, 2024, **504**, 215674.
133 X. Qiu, Y. Zhu, X. Zhang, Y. Zhang, L. T. Menisa, C. Xia, S. Liu and Z. Tang, *Sol. RRL*, 2020, **4**, 1900449.
134 Z. Wu, X. Huang, H. Zheng, P. Wang, G. Hai, W. Dong and G. Wang, *Appl. Catal., B*, 2018, **224**, 479–487.
135 A. Valverde-Gonzalez, M. Pintado-Sierra, A. Rasero-Almansa, F. Sanchez and M. Iglesias, *Appl. Catal., A*, 2021, **623**, 118287.
136 M. Campanelli, T. Del Giacco, F. De Angelis, E. Mosconi, M. Taddei, F. Marmottini, R. D'Amato and F. Costantino, *ACS Appl. Mater. Interfaces*, 2019, **11**, 45031–45037.
137 Y. Tang, G. Ji, H. Li, H. Gao, C. He, L. Zhao and C. Duan, *Inorg. Chem. Front.*, 2023, **10**, 5439–5451.
138 K. Wu, J.-K. Jin, X.-Y. Liu, Y.-L. Huang, P.-W. Cheng, M. Xie, J. Zheng, W. Lu and D. Li, *J. Mater. Chem. C*, 2022, **10**, 11967–11974.
139 M. Rouzifar, S. Sobhani, A. Farrokhi and J. M. Sansano, *J. Photochem. Photobiol., A*, 2024, **447**, 115263.
140 S. Wang, L. Chen, M. Wahiduzzaman, A. Tissot, L. Zhou, I. A. Ibarra, A. Gutiérrez-Alejandre, J. S. Lee, J.-S. Chang, Z. Liu, J. Marrot, W. Shepard, G. Maurin, Q. Xu and C. Serre, *Matter*, 2021, **4**, 182–194.
141 J.-K. Jin, K. Wu, X.-Y. Liu, G.-Q. Huang, Y.-L. Huang, D. Luo, M. Xie, Y. Zhao, W. Lu, X.-P. Zhou, J. He and D. Li, *J. Am. Chem. Soc.*, 2021, **143**, 21340–21349.
142 W.-J. Xu, B.-X. Huang, G. Li, F. Yang, W. Lin, J.-X. Gu, H.-G. Deng, Z.-G. Gu and H.-G. Jin, *ACS Catal.*, 2023, **13**, 5723–5732.
143 C. Fiankor, J. Nyakuchena, R. S. H. Khoo, X. Zhang, Y. Hu, S. Yang, J. Huang and J. Zhang, *J. Am. Chem. Soc.*, 2021, **143**, 20411–20418.
144 X.-T. Liu, B. B. Qian, T. Zhang, H.-X. Nie, N.-N. Xiao, H.-Y. Shi, Z. Chang, Y. S. Zhao and X.-H. Bu, *Matter*, 2022, **5**, 2918–2932.
145 B. Zhang, J. Xu, C.-T. Li, H.-L. Huang, M.-X. Chen, M.-H. Yu, Z. Chang and X.-H. Bu, *Angew. Chem., Int. Ed.*, 2023, **62**, e202303262.
146 M. C. Simons, S. D. Prinslow, M. Babucci, A. S. Hoffman, J. Hong, J. G. Vitillo, S. R. Bare, B. C. Gates, C. C. Lu, L. Gagliardi and A. Bhan, *J. Am. Chem. Soc.*, 2021, **143**, 12165–12174.
147 S. Kumar, S. Vijayan, K. Goyal, M. Kathuria and S. Gulati, in *Metal-Organic Frameworks (MOFs) as Catalysts*, ed. S. Gulati, Springer Nature Singapore, Singapore, 2022, pp.99–123.
148 M. Y. Masoomi, A. Morsali, A. Dhakshinamoorthy and H. Garcia, *Angew. Chem., Int. Ed.*, 2019, **58**, 15188–15205.
149 J. Liu, J. Xue, G.-P. Yang, L.-L. Dang, L.-F. Ma, D.-S. Li and Y.-Y. Wang, *Coord. Chem. Rev.*, 2022, **463**, 214521.
150 L. J. Wang, H. Deng, H. Furukawa, F. Gándara, K. E. Cordova, D. Peri and O. M. Yaghi, *Inorg. Chem.*, 2014, **53**, 5881–5883.
151 Z. Ji, T. Li and O. M. Yaghi, *Science*, 2020, **369**, 674–680.

152 D. Sun, W. Liu, M. Qiu, Y. Zhang and Z. Li, *Chem. Commun.*, 2015, **51**, 2056–2059.
153 A. Bhattacharyya, M. Gutiérrez, B. Cohen, A. Valverde-González, M. Iglesias and A. Douhal, *Mater. Today, Energy*, 2022, **29**, 101125.
154 A. Melilloa, M. Cabrero-Antoninoa, S. Navalóna, M. Álvaroa, B. Ferrera and H. García, *Appl. Catal., B*, 2020, **278**, 119345.
155 C. Xu, Y. Pan, G. Wan, H. Liu, L. Wang, H. Zhou, S.-H. Yu and H.-L. Jiang, *J. Am. Chem. Soc.*, 2019, **141**, 19110–19117.
156 H. D. Park, M. Dincă and Y. Román-Leshkov, *ACS Cent. Sci.*, 2017, **3**, 444–448.
157 L. Gutierrez, S. S. Mondal, A. Bucci, N. Kandoth, E. C. Escudero-Adan, A. Shafir and J. Lloret-Fillol, *ChemSusChem*, 2020, **13**, 3418–3428.
158 H.-Q. Zheng, Y. Cui and G. Qian, *Acc. Mater. Res.*, 2023, **4**, 982–994.
159 R.-B. Lin, Z. Zhang and B. Chen, *Acc. Chem. Res.*, 2021, **54**, 3362–3376.
160 M. I. Gonzalez, A. B. Turkiewicz, L. E. Darago, J. Oktawiec, K. Bustillo, F. Grandjean, G. J. Long and J. R. Long, *Nature*, 2020, **577**, 64–68.
161 L. Feng, G. S. Day, K.-Y. Wang, S. Yuan and H.-C. Zhou, *Chem*, 2020, **6**, 2902–2923.
162 Y. Kinoshita, N. Deromachi, T. Kajiwara, T. Koizumi, S. Kitagawa, H. Tamiaki and K. Tanaka, *ChemSusChem*, 2023, **16**, e202300032.
163 G. Han, G. Li, J. Huang, C. Han, C. Turro and Y. Sun, *Nat. Commun.*, 2022, **13**, 2288.
164 A. Mahammed and Z. Gross, *Coord. Chem. Rev.*, 2019, **379**, 121–132.
165 S. Yu, R.-X. Zhu, K.-K. Niu, N. Han, H. Liu and L.-B. Xing, *Chem. Sci.*, 2024, **15**, 1870–1878.
166 M. Zhu, Y.-J. Gao, X.-L. Huang, M. Li, C. Zheng and S.-L. You, *Nat. Commun.*, 2024, **15**, 2462.
167 C.-X. Lu, G.-P. Zhan, K. Chen, Z.-K. Liu and C.-D. Wu, *Appl. Catal., B*, 2020, **279**, 119350.
168 X. Yang, T. Liang, J. Sun, M. J. Zaworotko, Y. Chen, P. Cheng and Z. Zhang, *ACS Catal.*, 2019, **9**, 7486–7493.
169 P. M. Stanley, K. Hemmer, M. Hegelmann, A. Schulz, M. Park, M. Elsner, M. Cokoja and J. Warnan, *Chem. Sci.*, 2022, **13**, 12164–12174.
170 P. M. Stanley, A. Y. Su, V. Ramm, P. Fink, C. Kimna, O. Lieleg, M. Elsner, J. A. Lercher, B. Rieger, J. Warnan and R. A. Fischer, *ACS Catal.*, 2021, **11**, 871–882.
171 H. Liu, Q.-Q. Li, L. Zhou, B. Deng, P.-H. Pan, S.-Y. Zhao, P. Liu, Y.-Y. Wang and J.-L. Li, *J. Am. Chem. Soc.*, 2023, **145**, 17588–17596.
172 T. Goh, C.-K. Tsung and W. Huang, *ACS Appl. Mater. Interfaces*, 2019, **11**, 23254–23260.
173 D. Sun, M. Xu, Y. Jiang, J. Long and Z. Li, *Small Methods*, 2018, **2**, 1800164.
174 Y.-H. Zhu, J.-B. Yang, X.-M. Liu, J.-L. Wang, Q.-D. Ping, Z.-Y. Du, J.-N. Li, T.-T. Zang, H. Mei and Y. Xu, *Dalton Trans.*, 2022, **51**, 3502–3511.
175 Z. Fang, Z. Deng, X. Wan, Z. Li, X. Ma, S. Hussain, Z. Ye and X. Peng, *Appl. Catal., B*, 2021, **296**, 120329.
176 Z.-X. Sun, K. Sun, M.-L. Gao, O. Metin and H.-L. Jiang, *Angew. Chem., Int. Ed.*, 2022, **61**, e202206108.
177 M. Mukoyoshi and H. Kitagawa, *Chem. Commun.*, 2022, **58**, 10757–10767.
178 J. Guo, Y. Wan, Y. Zhu, M. Zhao and Z. Tang, *Nano Res.*, 2021, **14**, 2037–2052.
179 Y. Liu, Z. Liu, D. Huang, M. Cheng, G. Zeng, C. Lai, C. Zhang, C. Zhou, W. Wang, D. Jiang, H. Wang and B. Shao, *Coord. Chem. Rev.*, 2019, **388**, 63–78.
180 K. Kusada and H. Kitagawa, *Adv. Mater.*, 2016, **28**, 1129–1142.
181 X. Fang, Q. Shang, Y. Wang, L. Jiao, T. Yao, Y. Li, Q. Zhang, Y. Luo and H.-L. Jiang, *Adv. Mater.*, 2018, **30**, 1705112.
182 J.-D. Xiao, L. Han, J. Luo, S.-H. Yu and H.-L. Jiang, *Angew. Chem., Int. Ed.*, 2018, **57**, 1103–1107.
183 S. Dai, A. Tissot and C. Serre, *Adv. Energy Mater.*, 2022, **12**, 2100061.
184 S. Dai, K. P. Ngoc, L. Grimaud, S. Zhang, A. Tissot and C. Serre, *J. Mater. Chem. A*, 2022, **10**, 3201–3205.
185 S. Dai, T. Kajiwara, M. Ikeda, I. Romero-Muñiz, G. Patriarche, A. E. Platero-Prats, A. Vimont, M. Daturi, A. Tissot, Q. Xu and C. Serre, *Angew. Chem., Int. Ed.*, 2022, **61**, e202211848.
186 S. Wang, M. Cabrero-Antonino, S. Navalón, C.-C. Cao, A. Tissot, I. Dovgaliuk, J. Marrot, C. Martineau-Corcos, L. Yu, H. Wang, W. Shepard, H. García and C. Serre, *Chem*, 2020, **6**, 3409–3427.
187 M. Chen, C. R. Bowers and W. Huang, *Acc. Mater. Res.*, 2021, **2**, 1190–1202.
188 C. H. Mejia, T. W. van Deelen and K. P. de Jong, *Nat. Commun.*, 2018, **9**, 4459.
189 A. Aijaz, A. Karkamkar, Y. J. Choi, N. Tsumori, E. Roennebro, T. Autrey, H. Shioyama and Q. Xu, *J. Am. Chem. Soc.*, 2012, **134**, 13926–13929.
190 S. Linic, U. Aslam, C. Boerigter and M. Morabito, *Nat. Mater.*, 2015, **14**, 567–576.
191 L. Wang, S.-R. Li, Y.-Z. Chen and H.-L. Jiang, *Small*, 2021, **17**, 2004481.
192 A. Fujishima and K. Honda, *Nature*, 1972, **238**, 37–38.
193 S. Kohtani, A. Kawashima and H. Miyabe, *Front. Chem.*, 2019, **7**, 630.
194 Q. Lei, S. Yang, D. Ding, J. Tan, J. Liu and R. Chen, *J. Mater. Chem. A*, 2021, **9**, 2491–2525.
195 B. Weng, M.-Y. Qi, C. Han, Z.-R. Tang and Y.-J. Xu, *ACS Catal.*, 2019, **9**, 4642–4687.
196 L. Giri, S. R. Rout, R. S. Varma, M. Otyepka, K. Jayaramulu and R. Dandela, *Nanotechnol. Rev.*, 2022, **11**, 1947–1976.
197 S. Subudhi, S. P. Tripathy and K. Parida, *Inorg. Chem. Front.*, 2021, **8**, 1619–1636.
198 C.-C. Wang, X. Wang and W. Liu, *Chem. Eng. J.*, 2020, **391**, 123601.
199 C. Zhao, X. Pan, Z. Wang and C.-C. Wang, *Chem. Eng. J.*, 2021, **417**, 128022.
200 B. Deng, Q. Chen, Y. Liu, A. U. Khan, D. Zhang, T. Jiang, X. Wang, N. Liu, H. Li and B. Mao, *J. Colloid Interface Sci.*, 2024, **662**, 1016–1025.
201 J.-Y. Li, Y.-H. Li, M.-Y. Qi, Q. Lin, Z.-R. Tang and Y.-J. Xu, *ACS Catal.*, 2020, **10**, 6262–6280.

202 X. Ning and G. Lu, *Nanoscale*, 2020, **12**, 1213–1223.
203 R. Shen, D. Ren, Y. Ding, Y. Guan, Y. H. Ng, P. Zhang and X. Li, *Sci. China Mater.*, 2020, **63**, 2153–2188.
204 R. Wu, S. Wang, Y. Zhou, J. Long, F. Dong and W. Zhang, *ACS Appl. Nano Mater.*, 2019, **2**, 6818–6827.
205 X. Chu, C. I. Sathish, J.-H. Yang, X. Guan, X. Zhang, L. Qiao, K. Domen, S. Wang, A. Vinu and J. Yi, *Small*, 2023, **19**, 2302875.
206 A. Deng, Y. Sun, Z. Gao, S. Yang, Y. Liu, H. He, J. Zhang, S. Liu, H. Sun and S. Wang, *Nano Energy*, 2023, **108**, 108228.
207 A. Meng, Z. Teng, Q. Zhang and C. Su, *Chem. – Asian J.*, 2020, **15**, 3405–3415.
208 S. Wang, J. Zhang, B. Li, H. Sun, S. Wang and X. Duan, *J. Environ. Chem. Eng.*, 2022, **10**, 107438.
209 A. Anus and S. Park, *Chem. Eng. J.*, 2024, **486**, 150213.
210 Z. Durmus and A. W. Maijenburg, *Int. J. Hydrogen Energy*, 2022, **47**, 36784–36813.
211 J.-J. Jiang, F.-J. Zhang and Y.-R. Wang, *New J. Chem.*, 2023, **47**, 1599–1609.
212 M. Usman, Z. Zeb, H. Ullah, M. H. Suliman, M. Humayun, L. Ullah, S. N. A. Shah, U. Ahmed and M. Saeed, *J. Environ. Chem. Eng.*, 2022, **10**, 107548.
213 D.-E. Lee, M. Danish, U. Alam and W.-K. Jo, *J. Energy Chem.*, 2024, **92**, 322–356.
214 J. Liu, Q. Li, X. Xiao, F. Li, C. Zhao, Q. Sun, P. Qiao, J. Zhou, J. Wu, B. Li, H. Bao and B. Jiang, *J. Colloid Interface Sci.*, 2021, **590**, 1–11.
215 S. Daliran, M. Khajeh, A. R. Oveisi, J. Albero and H. Garcia, *ACS Appl. Mater. Interfaces*, 2022, **14**, 36515–36526.
216 N. Fernandes, C. F. Rodrigues, A. F. Moreira and I. J. Correia, *Biomater. Sci.*, 2020, **8**, 2990–3020.
217 C. Yan, Q. Tian and S. Yang, *RSC Adv.*, 2017, **7**, 37887–37897.
218 F. Wang, Y. Huang, Z. Chai, M. Zeng, Q. Li, Y. Wang and D. Xu, *Chem. Sci.*, 2016, **7**, 6887–6893.
219 Y.-N. Gong, X. Guan and H.-L. Jiang, *Coord. Chem. Rev.*, 2023, **475**, 214889.
220 T. He and Y. Zhao, *Angew. Chem., Int. Ed.*, 2023, **62**, e202303086.
221 A. Lopez-Magano, S. Daliran, A. R. Oveisi, R. Mas-Balleste, A. Dhakshinamoorthy, J. Aleman, H. Garcia and R. Luque, *Adv. Mater.*, 2023, **35**, 2209475.
222 S.-P. Qi, R.-T. Guo, Z.-X. Bi, Z.-R. Zhang, C.-F. Li and W.-G. Pan, *Small*, 2023, **19**, 2303632.
223 C. Xia, K. O. Kirlikovali, N. Thi Hong Chuong, N. Xuan Cuong, T. Quoc Ba, D. Minh Khoa, D. Minh Tuan Nguyen, N. Dang Le Tri, P. Singh, P. Raizada, N. Van-Huy, S. Y. Kim, L. Singh, C. C. Nguyen, M. Shokouhimehr and Q. V. Le, *Coord. Chem. Rev.*, 2021, **446**, 214117.
224 L. Yang, J. Wang, K. Zhao, Z. Fang, H. Qiao, L. Zhai and L. Mi, *ChemPlusChem*, 2022, **87**, e202200281.
225 G. Yuan, L. Tan, P. Wang, Y. Wang, C. Wang, H. Yan and Y.-Y. Wang, *Cryst. Growth Des.*, 2022, **22**, 893–908.
226 Y. Deng, Y. Wang, X. Xiao, B. J. Saucedo, Z. Zhu, M. Xie, X. Xu, K. Yao, Y. Zhai, Z. Zhang and J. Chen, *Small*, 2022, **18**, 2202928.
227 S. Xun, H. Li, G. Sini and J. L. Bredas, *Chem. - Asian J.*, 2021, **16**, 3781–3789.
228 G. Lu, X. Huang, Y. Li, G. Zhao, G. Pang and G. Wang, *J. Energy Chem.*, 2020, **43**, 8–15.
229 M.-Y. Zhang, J.-K. Li, R. Wang, S.-N. Zhao, S.-Q. Zang and T. C. W. Mak, *Adv. Sci.*, 2021, **8**, 2101884.
230 M.-L. Gao, M.-H. Qi, L. Liu and Z.-B. Han, *Chem. Commun.*, 2019, **55**, 6377–6380.
231 L. Wang, J. Mao, G. Huang, Y. Zhang, J. Huang, H. She, C. Liu, H. Liu and Q. Wang, *Chem. Eng. J.*, 2022, **446**, 137011.
232 Z. Wu, W. Li, L. Hou, Q. Wei, H. Yang, Y. Jiang and D. Tang, *Sep. Purif. Technol.*, 2023, **311**, 123322.
233 Q. Yang, Y. Zhang, N. Ding, Q. Hu, X. Yan, J. Liu, P. Zhang, S. Fu, Q. Wang, L. Wu and S. Wu, *Appl. Organomet. Chem.*, 2022, **36**, e6775.
234 S. Oudi, A. R. Oveisi, S. Daliran, M. Khajeh, R. Luque, U. Sen and H. Garcia, *Appl. Catal., A*, 2021, **611**, 117965.
235 C. Si, X. Liu, T. Zhang, J. Xu, J. Li, J. Fu and Q. Han, *Inorg. Chem.*, 2023, **62**, 4210–4219.
236 X.-Z. Wei, F. W. Dagnaw, J. Liu and L. Ma, *J. Colloid Interface Sci.*, 2023, **629**, 136–143.
237 C. Xu, H. Liu, D. Li, J.-H. Su and H.-L. Jiang, *Chem. Sci.*, 2018, **9**, 3152–3158.
238 W. Sheng, F. Huang, X. Dong and X. Lang, *J. Colloid Interface Sci.*, 2022, **628**, 784–793.
239 G.-C. Guo, J.-P. Zhao, S. Guo, W.-X. Shi, F.-C. Liu, T.-B. Lu and Z.-M. Zhang, *Angew. Chem., Int. Ed.*, 2024, **63**, e202402374.
240 W. Sheng, H. Hao, F. Huang, F. Zhang and X. Lang, *Chem. Eng. J.*, 2022, **430**, 133071.
241 W. Sheng, X. Wang, Y. Wang, S. Chen and X. Lang, *ACS Catal.*, 2022, **12**, 11078–11088.
242 L. Wang, D. Shen, H. Zhang, B. Mo, J. Wu and H. Hou, *Chem. – Eur. J.*, 2022, **28**, e202103466.
243 Y.-L. Chong, D.-D. Zhao, M. Yan, J.-J. Zhang, B. Wang, Z. Chen and J.-L. Zhuang, *J. Catal.*, 2024, **431**, 115395.
244 P. Tamuly and J. N. Moorthy, *ACS Appl. Mater. Interfaces*, 2024, **16**, 3348–3358.
245 Y. Wang, L. Zhao, S. Liu, G. Ji, C. He, Y. Tang and C. Duan, *ACS Appl. Mater. Interfaces*, 2023, **15**, 16744–16754.
246 G. Ji, L. Zhao, Y. Wang, Y. Tang, C. He, S. Liu and C. Duan, *ACS Catal.*, 2022, **12**, 7821–7832.
247 H. Jiang, H. Cheng, C. Zang, J. Tan, B. Sun and F. Bian, *J. Catal.*, 2021, **401**, 279–287.
248 L. Hou, X. Jing, H. Huang and C. Duan, *J. Mater. Chem. A*, 2022, **10**, 24320–24330.
249 H.-G. Jin, J.-X. Gu, W. Lin, W.-J. Xu, B.-X. Huang, F. Yang, J.-X. Wen, Y. Ren and Z.-S. Chao, *Microporous Mesoporous Mater.*, 2022, **346**, 112257.
250 Y. Zhang, W. Zhang, F. Zhang, Y. Xiao, G. Jia, W. Wang, F.-S. Ke and Z. Guo, *Angew. Chem., Int. Ed.*, 2024, **63**, e202402694.
251 C. Li, H. Zhang, X. Wang, Q.-Y. Li, X. Zhao and X.-J. Wang, *RSC Adv.*, 2022, **12**, 1638–1644.
252 M. Li, X. Liu, Y. Che, H. Xing, F. Sun, W. Zhou and G. Zhu, *Angew. Chem., Int. Ed.*, 2023, **62**, e202308651.
253 P. Chen, Z. Guo, X. Liu, H. Lv, Y. Che, R. Bai, Y. Chi and H. Xing, *J. Mater. Chem. A*, 2019, **7**, 27074–27080.

254 A. K. Kar, A. Behera and R. Srivastava, *ACS Appl. Nano Mater.*, 2022, **5**, 464–475.
255 L. Zeng, T. Zhang, R. Liu, W. Tian, K. Wu, J. Zhu, Z. Wang, C. He, J. Feng, X. Guo, A. I. Douka and C. Duan, *Nat. Commun.*, 2023, **14**, 4002.
256 H. Cheng, C. Zang, F. Bian, Y. Jiang, L. Yang, F. Dong and H. Jiang, *Catal. Sci. Technol.*, 2021, **11**, 5543–5552.
257 Y.-Y. Zhu, G. Lan, Y. Fan, S. S. Veroneau, Y. Song, D. Micheroni and W. Lin, *Angew. Chem., Int. Ed.*, 2018, **57**, 14090–14094.
258 S. A. A. Razavi, A. Morsali and M. Piroozzadeh, *Inorg. Chem.*, 2022, **61**, 19134–19143.
259 Z. Soleimani, Y. Absalan, M. Gholizadeh, M. Asadinamin, A. N. Utenishev, R. Galeev and K. Souri, *ACS Appl. Energy Mater.*, 2024, **7**, 3787–3805.
260 L. Feng, Y. Wang, S. Yuan, K.-Y. Wang, J.-L. Li, G. S. Day, D. Qiu, L. Cheng, W.-M. Chen, S. T. Madrahimov and H.-C. Zhou, *ACS Catal.*, 2019, **9**, 5111–5118.
261 M. R. Ghaleno, M. Ghaffari-Moghaddam, M. Khajeh, A. R. Oveisi and M. Bohlooli, *J. Colloid Interface Sci.*, 2019, **535**, 214–226.
262 X.-C. Lin, Y.-M. Wang, X. Chen, P.-Y. You, K.-M. Mo, G.-H. Ning and D. Li, *Angew. Chem., Int. Ed.*, 2023, **62**, e202306497.
263 H. Liu, C. Xu, D. Li and H.-L. Jiang, *Angew. Chem., Int. Ed.*, 2018, **57**, 5379–5383.
264 M. Klarner, S. Hammon, S. Feulner, S. Kuemmel, L. Kador and R. Kempe, *ChemCatChem*, 2020, **12**, 4593–4599.
265 P. Li, X. Yan, S. Gao and R. Cao, *Chem. Eng. J.*, 2021, **421**, 129870.
266 M. Hao, Y. Qin, J. Shen, B. Wang and Z. Li, *ACS Catal.*, 2022, **12**, 15282–15287.
267 X. Gong, Y. Shu, Z. Jiang, L. Lu, X. Xu, C. Wang and H. Deng, *Angew. Chem., Int. Ed.*, 2020, **59**, 5326–5331.
268 H. Li, Y. Yang, X. Jing, C. He and C. Duan, *Chem. – Asian J.*, 2021, **16**, 1237–1244.
269 D. Tilgner, M. Klarner, S. Hammon, M. Friedrich, A. Verch, N. de Jonge, S. Kuemmel and R. Kempe, *Aust. J. Chem.*, 2019, **72**, 842–847.
270 X. Deng, Y. Qin, M. Hao and Z. Li, *Inorg. Chem.*, 2019, **58**, 16574–16580.
271 J. Aleman and R. Mas-Balleste, *Front. Chem.*, 2021, **9**, 708312.
272 S. Boochakiat, B. Inceesungvorn, A. Nattestad and J. Chen, *ChemNanoMat*, 2023, **9**, e202300140.
273 K. Wu, X.-Y. Liu, P.-W. Cheng, M. Xie, W. Lu and D. Li, *Sci. China: Chem.*, 2023, **66**, 1634–1653.
274 X. Wang, X. Zhang, P. Li, K.-I. Otake, Y. Cui, J. Lyu, M. D. Krzyaniak, Y. Zhang, Z. Li, J. Liu, C. T. Buru, T. Islamoglu, M. R. Wasielewski, Z. Li and O. K. Farha, *J. Am. Chem. Soc.*, 2019, **141**, 8306–8314.
275 B. Wu, L. Zhang, B. Jiang, Q. Li, C. Tian, Y. Xie, W. Li and H. Fu, *Angew. Chem., Int. Ed.*, 2021, **60**, 4815–4822.
276 A. Santiago-Portillo, M. Cabrero-Antonino, M. Alvaro, S. Navalon and H. Garcia, *Chem. – Eur. J.*, 2019, **25**, 9280–9286.
277 K. Cerdan, W. Ouyang, J. C. Colmenares, M. J. Munoz-Batista, R. Luque and A. M. Balu, *Chem. Eng. Sci.*, 2019, **194**, 78–84.
278 G. An, X. Zhang, C. Zhang, H. Gao, S. Liu, G. Qin, H. Qi, J. Kasemchainan, J. Zhang and G. Wang, *Chin. J. Catal.*, 2023, **50**, 126–174.
279 S. Kim, J. Lee, S. Jeoung, H. R. Moon and M. Kim, *Chem. – Eur. J.*, 2020, **26**, 7568–7572.
280 S. M. Hosseini, H. Dehghan and V. Safarifard, *Polyhedron*, 2022, **212**, 115581.
281 D. Xie, S. Li, W. Yang, S. Fan and Y.-S. Feng, *ChemistrySelect*, 2022, **7**, e202103521.
282 G. Kumar, G. Bhargava, S. Kumar, J. K. Rajput, B. Singh, P. Singh and R. Kumar, *Inorg. Chim. Acta*, 2024, **563**, 121935.
283 H. Alamgholiloo, S. Rostamnia, A. Hassankhani, X. Liu, A. Eftekhari, A. Hasanzadeh, K. Zhang, H. Karimi-Maleh, S. Khaksar, R. S. Varma and M. Shokouhimehr, *J. Colloid Interface Sci.*, 2020, **567**, 126–135.
284 X. Li, F. Zhang, M. Zhang, Z. Zhou and X. Zhou, *J. Energy Storage*, 2023, **59**, 106473.
285 H. Yang, F. Peng, A. N. Hong, Y. Wang, X. Bu and P. Feng, *J. Am. Chem. Soc.*, 2021, **143**, 14470–14474.
286 F. Yu, B.-Q. Hu, X.-N. Wang, Y.-M. Zhao, J.-L. Li, B. Li and H.-C. Zhou, *J. Mater. Chem. A*, 2020, **8**, 2083–2089.
287 X. Chen, M. Zhang, H. Qin, J. Zhou, Q. Shen, K. Wang, W. Chen, M. Liu and N. Li, *Sep. Purif. Technol.*, 2022, **280**, 119751.
288 H. He, Y. Li, J. Wang, J. Wu, L. Sun, Y. Cai, H. Cheng and X. Wang, *Chem. Eng. J.*, 2022, **450**, 138141.
289 J. Lin, W. Tian, Z. Guan, H. Zhang, X. Duan, H. Wang, H. Sun, Y. Fang, Y. Huang and S. Wang, *Adv. Funct. Mater.*, 2022, **32**, 2201743.
290 X. Wu, T. Liu, W. Ni, H. Yang, H. Huang, S. He, C. Li, H. Ning, W. Wu, Q. Zhao and M. Wu, *J. Colloid Interface Sci.*, 2022, **623**, 9–20.
291 X. Wu, Q. Zhao, J. Zhang, S. Li, H. Liu, K. Liu, Y. Li, D. Kong, H. Sun and M. Wu, *J. Colloid Interface Sci.*, 2023, **634**, 972–982.
292 W. Xu, W. Xue, H. Huang, J. Wang, C. Zhong and D. Mei, *Appl. Catal., B*, 2021, **291**, 120129.
293 D. Dissanayake, L. A. Achola, P. Kerns, D. Rathnayake, J. He, J. Macharia and S. L. Suib, *Appl. Catal., B*, 2019, **249**, 32–41.
294 J. Li, R. Hu, W. Liu, D. Gao, H. Zhao, C. Li, X. Jiang and G. Chen, *Inorg. Chem.*, 2023, **62**, 3692–3702.
295 G. Liu, S. Liu, Z. Li, H. Chen, J. Li, Y. Zhang, G. Shen, B. Yang, X. Hu and X. Huang, *RSC Adv.*, 2021, **12**, 118–122.
296 C. Wu, J. Bu, W. Wang, H. Shen, Y. Cao and H. Zhang, *Ind. Eng. Chem. Res.*, 2022, **61**, 5442–5452.
297 R. An, M. Gu, Y. Zang, H. Xu, Z. Hou and C. Guo, *Curr. Org. Chem.*, 2020, **24**, 1897–1942.
298 H. Wang, J. Yu, S. Wei, M. Lin, Y. Song and L. Wu, *Chem. Eng. J.*, 2022, **441**, 136020.
299 L. M. Aguirre-Diaz, N. Snejko, M. Iglesias, F. Sanchez, E. Gutierrez-Puebla and M. Angeles Monge, *Inorg. Chem.*, 2018, **57**, 6883–6892.

300 S. Z. Anbardan, J. Mokhtari, A. Yari and A. H. Bozcheloei, *RSC Adv.*, 2021, **11**, 20788–20793.
301 K. Gao, H. Li, Q. Meng, J. Wu and H. Hou, *ACS Appl. Mater. Interfaces*, 2021, **13**, 2779–2787.
302 H. Liu, Z. Guo, H. Lv, X. Liu, Y. Che, Y. Mei, R. Bai, Y. Chi and H. Xing, *Inorg. Chem. Front.*, 2020, **7**, 1016–1025.
303 Z. Liu, C. Li, J. Chen, X. Li, F. Luo, F. Cheng and J.-J. Liu, *Inorg. Chem. Front.*, 2022, **9**, 111–118.
304 R. Shang, Q. Zhang, P. Lin, B. Gu, Q. Tang, Q. Cao and W. Fang, *Appl. Catal., B*, 2022, **319**, 121904.
305 S. Wang, K. Gao, Y. Cui, S. Li, H. Zhang, B. Zhang, J. Wu, H. Hou and S. Zang, *Nano Res.*, 2023, **16**, 4715–4722.
306 Y.-X. Wang, H.-M. Wang, P. Meng, D.-X. Song, Z. Qi and X.-M. Zhang, *Chin. J. Chem.*, 2021, **39**, 2983–2989.
307 K. Zhang, Z. Xi, Z. Wu, G. Lu and X. Huang, *ACS Sustainable Chem. Eng.*, 2021, **9**, 12623–12633.
308 F.-J. Zhao, G. Zhang, Z. Ju, Y.-X. Tan and D. Yuan, *Inorg. Chem.*, 2020, **59**, 3297–3303.
309 B. Zeng, Y. Wang, F. Huang, K. Xiong, K. Zhang and X. Lang, *Catal. Sci. Technol.*, 2024, **14**, 2838–2847.
310 X. B. Liu, Q. Rong, J. Tan, C. Chen and Y. L. Hu, *Front. Chem.*, 2022, **9**, 798603.
311 E. Skolia, P. L. Gkizis and C. G. Kokotos, *ChemPlusChem*, 2022, **87**, e202200008.
312 S. Wolfe and C. F. Ingold, *J. Am. Chem. Soc.*, 1983, **105**, 7755–7757.
313 X.-F. Li, P. Wu, L. Kan, Q. Niu, S.-N. Sun, Q. Huang and Y.-Q. Lan, *Adv. Funct. Mater.*, 2023, **33**, 2308534.
314 Y. Li, F. Gao, J. Xue, G.-P. Yang and Y.-Y. Wang, *Cryst. Growth Des.*, 2023, **23**, 3702–3710.
315 P. Patel, B. Parmar, R. I. Kureshy, N.-U. H. Khan and E. Suresh, *Dalton Trans.*, 2018, **47**, 8041–8051.
316 L.-Q. Wei and B.-H. Ye, *ACS Appl. Mater. Interfaces*, 2019, **11**, 41448–41457.
317 B. Zeng, W. Sheng, F. Huang, K. Zhang, K. Xiong and X. Lang, *Chem. Eng. J.*, 2023, **474**, 145559.
318 Z. Zhao, M. Liu, K. Zhou, L. Guo, Y. Shen, D. Lu, X. Hong, Z. Bao, Q. Yang, Q. Ren, P. R. Schreiner and Z. Zhang, *ACS Appl. Mater. Interfaces*, 2023, **15**, 6982–6989.
319 J.-Q. Chen, K.-Y. Zhang, X.-D. Zhang, Z.-Q. Huang, H. Deng, Y. Zhao, Z.-Z. Shi and W.-Y. Sun, *Chem. – Eur. J.*, 2024, **30**, e202303725.
320 Z. Zhao, M. Liu, K. Zhou, L. Guo, Y. Shen, D. Lu, X. Hong, Z. Bao, Q. Yang, Q. Ren, P. R. Schreiner and Z. Zhang, *ACS Appl. Mater. Interfaces*, 2023, **15**, 6982–6989.
321 Y. Wang, Z. Zhang, J. Li, Y. Yuan, J. Yang, W. Xu, P. An, S. Xi, J. Guo, B. Liu and J. Li, *Angew. Chem., Int. Ed.*, 2022, **61**, e202211031.
322 T. He, B. Ni, S. Zhang, Y. Gong, H. Wang, L. Gu, J. Zhuang, W. Hu and X. Wang, *Small*, 2018, **14**, 1703929.
323 Y. Pan, R. Abazari, J. Yao and J. Gao, *J. Phys. Energy*, 2021, **3**, 032010.
324 Y. Pan, X. Yuan, L. Jiang, H. Yu, J. Zhang, H. Wang, R. Guan and G. Zeng, *Chem. Eng. J.*, 2018, **354**, 407–431.
325 V. Soni, P. Raizada, A. Kumar, V. Hasija, S. Singal, P. Singh, A. Hosseini-Bandegharaei, V. K. Thakur and N. Van-Huy, *Environ. Chem. Lett.*, 2021, **19**, 1065–1095.
326 R. Yang, L. Mei, Y. Fan, Q. Zhang, R. Zhu, R. Amal, Z. Yin and Z. Zeng, *Small Methods*, 2021, **5**, 2100887.
327 G. Zhang, H. Wu, D. Chen, N. Li, Q. Xu, H. Li, J. He and J. Lu, *Green Energy Environ.*, 2022, **7**, 176–204.
328 F. Babawale, K. Murugesan, R. Narobe and B. Koenig, *Org. Lett.*, 2022, **24**, 4793–4797.
329 K. He, P. Li, S. Zhang, Q. Chen, H. Ji, Y. Yuan and X. Jia, *Chem. Commun.*, 2018, **54**, 13232–13235.
330 R.-X. Jin, J.-C. Dai, Y. Li and X.-S. Wang, *Org. Lett.*, 2021, **23**, 421–426.
331 R. R. Karimov and J. F. Hartwig, *Angew. Chem., Int. Ed.*, 2018, **57**, 4234–4241.
332 Y. Yuan, S. Zhang, Z. Sun, Y. Su, Q. Ma, Y. Yuan and X. Jia, *Chem. Commun.*, 2021, **57**, 3347–3350.
333 Q. Zhang, B. An, Y. Lei, Z. Gao, H. Zhang, S. Xue, X. Jin, W. Xu, Z. Wu, M. Wu, X. Yang and W. Wu, *Angew. Chem., Int. Ed.*, 2023, **62**, e202304699.
334 G. Ji, L. Zhao, Y. Tang, S. Liu, Y. Wang, C. He and C. Duan, *Small*, 2023, **19**, 2300597.
335 Y. Wang, L. Zhao, G. Ji, C. He, S. Liu and C. Duan, *ACS Appl. Mater. Interfaces*, 2022, **14**, 2794–2804.
336 G. Laudadio, S. Govaerts, Y. Wang, D. Ravelli, H. F. Koolman, M. Fagnoni, S. W. Djuric and T. Noel, *Angew. Chem., Int. Ed.*, 2018, **57**, 4078–4082.
337 Z.-J. Bai, S. Tian, T.-Q. Zeng, L. Chen, B.-H. Wang, B. Hu, X. Wang, W. Zhou, J.-B. Pan, S. Shen, J.-K. Guo, T.-L. Xie, Y.-J. Li, C.-T. Au and S.-F. Yin, *ACS Catal.*, 2022, **12**, 15157–15167.
338 J. Li, B. Ren, X. Yan, P. Li, S. Gao and R. Cao, *J. Catal.*, 2021, **395**, 227–235.
339 H. Han, X. Zheng, C. Qiao, Z. Xia, Q. Yang, L. Di, Y. Xing, G. Xie, C. Zhou, W. Wang and S. Chen, *ACS Catal.*, 2022, **12**, 10668–10679.
340 L. Zhao, W. Cai, G. Ji, J. Wei, Z. Du, C. He and C. Duan, *Inorg. Chem.*, 2022, **61**, 9493–9503.
341 J. Liu, G. S. Cremosnik, F. Otte, A. Pahl, S. Sievers, C. Strohmann and H. Waldmann, *Angew. Chem., Int. Ed.*, 2021, **60**, 4648–4656.
342 A. M. Nauth, E. Schechtel, R. Dören, W. Tremel and T. Opatz, *J. Am. Chem. Soc.*, 2018, **140**, 14169–14177.
343 S. Shirase, S. Tamaki, K. Shinohara, K. Hirosawa, H. Tsurugi, T. Satoh and K. Mashima, *J. Am. Chem. Soc.*, 2020, **142**, 5668–5675.
344 W. T. Chung, I. M. A. Mekhemer, M. G. Mohamed, A. M. Elewa, A. F. M. El-Mahdy, H.-H. Chou, S.-W. Kuo and K. C. W. Wu, *Coord. Chem. Rev.*, 2023, **483**, 215066.
345 M. Guo, M. Zhang, R. Liu, X. Zhang and G. Li, *Adv. Sci.*, 2022, **9**, 2103361.
346 S. Liu, C. Zhang, Y. Sun, Q. Chen, L. He, K. Zhang, J. Zhang, B. Liu and L.-F. Chen, *Coord. Chem. Rev.*, 2020, **413**, 213266.
347 D. A. Reddy, Y. Kim, M. Gopannagari, D. P. Kumar and T. K. Kim, *Sustainable Energy Fuels*, 2021, **5**, 1597–1618.
348 H.-L. Tang, X.-J. Sun and F.-M. Zhang, *Dalton Trans.*, 2020, **49**, 12136–12144.
349 I. I. Alkhatib, C. Garlisi, M. Pagliaro, K. Al-Ali and G. Palmisano, *Catal. Today*, 2020, **340**, 209–224.

350 M. Dong, J.-X. Gu, C.-Y. Sun, X.-L. Wang and Z.-M. Su, *Chem. Commun.*, 2022, **58**, 10114–10126.
351 Z. Fang, X. Yue, F. Li and Q. Xiang, *Chem. – Eur. J.*, 2023, **29**, e202203706.
352 K. Guo, I. Hussain, G. A. Jie, Y. Fu, F. Zhang and W. Zhu, *J. Environ. Sci.*, 2023, **125**, 290–308.
353 K.-G. Liu, F. Bigdeli, A. Panjehpour, A. Larimi, A. Morsali, A. Dhakshinamoorthy and H. Garcia, *Coord. Chem. Rev.*, 2023, **493**, 215257.
354 K. Hu, Z. Huang, L. Zeng, Z. Zhang, L. Mei, Z. Chai and W. Shi, *Eur. J. Inorg. Chem.*, 2022, e202100748.
355 J. Pan, B. Xiao, W. Zhu, Y. Yang, H. Huang, Z. Lian, T. Zhang, F. Qiu, S. Xue and H. Pang, *Nano Res.*, 2024, **17**, 6713–6720.
356 J. Song, Z.-F. Huang, L. Pan, K. Li, X. Zhang, L. Wang and J.-J. Zou, *Appl. Catal., B*, 2018, **227**, 386–408.
357 H. Liu, Q. Mei, Q. Xu, J. Song, H. Liu and B. Han, *Green Chem.*, 2017, **19**, 196–201.
358 M. Cybularczyk-Cecotka, J. Szczepanik and M. Giedyk, *Nat. Catal.*, 2020, **3**, 872–886.
359 K. Tamao, K. Sumitani and M. Kumada, *J. Am. Chem. Soc.*, 1972, **94**, 4374–4376.
360 Z. Guo, X. Liu, R. Bai, Y. Che, Y. Chi, C. Guo and H. Xing, *Inorg. Chem.*, 2021, **60**, 8672–8681.
361 T. Luo, L. Li, Y. Chen, J. An, C. Liu, Z. Yan, J. H. Carter, X. Han, A. M. Sheveleva, F. Tuna, E. J. L. McInnes, C. C. Tang, M. Schröder and S. Yang, *Nat. Commun.*, 2021, **12**, 3583.
362 S. Bhatt, R. S. Das, A. Kumar, A. Malik, A. Soni and S. L. Jain, *Catal. Sci. Technol.*, 2022, **12**, 6805–6818.
363 Y. Che, X. Liu, M. Li, X. Liu, M. Wang, Q. Song and H. Xing, *Appl. Surf. Sci.*, 2023, **634**, 157699.
364 X. Liu, Z. Guo, Y. Che, M. Li, X. Liu, F. Cui and H. Xing, *J. Mater. Chem. A*, 2024, **12**, 2200–2208.
365 Y.-X. Tan, S.-X. Lin, C. Liu, Y. Huang, M. Zhou, Q. Kang, D. Yuan and M. Hong, *Appl. Catal., B*, 2018, **227**, 425–432.
366 Q. Xia, J. Dong, H. Song and Q. Wang, *Chem. – Eur. J.*, 2019, **25**, 2949–2961.
367 S. M. Khake, V. Soni, R. G. Gonnade and B. Punji, *Dalton Trans.*, 2014, **43**, 16084–16096.
368 C. M. McMahon and E. J. Alexanian, *Angew. Chem., Int. Ed.*, 2014, **53**, 5974–5977.
369 I. P. Beletskaya and V. P. Ananikov, *Chem. Rev.*, 2011, **111**, 1596–1636.
370 M. Jiang, H. Li, H. Yang and H. Fu, *Angew. Chem., Int. Ed.*, 2017, **56**, 874–879.
371 N. A. Patil, J. Tailhades, R. A. Hughes, F. Separovic, J. D. Wade and M. A. Hossain, *Int. J. Mol. Sci.*, 2015, **16**, 1791–1805.
372 R. Jin, D. Zheng, R. Liu and G. Liu, *ChemCatChem*, 2018, **10**, 1739–1752.
373 T. F. Qahtan, T. O. Owolabi, O. E. Olubi and A. Hezam, *Coord. Chem. Rev.*, 2023, **492**, 215276.
374 X. Yang, S. J. Kalita, S. Maheshuni and Y.-Y. Huang, *Coord. Chem. Rev.*, 2019, **392**, 35–48.
375 Z. Yin, S. Wan, J. Yang, M. Kurmoo and M.-H. Zeng, *Coord. Chem. Rev.*, 2019, **378**, 500–512.
376 W. Zheng, X. Yang, Z. Li, B. Yang, Q. Zhang, L. Lei and Y. Hou, *Angew. Chem., Int. Ed.*, 2023, **62**, e202307283.
377 M. Hao and Z. Li, *Sol. RRL*, 2021, **5**, 2000454.
378 W. Shi, Y. Quan, G. Lan, K. Ni, Y. Song, X. Jiang, C. Wang and W. Lin, *J. Am. Chem. Soc.*, 2021, **143**, 16718–16724.
379 S. Daliran, M. Khajeh, A. R. Oveisi, H. Garcia and R. Luque, *ACS Sustainable Chem. Eng.*, 2022, **10**, 5315–5322.
380 D. Wang, Y. Pan, L. Xu and Z. Li, *J. Catal.*, 2018, **361**, 248–254.
381 S. Daliran, M. Khajeh, A. R. Oveisi, J. Albero and H. Garcia, *ACS Appl. Mater. Interfaces*, 2022, **14**, 36515–36526.
382 A. Melillo, C. García-Vallés, B. Ferrer, M. Álvaro, S. Navalón and H. García, *Org. Biomol. Chem.*, 2021, **19**, 794–800.
383 Y.-B. Huang, J. Liang, X.-S. Wang and R. Cao, *Chem. Soc. Rev.*, 2017, **46**, 126–157.
384 G. Schmid and W. Hofheinz, *J. Am. Chem. Soc.*, 1983, **105**, 624–625.
385 I. Khan, A. Ibrar, W. Ahmed and A. Saeed, *Eur. J. Med. Chem.*, 2015, **90**, 124–169.
386 L. Li and S. B. Herzon, *J. Am. Chem. Soc.*, 2012, **134**, 17376–17379.
387 L. Li, M. Zeng and S. B. Herzon, *Angew. Chem., Int. Ed.*, 2014, **53**, 7892–7895.
388 F. Costantino and P. V. Kamat, *ACS Energy Lett.*, 2022, **7**, 242–246.
389 S. Kampouri and K. C. Stylianou, *ACS Catal.*, 2019, **9**, 4247–4270.
390 M.-Y. Qi, M. Conte, M. Anpo, Z.-R. Tang and Y.-J. Xu, *Chem. Rev.*, 2021, **121**, 13051–13085.
391 W. Shang, Y. Li, H. Huang, F. Lai, M. B. J. Roeffaers and B. Weng, *ACS Catal.*, 2021, **11**, 4613–4632.
392 L. Yuan, M.-Y. Qi, Z.-R. Tang and Y.-J. Xu, *Angew. Chem., Int. Ed.*, 2021, **60**, 21150–21172.
393 Z. Wang, J. Wang, J. Zhang and K. Dai, *Acta Phys.-Chim. Sin.*, 2023, **39**, 2209037.
394 X. Wang, L. Zhu, Z. Lv, Z. Qi, Y. Xu, T. Miao, X. Fu and L. Li, *Chem. Eng. J.*, 2022, **442**, 136186.
395 C. Y. Toe, C. Tsounis, J. Zhang, H. Masood, D. Gunawan, J. Scott and R. Amal, *Energy Environ. Sci.*, 2021, **14**, 1140–1175.
396 K. P. McClelland and E. A. Weiss, *ACS Appl. Energy Mater.*, 2019, **2**, 92–96.
397 W. Sung, B. An, B. Qi, T. Liu, M. Jin and C. Duan, *ACS Appl. Mater. Interfaces*, 2018, **10**, 13462–13469.
398 X.-Y. Lin, M.-Y. Qi, Z.-R. Tang and Y.-J. Xu, *Appl. Catal., B*, 2022, **317**, 121708.
399 K.-Q. Hu, Z.-W. Huang, Z.-H. Zhang, L. Mei, B.-B. Qian, J.-P. Yu, Z.-F. Chai and W.-Q. Shi, *Chem. – Eur. J.*, 2018, **24**, 16766–16769.
400 Q.-Q. Kang, W. Wu, Q. Li and W.-T. Wei, *Green Chem.*, 2020, **22**, 3060–3068.
401 D. Ma, S. Zhai, Y. Wang, A. Liu and C. Chen, *Front. Chem.*, 2019, **7**, 635.
402 S. Singh, V. J. Roy, N. Dagar, P. P. Sen and S. R. Roy, *Adv. Synth. Catal.*, 2021, **363**, 937–979.
403 A. Torregrosa-Chinillach and R. Chinchilla, *Molecules*, 2022, **27**, 497.

404 Y. Wang, X. Zhang, K. Chang, Z. Zhao, J. Huang and Q. Kuang, *Chem. – Eur. J.*, 2022, **28**, e202104514.
405 H. Liu, L. Shi, Q. Zhang, P. Qi, Y. Zhao, Q. Meng, X. Feng, H. Wang and J. Ye, *Chem. Commun.*, 2021, **57**, 1279–1294.
406 Y.-Z. Chen, Z. U. Wang, H. Wang, J. Lu, S.-H. Yu and H.-L. Jiang, *J. Am. Chem. Soc.*, 2017, **139**, 2035–2044.
407 L. Li, W. Yang, Q. Yang, Q. Guan, J. Lu, S.-H. Yu and H.-L. Jiang, *ACS Catal.*, 2020, **10**, 7753–7762.
408 L. Li, Y. Li, L. Jiao, X. Liu, Z. Ma, Y.-J. Zeng, X. Zheng and H.-L. Jiang, *J. Am. Chem. Soc.*, 2022, **144**, 17075–17085.
409 H. Chen, L. Shao, C. Wang and Y. Fu, *J. Mater. Chem. A*, 2022, **10**, 17434–17439.
410 P. Jing, B. Wu, Z. Han, W. Shi and P. Cheng, *Chin. Chem. Lett.*, 2021, **32**, 3505–3508.
411 Y. Shang, X. Xu, B. Gao, S. Wang and X. Duan, *Chem. Soc. Rev.*, 2021, **50**, 5281–5322.
412 X. Wu, W. Zhao, Y. Huang and G. Zhang, *Chem. Eng. J.*, 2020, **381**, 122768.
413 H. Bai, P. He, L. Hao, Z. Fan, R. Niu, T. Tang and J. Gong, *Chem. Eng. J.*, 2023, **456**, 140994.
414 Q. Yang, Y.-Z. Chen, Z. U. Wang, Q. Xu and H.-L. Jiang, *Chem. Commun.*, 2015, **51**, 10419–10422.
415 E. Peiris, S. Hanauer, T. Le, J. Wang, T. Salavati-fard, P. Brasseur, E. V. V. Formo, B. Wang and P. H. C. Camargo, *Angew. Chem., Int. Ed.*, 2023, **62**, e202216398.
416 B. J. Gregori, M.-O. W. S. Schmotz and A. J. von Wangelin, *ChemCatChem*, 2022, **14**, e202200886.
417 X. Chen, K. Shen, D. Ding, J. Chen, T. Fan, R. Wu and Y. Li, *ACS Catal.*, 2018, **8**, 10641–10648.
418 J. Zhang, L. Wang, Y. Shao, Y. Wang, B. C. Gates and F.-S. Xiao, *Angew. Chem., Int. Ed.*, 2017, **56**, 9747–9751.
419 P. Verma, D. J. Stewart and R. Raja, *Catalysts*, 2020, **10**, 1176.
420 N. Zhang, X. Zhang, L. Tao, P. Jiang, C. Ye, R. Lin, Z. Huang, A. Li, D. Pang, H. Yan, Y. Wang, P. Xu, S. An, Q. Zhang, L. Liu, S. Du, X. Han, D. Wang and Y. Li, *Angew. Chem., Int. Ed.*, 2021, **60**, 6170–6176.
421 G. Li, S. Dong, P. Fu, Q. Yue, Y. Zhou and J. Wang, *Green Chem.*, 2022, **24**, 3433–3460.
422 Q.-J. Wu, J. Liang, Y.-B. Huang and R. Cao, *Acc. Chem. Res.*, 2022, **55**, 2978–2997.
423 J. Li, L. He, Q. Liu, Y. Ren and H. Jiang, *Nat. Commun.*, 2022, **13**, 928.
424 R. Ramakrishnan, M. A. Niyas, M. P. Lijina and M. Hariharan, *Acc. Chem. Res.*, 2019, **52**, 3075–3086.
425 H.-H. He, J.-P. Yuan, P.-Y. Cai, K.-Y. Wang, L. Feng, A. Kirchon, J. Li, L.-L. Zhang, H.-C. Zhou and Y. Fang, *J. Am. Chem. Soc.*, 2023, **145**, 17164–17175.
426 J. Liu, J. Xue, G.-P. Yang, L.-L. Dang, L.-F. Ma, D.-S. Li and Y.-Y. Wang, *Coord. Chem. Rev.*, 2022, **463**, 214521.
427 R. E. Sikma, K. S. Butler, D. J. Vogel, J. A. Harvey and D. F. S. Gallis, *J. Am. Chem. Soc.*, 2024, **146**, 5715–5734.
428 M. Y. Masoomi, A. Morsali, A. Dhakshinamoorthy and H. Garcia, *Angew. Chem., Int. Ed.*, 2019, **58**, 15188–15205.
429 S. Abednatanzi, P. Gohari Derakhshandeh, H. Depauw, F.-X. Coudert, H. Vrielinck, P. Van Der Voort and K. Leus, *Chem. Soc. Rev.*, 2019, **48**, 2535–2565.
430 W. Gong, Z. Chen, J. Dong, Y. Liu and Y. Cui, *Chem. Rev.*, 2022, **122**, 9078–9144.
431 Z. Sharifzadeh, K. Berijani and A. Morsali, *Coord. Chem. Rev.*, 2021, **445**, 214083.
432 G. Cai, P. Yan, L. Zhang, H.-C. Zhou and H.-L. Jiang, *Chem. Rev.*, 2021, **121**, 12278–12326.
433 Y. Yao, X. Zhao, G. Chang, X. Yang and B. Chen, *Small Struct.*, 2023, **4**, 2200187.
434 Y. Fan, J. Zhang, Y. Shen, B. Zheng, W. Zhang and F. Huo, *Nano Res.*, 2021, **14**, 1–28.
435 G. Chakraborty, I.-H. Park, R. Medishetty and J. J. Vittal, *Chem. Rev.*, 2021, **121**, 3751–3891.
436 X. Xiao, L. Zou, H. Pang and Q. Xu, *Chem. Soc. Rev.*, 2020, **49**, 301–331.
437 H. Lin, Y. Yang, K. W. Festus, Y.-C. Hsu, R.-R. Liang, I. Afolabi and H.-C. Zhou, *Acc. Mater. Res.*, 2024, **5**, 236–248.
438 S. Ma, W. Han, W. Han, F. Dong and Z. Tang, *J. Mater. Chem. A*, 2023, **11**, 3315–3363.
439 S. Dai, F. Nouar, S. Zhang, A. Tissot and C. Serre, *Angew. Chem., Int. Ed.*, 2021, **60**, 4282–4288.
440 S. Dai, E. Montero-Lanzuela, A. Tissot, H. G. Baldoví, H. García, S. Navalón and C. Serre, *Chem. Sci.*, 2023, **14**, 3451–3461.
441 V. Mansi, V. Shrivastav, P. Dubey, S. Sundriyal, U. K. Tiwari and A. Deep, *Coord. Chem. Rev.*, 2024, **499**, 215497.
442 W. Ma, J. Sun, S. Yao, Y. Wang, G. Chen, G. Fan and Y. Li, *Angew. Chem., Int. Ed.*, 2024, **62**, e202313784.
443 B. Xiang, J. Gong, Y. Sun and J. Li, *J. Hazard. Mater.*, 2023, **462**, 132803.
444 L. Su, X. Liu, W. Xia, B. Wu, C. Li, B. Xu, B. Yang, R. Xia, J. Zhou, J. Qian and L. Miao, *J. Colloids Interface Sci.*, 2023, **650**, 613–621.
445 J. Ouyang and Y. Quan, *ChemCatChem*, 2024, **16**, e202400112.
446 M. Z. Hussain, Z. Yang, Z. Huang, Q. Jia, Y. Zhu and Y. Xia, *Adv. Sci.*, 2021, **8**, 2100625.
447 P. Behera, S. Subudhi, S. P. Tripathy and K. Parida, *Coord. Chem. Rev.*, 2022, **456**, 214392.

